Detection of Coccolithophore Bloom Development in the Salish Sea, Canada: Leveraging Reflectance Data from Autonomous Shipborne *In Situ* Radiometers and Sentinel-3A with a Random Forest Classifier

by

Ziwei Wang

B.Sc., China University of Geoscience, 2012

M.Sc., China University of Geoscience, 2015

A Dissertation Submitted in Partial Fulfilment of the

Requirements for the Degree of

DOCTOR OF PHILOSOPHY

in the Department of Geography

University of Victoria

We acknowledge and respect the Lək̓ʷəŋən (Songhees and X̣ʷsepsəm/Esquimalt) Peoples on whose territory the university stands, and the Lək̓ʷəŋən and W̱SÁNEĆ Peoples whose historical relationships with the land continue to this day.

Detection of Coccolithophore Bloom Development in the Salish Sea, Canada: Leveraging Reflectance Data from Autonomous Shipborne *In Situ* Radiometers and Sentinel-3A with a Random Forest Classifier

by

Ziwei Wang

B.Sc., China University of Geoscience, 2012

M.Sc., China University of Geoscience, 2015

Supervisory Committee:

Dr. Maycira Costa, Supervisor (Department of Geography)

Dr. David Atkinson, Committee Member (Department of Geography)

Dr. Laura Cowen, Committee Member (Department of Mathematics and Statistics)

Abstract

Phytoplankton are the primary producers in the ocean, forming the base of the marine food web. Among them, coccolithophores hold particular significance due to their ability to form extensive blooms and their unique role in oceanic calcium and carbonate cycling, as well as related biogeochemical processes. Current limitations in using satellite imagery to derive accurate phytoplankton data, such as chlorophyll concentrations and phytoplankton functional types stem from insufficient *in situ* reflectance measurements to develop models and validate satellite reflectance. To address this, we deployed a suite of hyperspectral radiometers equipped with autonomous solar tracking capability, collectively known as SAS Solar Tracker (Satlantic Inc./Sea-Bird, denoted as SAS-ST hereafter), atop a commercial ferry traversing the Salish Sea, Canada. We specified the optimal geometry for SAS-ST installation, as well as the identification and flagging of unfavourable meteorological conditions, correction for sun glint and skylight contributions, mitigation of structural interferences, and subsequent application of bidirectional reflectance distribution function (BRDF) corrections to ensure optimal data quality. Assessment of the final data quality was conducted using a quality assurance method that considers spectral shape similarity, revealing that approximately 92% of the acquired reflectance data aligned well with the global database, indicating high quality. During the data collection period of this research in the summer of 2016, an unprecedented coccolithophore bloom occurred in the Salish Sea area. Coccolithophores, a distinctive phytoplankton species, are encased in calcium carbonate plates called coccoliths, which can be shed into the water during later stages of the blooms, significantly augmenting water reflectance. Based on its unique spectral features, our research successfully identified the presence of the coccolithophore bloom and further categorized the bloom spectra into growing and decaying stages. The hyperspectral reflectance

SAS-ST data were initially convolved to the Sentinel-3A OLCI 10 spectral bands spanning 400 to 709 nm. Comparison of Sentinel-3A OLCI satellite spectra with SAS-ST *in situ* data revealed that reflectance acquired by the OLCI satellite was underestimated, particularly in the 400-443 nm range and the decaying bloom category. Consequently, we developed an adapted machine learning algorithm based on wavelengths ranging from 490 nm to 709 nm, which increased the overall prediction accuracy for OLCI-measured coccolithophore spectra from 0.794 to 0.891, and enhanced the Kappa coefficient from 0.14 to 0.60. By leveraging data from autonomous shipborne *In situ* SAS-ST and Sentinel-3A OLCI, my research overcomes current limitations of coccolithophore detection algorithms in coastal waters impacted by river plumes, while also providing new insights into coccolithophore dynamics and potentially enhancing their remote sensing.

Table of Contents

List of Figures

List of Tables

Table 1| Symbols used in this thesis.

E_s	upper hemisphere downwelling irradiance
L_i	sky radiance
L_t	total upwelling radiance received by the sensor pointed at the water surface
L_w	water-leaving radiance
θ_v	sensor viewing zenith angle
θ_s	solar zenith angle
φ_v	sensor-sun azimuth angle
α	SAS-ST rotator angle with reference to the home position
γ	the Sun azimuth angle relative to the ferry heading
ρ_s	sea surface reflectance factor
R_{rs}^{0+}	above-water reflectance
R_{rs}^{M99}	sky glint corrected R_{rs}^{0+} following Mobley (1999)
$R_{rs}^{M99+ship}$	sky glint and ship superstructure perturbation corrected R_{rs}^{0+}
R_{rs}	sky glint, ship superstructure perturbation and BRDF corrected R_{rs}^{0+}
R_{rs}^{ship}	ship superstructure perturbation introduced reflectance
ε	percentage difference for IOPs-based BRDF correction
r	a precipitation flag based on the ratio between $E_s(\lambda = 720$ nm) and $E_s(\lambda = 370$ nm) adapted from Wernand (2002)
u^*	threshold value between two neighbouring classes of weather conditions

$\alpha(\lambda)$	total absorption
$b_{bp}(\lambda)$	particle backscattering
$b_{bw}(\lambda)$	water backscattering
k	sum of $\alpha(\lambda)$, $b_{bp}(\lambda)$ and $b_{bw}(\lambda)$
$G_0^w, G_1^w, G_0^p, G_1^p$	model coefficients $G_0^w, G_1^w, G_0^p, G_1^p$ for water and particles in Lee et al. (2011).
nR_{rs}	reflectance normalized by the respective root-sum-squares at all wavelength
$nR_{rs}{}^*$	normalized reflectance for each water type from Wei et al. (2016)
$\cos\beta$	angle defined between the predefined reference normalized spectrum, $nR_{rs}{}^*$, and the normalized spectrum, nR_{rs}
RFC10	random forest model using 10 bands of OLCI (400-709 nm)
RFC7	random forest model using 10 bands of OLCI (490-709 nm)
Rrs^{SST}	Reflectance retrieved from SAS-ST
Rrs^{OLCI}	Reflectance retrieved from OLCI
L_{wn}	normalized water-leaving radiance
PFTs	phytoplankton functional types

Acknowledgements

Special thanks to my supervisor, Maycira Costa, whose invaluable time and brainstorming sessions greatly contributed to the completion of this work. I extend my gratitude to David Atkinson for his hands-on Python programming course, which significantly enhanced my coding abilities and facilitated the extensive data analysis required for this research. I am also grateful to my family, doctors, and friends for their unwavering support and companionship throughout this journey.

Chapter 1: Introduction

1.1 Overview

Ocean colour satellite sensors, characterized by their ability to monitor spectral variations in water leaving radiance or reflectance across the visible bands of the electromagnetic spectrum, serve as a practical tool for large-scale, synoptic monitoring of aquatic environments, thus providing a comprehensive assessment of the environment's bio-optical variables (Werdell et al., 2018; Groom et al., 2019; Sathyendranath et al., 2017, 2023). Utilizing satellite sensors for ocean colour analysis enables extensive monitoring of key bio-optical variables, including phytoplankton through the retrieval of chlorophyll-a (the primary phytoplankton pigment; Mélin et al., 2011) and phytoplankton functional types (PFTs; IOCCG, 2014), as well as other optically active constituents such as coloured dissolved organic matter (CDOM; Mannino et al., 2014) and non-algal particles (Dogliotti et al., 2015). Ocean colour data provide important information for addressing ecosystem-based fisheries management, analysis of ocean biogeochemical cycles, assessment of ecosystem health, and examination of climate change impacts (Sathyendranath et al., 2023; Brewin et al., 2024). Ocean colour satellites can monitor distinctive PFTs like coccolithophores, whose unique optical properties make them particularly visible in satellite observations. This highlights their significance as an important phytoplankton group to track, with satellite sensors offering a valuable tool for studying their presence and bloom dynamics on a global scale.

Coccolithophores, a distinctive group within the phytoplankton community, are characterized by their unique exoskeleton comprised of an assemblage of individual calcium carbonate plates called coccoliths (Young et al., 2003). This characteristic feature highlights their unique role in marine ecosystems and biogeochemical cycles, particularly in oceanic calcium and carbonate cycling and associated biogeochemical processes through the formation of these calcareous structures (Balch et al., 2011; Balch and Mitchell, 2023). Among the various species of coccolithophores, *Emiliania huxleyi* is notably predominant, exhibiting a wide latitudinal distribution that extends from tropical to subpolar oceans (Holligan and Balch, 1991; Tyrrell and Merico, 2004). These organisms exert a strong influence on the optical properties of the water, increasing water reflectance due to the backscattering properties of their coccospheres. In the later stages of their bloom cycle, when *E. huxleyi* overproduces and sheds coccoliths, the detached coccoliths further enhance backscattering, significantly contributing to the observed increase in water reflectance (Groom and Holligan, 1987; Holligan et al., 1993; Brown and Yoder, 1994). This interaction with light imparts a distinctive milky-turquoise hue to the ocean, a phenomenon that renders these unique blooms particularly conspicuous using ocean colour satellites, thus facilitating their detection and monitoring from space (Gordon et al., 2001; Balch et al., 2005).

The successful use of satellite ocean colour remote sensing to retrieve ocean variables, including PFTs such as coccolithophores, relies on the vicarious calibrations and validation of the satellite data through *in situ* measurements acquired at the ocean surface (Mélin, 2022; Valente et al., 2022). Specifically, this involves the system vicarious calibration of the satellite sensor and rigorous atmospheric correction of top-of-atmosphere measured radiance (L^{TOA}) to align with *in situ* measurements, thereby enabling the accurate derivation of above-water remote sensing reflectance (Rrs^{0+}) and biogeochemical products (Zibordi et al., 2015a, 2015b; Mélin, 2022; Valente et al., 2022). The scientific community has undertaken significant efforts to collect and systematically archive ocean colour *in situ* measurements (Valente et al., 2022), including contributions from several long-term international programs that provide Fiducial Reference Measurements (FRMs). For instance, the Marine Optical BuoY (MOBY), a fixed mooring *in situ* radiometric system deployed off the coast of Lanai, measures incident sunlight and water-leaving radiance at various depths (Clark et al., 2003). Another example is the Ocean Colour component of the Aerosol Robotic Network (AERONET-OC), which provides fully normalized water-leaving radiance through standardized measurements conducted at different sites using identical systems and protocols, calibrated with a single reference source and method, and processed with the same codes (Zibordi et al., 2006, 2009).

Effectively separating the atmospheric signal from L^{TOA} necessitates high-quality *in situ* matchup radiometric data. This data is required for both the development and validation of atmospheric correction models, thereby enhancing the accuracy of derived products such as water-leaving radiance (L_w) and remote sensing reflectance (Rrs^{0+}) (Ruddick et al., 2006; Ahmad et al., 2010). The validation of atmospherically-corrected L_w and Rrs^{0+} typically involves comparative analyses with *in situ* measurements acquired from a variety of platforms, including moored buoys (Antoine et al., 2008), stationary platforms (Zibordi et al., 2006, 2009; Vansteenwegen et al., 2019; Tilstone et al., 2020; Vanhellemont and Ruddick, 2021), and mobile platforms such as research vessels and ships of opportunity (Simis and Olsson, 2013; Brando et al., 2016; Carswell et al., 2017; Tilstone et al., 2020; Giannini et al., 2021; Brewin et al., 2024).

The above methodologies serve as solutions to mitigate the lack of *in situ* measurements, thereby optimizing the utility of ocean colour satellite data and atmospheric correction models.

However, off the western coast of Canada, the availability of *in situ* matchups for satellite optical sensors, including those for multispectral Sentinel-3 series, is constrained due to the high expenses associated with ocean-based fieldwork, the labour-intensive nature of manually adjusting the radiometer's geometry on ships-of-opportunity, and the frequent cloud cover, which diminishes the quality of costly field-collected data. To address these problems, this research utilizes the SAS Solar Tracker (denoted as SAS-ST), a suite of autonomous hyperspectral radiometers installed on a commercial ferry that crosses the Salish Sea multiple times daily. Its effective deployment and successful operation greatly enhanced the understanding of the Salish Sea area, especially given the limited number of available matchups before its implementation (Carswell et al., 2017). In addition to increased spectral resolution, SAS-ST also enables spatially continuous measurement of the water body when deployed on mobile platforms, different from stationary above-water sensors such as AERONET-OC (Zibordi et al., 2006, 2009) and WATERHYPERNET (Vanhellemont and Ruddick, 2021). This advancement not only enhances the ability to supplement the network of fixed platforms, but also expands the capacity for research and observation in various marine environments, including coastal waters, as in this research (Brewin et al., 2024). This move from multispectral to hyperspectral, from fixed platform and occasionally cruise to consistent mobile platform, has resulted in the availability of a large *in situ* ocean colour dataset for this research. Moreover, the methodology outlined in this work is adaptable to other regions worldwide that lack *in situ* reflectance data, utilizing ships-of-opportunity platforms.

Coinciding with the SAS-ST acquisition period, an unprecedented coccolithophore bloom, one order of magnitude more intense than typical blooms (Balch and Mitchell, 2023), occurred in the Salish Sea area (NASA, 2016; Chandler et al., 2017; Simpson et al., 2022; Nemceka et al., 2023). The SAS-ST acquired above water radiometric data throughout the entire life cycle of this coccolithophore bloom. The current approach for identifying and monitoring coccolithophore bloom dynamics and distribution patterns across global oceans mainly relies on satellite technology and associated algorithms (Balch and Mitchell, 2023). Additionally, the widely accepted coccolithophore flagging algorithms were developed primarily for Case 1 open ocean waters (Moore et al., 2012), rendering them unsuitable for application to coccolithophore blooms occurring in Case 2 coastal waters, as in our case. Therefore, the *in situ* hyperspectral measurements provided by SAS-ST in the Salish Sea was crucial to enable a more detailed analysis of the reflectance characteristics of coccolithophores bloom development, supporting the development of a more refined detection algorithm for coccolithophore monitoring in the coastal region.

A variety of methodologies have been developed and implemented for detecting and characterizing coccolithophore bloom events using satellite observations, effectively identifying and monitoring bloom dynamics and distribution patterns across global oceans, thereby enhancing our understanding of their potential impacts on marine ecosystems and biogeochemical cycles (Balch and Mitchell, 2023). These approaches utilize the distinctive reflectance patterns of coccolithophore blooms, including the coccolith flag algorithm proposed by Brown and Yoder (1994) and later modified by Iglesias-Rodríguez et al. (2002), as well as an optical water type classifier proposed by Moore et al. (2012). Other approaches for coccolithophore detection are the estimation of particulate inorganic carbon (PIC) concentrations from ocean colour imagery, given that coccolithophores are the major producer of PIC among the many calcifying marine organisms (Tyrrell et al., 1999; Smyth et al., 2002; Balch et al., 2011). PIC primarily comprises calcium carbonate produced by various planktonic organisms, such as coccolithophores, foraminifera, and pteropods, with coccolithophores responsible for the majority of optical PIC backscattering, while larger PIC particles associated with foraminifera and pteropods have minimal optical impact (Balch et al., 1996; Balch and Mitchell, 2023). Two widely used PIC algorithms are the two bands or three bands (2B/3B) method proposed by Balch et al. (2005) and Gordon et al. (2001), which have been accepted as NASA's standard PIC algorithms, along with the two-band colour index algorithm introduced by Mitchell et al. (2017).

1.2 Research Objectives

The main goal of my research is to develop a machine learning model to characterize coccolithophore bloom development based on *in situ* autonomous radiometry and Sentinel-3A data. This was accomplished by analyzing a unique time series of above water reflectance data acquired with an autonomous set of radiometers deployed in the Queen of Oak Bay Ferry, crossing the Salish Sea, Canada, during the development of an intense coccolithophore bloom. Prior to the model development, the installation, deployment settings, flags and corrections and quality control of the *in situ* radiometric data were performed. The following specific objectives were addressed:

(1) Develop a methodological framework to facilitate the acquisition, processing, and quality control of above water remote sensing reflectance obtained with the SAS Solar Tracker system, focusing on robust procedures to ensure high quality measurements under ideal environmental conditions. To accomplish this, a set of autonomous radiometers were installed aboard the ferry, ensuring optimal geometry for data acquisition. Flags were developed to filter out measurements under adverse meteorological conditions, and corrections were applied for sky glint, ship superstructure perturbation and BRDF effects, followed by a quality control procedure to ensure data reliability. This high quality *in situ* dataset was then used to train a machine learning model for the coccolithophore bloom development stages classification in Objective 2.

(2) Utilize *in situ* measurements collected with SAS-ST as validation matchups for satellite-derived (OLCI from Sentinel-3A) atmospherically corrected Rrs^{0+}, and leverage both datasets to develop regional machine learning models aimed at monitoring both the occurrence and temporal evolution of coccolithophore blooms in the Salish Sea. To accomplish this, the *in situ* dataset from Objective 1, which involved a detailed processing of *in situ* SAS Solar Tracker measurements, was used to develop a machine learning model for characterizing coccolithophore bloom development stages. This model was then applied to Sentinel-3A imagery to enable large scale monitoring of bloom dynamics in the Salish Sea.

Overall, this research advances our knowledge to use remote sensing data, both *in situ* and satellite, to track coccolithophore bloom dynamics by analyzing a robust and comprehensive dataset that integrates autonomous shipborne *in situ* reflectance measurements with satellite-derived reflectance data. The outcome of this thesis enhances the availability of *in situ* matchups that support the validation of satellite ocean colour sensors in the Salish Sea through the successful operation of the autonomous SAS-ST system aboard a commercial ferry, thus contributing to the global effort to define operational methods for increasing *in situ* data to validate present and future satellite platforms. Furthermore, by combining satellite data with the large *in situ* reflectance dataset, I developed a regional machine learning model aimed at satellite-based monitoring of coccolithophore blooms in the Salish Sea with high detection accuracy. Beyond regional applications, the methodological framework established in this study can be adapted to other oceanic regions, contributing to improved measurements of coccolithophore distributions in the global ocean. This is essential for refining estimates of oceanic carbon fluxes, understanding associated biogeochemical cycling, and assessing potential impacts on fisheries and marine ecosystem health.

1.3 Thesis Structure

This thesis is separated into two main papers to address the research objectives. Chapter 2 (Objective 1) provides a methodological framework for the acquisition, processing, and quality control of above-water remote sensing reflectance acquired with the autonomous ship-borne *in situ* radiometers-SAS-ST. It should be noted that Chapter 2 is the published paper Wang and Costa (2022); however, we acknowledge that Wang is the principal author (defined as the co-author who is responsible for 90% or more of a paper’s contents). Chapter 3 (objective 2) uses the *in situ* measured Rrs^{0+} collected with SAS-ST obtained as part of objective1, in conjunction with Sentinel-3A atmospherically corrected Rrs^{0+} to develop regional machine learning models for coccolithophore bloom monitoring. Lastly, the conclusion (Chapter 4) unites these two objectives and summarizes the broad implications of my work.

Chapter 2: **Autonomous shipborne *in situ* reflectance data in optically complex coastal waters: a case study of the Salish Sea, Canada**

Frontiers in Remote Sensing, 2022

https://doi.org/10.3389/frsen.2022.867570

Ziwei Wang, Maycira Costa

Department of Geography, University of Victoria, Victoria, BC, Canada

Abstract

Present limitations on using satellite imagery to derive accurate chlorophyll concentrations and phytoplankton functional types arise from insufficient *in situ* measurements to validate the satellite reflectance, R_{rs}^{0+}. We installed a set of hyperspectral radiometers with autonomous solar tracking capability, collectively named SAS Solar Tracker (Satlantic Inc./Sea-Bird), on top of a commercial ferry, to measure the *in situ* reflectance as the ferry crosses the Salish Sea, Canada. We describe the SAS Solar Tracker installation procedure, which enables a clear view of the sea surface and minimizes the interference caused by the ship superstructure. Corrections for residual ship superstructure perturbations and non-nadir-viewing geometry are applied during data processing to ensure optimal data quality. It is found that the ship superstructure perturbation correction decreased the overall R_{rs}^{0+} by 0.00055 sr^{-1}, based on a black-pixel assumption for the infrared band of the lowest-acquired turbid water. The BRDF correction using the inherent optical properties approach lowered the spectral signal by ~5-10%, depending on the wavelength. Data quality was evaluated according to a quality assurance method considering spectral shape similarity, and ~92% of the acquired reflectance data matched well against the global database, indicating high quality.

2.1 Introduction

Ocean colour satellite sensors are a practical approach for large-scale synoptic monitoring of aquatic environments by providing bio-optical variables such as chlorophyll concentration (a direct proxy for phytoplankton biomass) and inherent optical properties (Sathyendranath et al., 2017; Werdell et al., 2018; Groom et al., 2019). However, proper vicarious calibration (space sensor calibration) and atmospheric correction of top of atmosphere measured radiance (L^{TOA}) are required to retrieve accurate water-leaving radiance (L_w) and, consequently, remote sensing reflectance ($R_{rs}{}^{0+}$) and biogeochemical products (Zibordi et al., 2015a, 2015b). For space sensor calibration, Fiducial Reference Measurements (FRMs), which come with uncertainty budgets including those for sensors calibration and high-quality protocols for data acquisition, are ultimately required (Ruddick et al., 2019). Long-term international programs providing FRMs are, for example, the Marine Optical Buoy (MOBY), the Buoy for the Acquisition of a Long-Term Optical Time Series (Bouée pour L'acquisition de Séries Optiques à Long Terme, BOUSSOLE), the NASA bio-Optical Algorithm Data set (NOMAD), the Ocean Reflectance Models (ORM) and the Ocean Colour component of the Aerosol Robotic Network (AERONET-OC). Generally, these programs have provided a range of 46 to 241 high-quality matchups over 3 to 7 years for vicarious calibration of various ocean colour satellites (Zibordi et al., 2015b). For addressing the atmospheric signal from L^{TOA}, high quality in-situ radiometric data is also required for the development and validation of optimal atmospheric correction models (Ruddick et al., 2006; Ahmad et al., 2010; Müller et al., 2015; Carswell et al., 2017; Zibordi et al., 2018; Giannini et al., 2021). Atmospherically-corrected L_w and $R_{rs}{}^{0+}$ are generally validated in comparison with in-situ matchups acquired with radiometers installed on moored buoys (e.g., Antoine et al., 2008), stationary platforms (e.g., Zibordi et al., 2006, 2009; Vansteenwegen et al., 2019; Tilstone et al., 2020; Vanhellemont and Ruddick 2021), and mobile platforms such as research vessels and ship of opportunities (e.g., Simis and Olsson 2013; Brando et al., 2016; Carswell et al., 2017; Ottaviani et al., 2018; Tilstone et al., 2020; Giannini et al., 2021). Among mobile platforms, deploying sensors aboard research vessels is the most common approach and requires different levels of human interaction to provide optimal geometry for data acquisition. For instance, Ruddick et al. (2006), Carswell et al. (2017), Phillips and Costa (2017) and Tilstone et al. (2020) adjusted the geometry as required according to the Sun and vessel position. Hooker et al. (2012), Simis and Olsson (2013), Brando et al. (2016) and Ottaviani et al. (2018) deployed instead radiometers with the autonomous capability of defining optimal geometry based on real-time Sun position and ship orientation.

Within the scope of autonomous measurements from stationary and mobile platforms, predefined optimal geometry of acquisition, flagging of non-optimal environmental conditions, data correction for the effects of Sun glint and skylight contributions, and structure interferences are the most important to obtain high-quality R_{rs}^{0+} measurements (Hooker and Morel 2003; Zibordi et al., 2006, 2009, 2015a; Simis and Olsson 2013; Ottaviani et al., 2018). First, maintaining optimal viewing geometry is a considerable challenge in shipborne reflectance measurement as the ship and the Sun are constantly moving. The general ideal geometry of acquisition, as recommended in the literature, is as follows: a viewing zenith angle (θ_v) of the upwelling radiance sensor (L_t) of 40°, and a viewing azimuth angle (φ_v) between the sensors and the Sun of $90^{\circ} < \varphi_v < 135^{\circ}$ (ideally 135°) to minimize Sun glint (Mobley 1999; Simis and Olsson 2013). At the same time, the sensors should be deployed to avoid the effect of ship shadow, sea spray, and minimize ship superstructure perturbation (Mobley 1999; Hooker and Morel 2003; Ottaviani et al., 2018). Second, the instantaneous cloud cover conditions affect the spectral (ir)radiance distributions from the Sun and sky, thus resulting in variation in measurements of sky radiance and in the sky glint contribution to the upwelling radiance (Mobley 1999; Ruddick et al., 2006). Therefore, clear sky conditions are ideal for high-quality measurements. As such, meteorological flags need to be applied. Finally, the presence of a fixed platform or the research vessel itself modifies the radiance field, since the platform shadow or multiple reflections between the superstructure and the water can fall into the sensor's field of view (Hooker and Morel 2003).

Here, we provide a framework for the acquisition, processing, and quality control of above-water remote sensing reflectance acquired with the SAS Solar Tracker (Satlantic Inc./Sea-Bird, denoted as SAS-ST). This autonomous sensor is installed aboard a ship of opportunity, the Queen of Oak Bay (QoOB) ferry, which crosses multiple times each day the Salish Sea off the west coast of Canada. The data processing included screening via meteorological flags, reflected sky radiance correction, superstructure signal correction and BRDF corrections, followed by quality control of R_{rs}^{0+} based on method by Wei et al. (2016). The defined framework was based on published protocols (Mobley 1999; Hooker and Morel 2003; Simis and Olsson 2013), and adapted for acquiring high-quality R_{rs}^{0+} measurements according to the local conditions. The purpose of these measurements is to provide matchups for validation of satellite-derived atmospheric corrected R_{rs}^{0+}, and the development of regional hyperspectral-based bio-optical models for deriving biogeochemical products (e.g., phytoplankton functional types). Off the west coast of Canada, the number of available matchups is restricted due to the limited research vessel trips, required labour on the ships of opportunity to manually adjust the radiometer's geometry (Komick et al., 2009; Carswell et al., 2017) and the frequent cloud coverage (Hilborn and Costa 2018). Therefore, the successful operation of the autonomous SAS-ST is very desirable in this area. The methodology presented here is adaptable to other regions of the world lacking in-situ reflectance data, and provides a step forward to complement a network of fixed platforms above-water sensors such as AERONET-OC (Zibordi et al., 2009) and WATERHYPERNET (Vanhellemont and Ruddick 2021).

2.2 Materials and Method

2.2.1 Study Area

The Salish Sea is an estuarine system in the southwest of Canada, extending about 200 km in length by 30 km in width with an average depth of 150 m (Figure 1 A). It is composed of the Strait of Georgia (SoG), the Puget Sound and the Juan de Fuca Strait, and it is connected to the Pacific Ocean via the Juan de Fuca Strait in the South and the Johnstone Strait in the North. Since the northern passage is very constricted, most of the water exchange between the Salish Sea and the Pacific waters flows through the southern passage (Masson, 2002; Pawlowicz et al., 2019). A vital feature of the SoG is the significant freshwater inputs from the Fraser River (Johannessen et al., 2003; Yunker and Macdonald, 2003), which drive southward estuarine circulation, and the corresponding river plume extends into and occasionally entirely across the central and southern SoG(Li et al., 2000; Halverson and Pawlowicz, 2008, 2011; Pawlowicz et al., 2017, 2019).The river plume has a high concentration of total suspended matter (TSM), and coloured dissolved organic matter (CDOM) due to its terrestrial origin, which produces optically complex waters with the highest light attenuation, particularly in the spring and summer times (Loos and Costa, 2010). The discharge of the Fraser River typically peaks with a freshet in mid-June following snowpack melt (Masson, 2002, 2006).

Biologically, the Salish Sea typically has maximum diatom-dominated spring blooms followed by weaker fall bloom events (Allen and Wolfe, 2013). The timing of the spring phytoplankton bloom varies interannually and is mediated by light availability due to cloud cover, wind dynamics, and timing of spring freshwater outflow (Collins et al., 2009; Masson and Peña, 2009; Allen and Wolfe, 2013; Phillips and Costa, 2017; Suchy et al., 2019). The second most abundant phytoplankton group in this region is dinoflagellates, peaking in the summer and early fall (Pospelova et al., 2010). Calcifying phytoplankton, such as coccolithophore (*Emiliania huxleyi*), uncommon within the SoG (Haigh et al., 2015), were observed to flourish in July and August of 2016 when SAS-ST acquired data for the research presented here. With the high particulate discharge from the Fraser River, the Salish Sea is thus an optically dynamic coastal system (Loos and Costa, 2010).

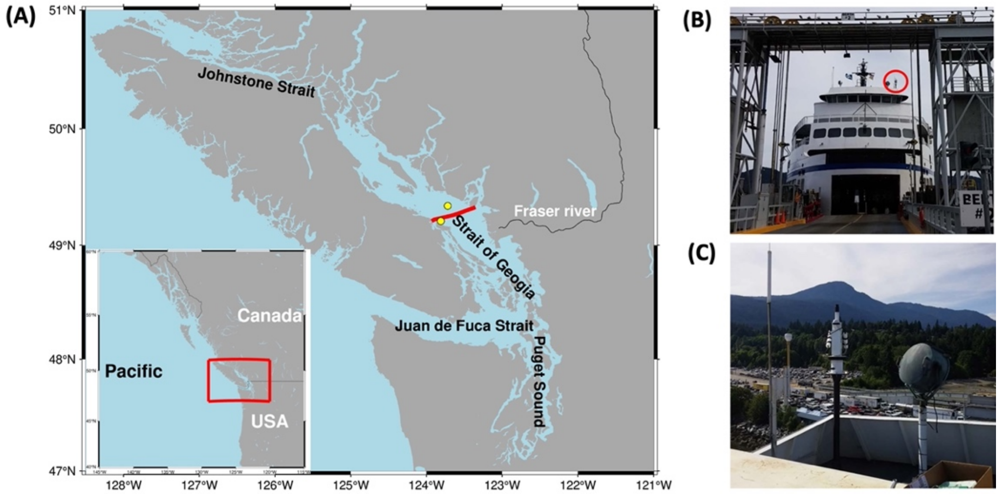

Figure 1| (A) The Salish Sea study area. Red line indicates the track of the Queen of Oak Bay. Two yellow dots are Entrance Island (49.21 N, 123.81 W) and Halibut Bank (49.34N, 123.72W) for local wind measurement; (B) SAS-ST is installed on the deck of the Queen of Oak Bay (red circle) at a total height of 19 m above the water surface; (C) SAS-ST is mounted on top of a custom-fabricated pedestal, and the base of the pedestal is bolted to a welded stand.

2.2.2 Dataset

Here we describe the installation of the SAS-ST on the QoOB and data acquisition and processing. Biogeochemical data from the BC FerryBox, which automatically measures a series of environmental oceanographic parameters, aided in the ferry's perturbation correction approach and the characterization of the water spectral types.

2.2.2.1 SAS Solar Tracker Installation and Acquisition Geometry

The SAS-ST was installed on a commercial ferry, BC Ferries Queen of Oak Bay, about 139 m long and 27 m wide. The ferry sails at approximately 20 knots (10.3 m/s) from Departure Bay, Nanaimo to Horseshoe Bay, West Vancouver, BC, totaling a distance of about 55 km (Figure 1A). The SAS-ST is mounted 19 m above the water surface on top of a custom-fabricated pedestal designed by Ocean Networks Canada (ONC), and the base of the pedestal is bolted to a welded stand (Figure 1B, C). The SAS-ST is equipped with a drive unit as a base and thus has the advantage of solar tracking capability, which permits autonomous operation to maintain optimal viewing geometry (Satlantic, 2016). The SAS-ST consists of two hyperspectral radiometers to measure sea surface total upwelling radiance, $L_t(\lambda)$, and sky radiance, $L_i(\lambda)$, with a 3° half-angle field of view (FOV), and a third sensor to measure the upper hemisphere downwelling irradiance, $E_s(\lambda)$ (Figure 2A). These sensors perform automated measurements up to a frequency of 3Hz, and automatically adjust their integration time to the instantaneously measured light intensity (Satlantic, 2016; Tilstone et al., 2020). In addition to the three radiometers and the drive unit, a GPS receiver and a junction box (including power and communication components) are mounted onto the SAS-ST system. The true ship heading data is acquired by a Hemisphere Vector GPS sensor installed by ONC beside SAS-ST, which processes signals from two GPS antennas to determine the true ship heading. These data are fed into the SAS-ST's acquisition module housed in the junction box. This auxiliary GPS was required because the metal structure of the ferry causes the internal SAS-ST GPS's heading measurement to lack the necessary accuracy. The SAS-ST serial data stream and auxiliary GPS heading measurement are sent to a serial-to-Ethernet converter, served on the ONC local area network (LAN) on a transmission control protocol (TCP) port. Mounted in the ONC telemetry box is a small computer that runs a driver developed on a Linux operating system. It has Ethernet connectivity and collects SAS-ST data from the LAN, stores the data, and sends it to ONC's server onshore. This setup allows for data to be downloaded in near real-time directly from ONC's Oceans 2.0 portal (https://data.oceannetworks.ca/DataSearch).

To avoid the effects of sun glint and reduce ship shadow and ship superstructure influence, the $L_t(\lambda)$ and $L_i(\lambda)$ sensors were positioned at a fixed viewing zenith angle, $\theta_v = 50^o$, and programmed to maintain a sensor-sun azimuth $\varphi_v = 120\pm5°$, following Hooker and Morel (2003) (Figure 2A). The value of θ_v was adapted from the optimal guidelines to keep the FOV of the L_t sensor further away from the ferry and avoid ship shadow, while φ_v was chosen around 120°, roughly the median of 90°-135°, to allow the drive unit to operate within a range of angles. These parameters are programmed as part of the "deployment setup" (see Appendix A, Section 1) before the system starts acquiring data, and can be changed as needed. To attain the optimal geometric conditions, the ferry run from 12:50 to 14:30 local time was designated for data acquisition during the spring and summer.

The preset φ_v is maintained using the autonomous stepper motor platform that triggers the required positioning according to the ship heading and the solar azimuth. The geometric setup was planned for the ferry run that approximately coincides with the time of imagery acquisition by several operational ocean colour satellites. First, for the optimal time of data acquisition (12:50 to 14:30 LT), the solar azimuth angle relative to the ferry heading, indicated as γ in Figure 2B, changed within the 90° to 140° range, with the Sun always at starboard. This is important because the port side, where the SAS-ST was installed, was not directly illuminated by the Sun, so that the ship reflections in the region where the L_t FOV falls (orange area in Figure 2B) are minimized. The defined geometry of acquisition adjusted optimal guidelines (Mobley, 1999) to local conditions, and the data analysis followed the protocol of Hooker and Morel (2003) to minimize the interference of the white wall of the ship (Section 2.2.2.2.4). Moreover, based on the solar geometry at typical times of acquisition ($\theta_s \approx 30°$), a ship's shadow measuring 14 m in extent (grey area in Figure 2B) was predicted to be cast at the port side, a fact which was confirmed during field observations. The ship's shadow was within the FOV of the L_t sensor when the rotator angle (denoted as α, with reference to the home position) was lower than -50°. Therefore, any SAS-ST data acquired at α lower than -50° were filtered out from further analysis.

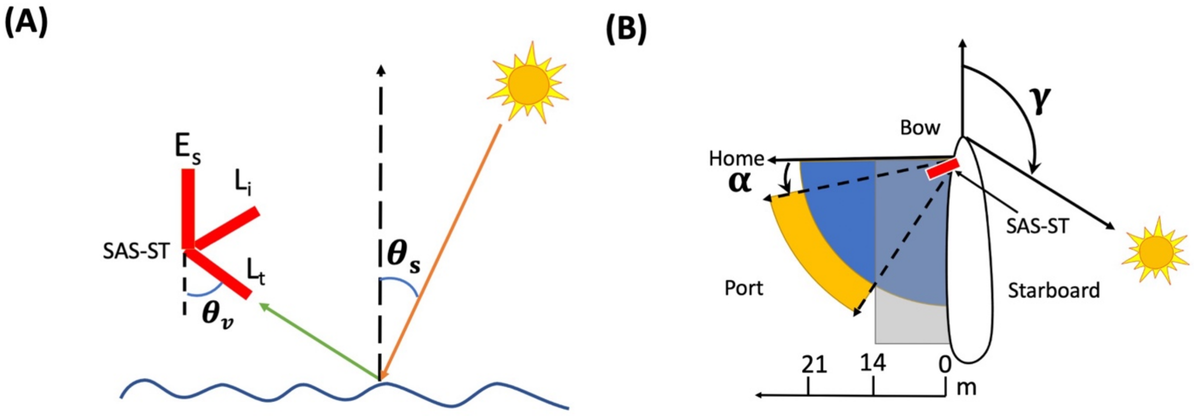

Figure 2| **(A)** SAS-ST geometry of acquisition. Red bars are the three radiometers with $\theta_v = 50°$. The solar zenith angle θ_s is about 30° at the time of data acquisition in spring and summer. **(B)** Position of SAS-ST regarding the ferry and the Sun. The red bar indicates SAS-ST, blue indicates water, the orange stripe indicates the L_t footprint, and the grey area indicates ship shadow as far as 14 m from the ship wall. γ is 90° to 140°, and α is -15° to -50°. Note that the ferry is not drawn to scale.

2.2.2.2 SAS Solar Tracker Data Processing

This section explains the data calibration and the meteorological flags used to preprocess the raw SAS-ST data. After the calibration and the application of the screening flags, data were subjected to sky and sun glint, ship perturbation, and BRDF corrections.

2.2.2.2.1 *Calibration and Flags*

An application with batch-mode capability, PySciDON (Python Scientific Framework for Development of Ocean Network application; Vandenberg et al., 2017), was developed by our research group to apply the calibration files to the raw data stream for each sensor. The software accounts for the rotator angle and Sun azimuth angle flag, time and wavelength interpolation, longitude or time binning, meteorological flags, Mobley's wind-based ρ_s factor correction (Mobley, 1999), and the correction for the ship superstructure perturbation. This application also provides band simulations for Sentinel-3 and MODIS-Aqua (not used in this research) and general statistical tools, including mean, median, and standard deviation for the specified binning mode. Sensors were freshly calibrated before deployment (and optics were cleaned bi-weekly during deployment), and the calibration files from Satlantic Inc. provide descriptions of the format of the raw data files. More details can be found in Vandenberg et al. (2017) and the Satlantic Inc.'s Instrument File Standard document (Satlantic, 2011).

2.2.2.2.2 *Meteorological Flags*

The definition of meteorological flags followed the recommendations of Wernand (2002) to address unfavourable measurement circumstances, such as low light, dusk and dawn, and precipitation. The author defined a precipitation flag based on the ratio (denoted as r) between E_s (λ = 940 nm) and E_s (λ = 370 nm) to infer the influence of Mie scattering by raindrops at 370 nm and absorption by H_2O at 940 nm (Eismann, 2012). This part of the spectra is beyond SAS-ST's spectral range (350-800 nm); therefore, the precipitation flag uses 720 nm, which is also an absorption band of water vapour (Eismann, 2012), as also suggested by Wernand (2002). The low-light and dawn/dusk flags were also adjusted to the wavelength range of the SAS-ST. The meteorological flags were therefore specified as follows:

Flag 1, $E_s(\lambda = 480 \text{ nm}) > 2\, u \text{ W} \cdot \text{cm}^{-2} \cdot \text{nm}^{-1}$: selecting significant E_s (not low light).

Flag 2, $E_s(\lambda\text{=470nm})/E_s(\lambda\text{=680 nm})>1$: masking spectra acquired at dawn/dusk.

Flag 3, $r=E_s(\lambda = 720 \text{ nm}) / E_s(\lambda = 370 \text{ nm})$: value defined according to a predefined threshold masking spectra affected by rainfall and high humidity.

The definition of Flag 3 took into consideration approximately 35000 *in situ* E_s spectra acquired with the SAS-ST system at different meteorological conditions between 13:00 and 14:30 LT from June 18 to July 13, 2016. All the measured in-situ spectra were averaged every 1 minute, resulting in about 1400 averaged spectra. Humidity data at 1-minute intervals were acquired with an RM Young Temperature RH installed on the ferry. Additionally, a camera was installed horizontally on top of the SAS-ST supporting frame, to acquire sky photos with a similar viewing geometry as the E_s sensor. Weather conditions were determined based on the visual evaluation of 1400 sky photos, which were organized into four classes: rainy, overcast, variable clouds (corresponding to 100%, 75%, and 50% cloudy conditions), and clear sky (corresponding to <=25% cloudy and clear sky conditions).

To address Flag 3, E_s and humidity data measured simultaneously were associated with the four weather classes. With this dataset, a discriminant analysis (Gao, 2005) was applied to r (N=1,400) to determine the threshold value between two neighbouring classes of weather conditions (denoted as u^*) according to:

$$\boldsymbol{u}^* = \frac{\boldsymbol{u1 * \sigma 2 + u2 * \sigma 1}}{\boldsymbol{\sigma 1 + \sigma 2}} \qquad (1)$$

where u and σ are the mean and the standard deviation of the two neighbouring weather classes. The spectra were organized according to u^* into the weather condition classes. An accuracy assessment was conducted following a confusion matrix approach, which summarizes agreement and disagreement in the classified and in-situ, with the matrix's diagonal elements representing the counts correctly classified (Rosenfield and Fitzpatrick-Lins, 1984).

2.2.2.2.3 *Deriving R_{rs}^{0+}*

Different approaches are available to derive R_{rs}^{0+}, each with a certain level of complexity. For instance, Ruddick et al. (2006) suggested considering the spectral shape of the R_{rs}^{0+} for moderately- to highly-turbid waters. Simis and Olsson (2013) developed the "fingerprint method" to minimize the atmospheric gas absorption features in the reflectance spectrum by optimizing the sky radiance contribution to the water radiance signal. Gege (2014) and Groetsch et al. (2017) put forward a three-component reflectance model, which considers a spectrally resolved offset to correct for residual Sun and sky glint. This method generally performs best with local IOPs measurements, which can not always be applied to the water conditions of our study area. Here, the remote sensing reflectance (denoted as R_{rs}^{M99}) was calculated following Mobley (1999) considering its good performance, simplicity and the wide use by the community (e.g., Zibordi et al., 2009; Zibordi 2016):

$$\boldsymbol{R_{rs}^{M99}(\lambda)} = \frac{\boldsymbol{L_t(\lambda) - \rho_s L_i(\lambda)}}{\boldsymbol{E_s(\lambda)}} \qquad (2)$$

where the numerator represents the water-leaving radiance, $L_w(\lambda)$, and ρ_s is the fraction of sky radiance (L_i) that is measured by the sea viewing sensor (L_t), (Mobley, 1999). Variable illumination and surface roughness conditions make the determination of ρ_s a challenge (Mobley, 1999). The value of ρ_s is usually less than 5% of the acquired L_i (Morel and Bricaud, 1981). However, the sky glint ($\rho_s L_i(\lambda)$) can have a similar magnitude of L_w, and therefore the choice of ρ_s significantly influences the accuracy of R_{rs}^{M99} calculations (Mobley, 1999). The value of ρ_s was defined considering the local wind speed measured at Entrance Island (49.21 N, 123.81 W) and Halibut Bank (49.34N, 123.72W) (Figure 1A), available on the website of Environment and Climate Change Canada. Data from the ship anemometer were not used, due to challenges in correcting for the movement of the ferry.

2.2.2.2.4 *Ship superstructure perturbation correction*

The ship superstructure influences the above-water radiometry by introducing a signal to the radiance field measured by the sea viewing sensor. Here, we considered that the ship wall was always under non-sunlit conditions, which minimizes any superstructure reflection onto the water. Further, any data acquired at rotator angles lower than -50° (less than 14 m from the ship wall) is removed from further analysis due to possible measurements of shadowed waters. Hooker and Morel (2003) assume that the reflection of a white ship's superstructure onto the water (denoted $L^{ship}(\lambda)$) has the same spectral composition as $E_s(\lambda)$, and that the infrared reflectance (e.g. 780 nm) from clear waters was negligible. Thus, the contribution of $L^{ship}(\lambda)$) to $L_t(\lambda)$, can be written as

$$\boldsymbol{L^{ship}(\lambda) = \frac{[L_t(780) - \rho_s L_i(780)]}{E_s(780)} E_s(\lambda) = R_{rs}^{M99}(\ 780) E_s(\lambda)} \quad (3)$$

At any wavelength, the reflectance corrected for the sky and ship perturbation contributions, denoted $R_{rs}^{M99+ship}(\lambda)$, was calculated as

$$\boldsymbol{R_{rs}^{M99+ship}(\lambda) = \frac{[L_t(\lambda) - \rho_s L_i(\lambda) - L^{ship}(\lambda)]}{E_s(\lambda)}} \quad (4)$$

Substituting for $L^{ship}(\lambda)$ in Eq. 4, we have:

$$\boldsymbol{R_{rs}^{M99+ship}(\lambda) = \frac{[L_t(\lambda) - \rho_s L_i(\lambda)]}{E_s(\lambda)} - R_{rs}^{M99}(\ 780)} \quad (5)$$

where $R_{rs}^{M99}(\ 780)$ is a constant reflectance at 780 nm and corresponds to the ship contributed reflectance, R_{rs}^{ship}. To define this constant, L_t and the corresponding L_i and E_s measurements were chosen from the day with the lowest water reflectance, acquired under the lowest water turbidity conditions (turbidity data from the FerryBox system). For these conditions, we selected approximately 731 R_{rs}^{M99} spectra from July 06, 2016 (Level 3A). The measured $R_{rs}^{M99}(780)$ therefore corresponds to R_{rs}^{ship}, and Eq. 5 can be re-written as:

$$\boldsymbol{R_{rs}^{M99+ship}}(\boldsymbol{\lambda}) = \frac{[\boldsymbol{L_t}(\boldsymbol{\lambda})-\boldsymbol{\rho_s L_i}(\boldsymbol{\lambda})]}{\boldsymbol{E_s}(\boldsymbol{\lambda})} - \boldsymbol{R_{rs}^{ship}} \qquad (6)$$

2.2.2.2.5 *BRDF correction*

To minimize the non-isotropic distribution of the water-leaving radiances in optically complex waters, a BRDF correction was applied following the inherent optical properties approach proposed by Lee et al. (2011). We developed a Python version of the code, adapted from the IDL version developed by Talone et al. (2018). The approach considers a two-step process: first, the quasi-analytical algorithm (QAA) method (Lee et al., 2002, 2011) is applied to $R_{rs}^{M99+ship}(\theta,\varphi)$ to retrieve the IOPs. Second, the derived IOPs and accompanying G coefficients at nadir view are used to calculate the $R_{rs}^{M99+ship}(0,0)$. More specifically, with the input of seawater absorption, seawater backscattering (Lee et al., 2011), and $R_{rs}^{M99+ship}(\theta,\varphi)$, total absorption at a reference wavelength (λ_0 = 555 or 670 nm in QAA_V6) $\alpha(\lambda_0)$ and particle scattering $b_{bp}(\lambda_0)$ are calculated first. Particle scattering, $b_{bp}(\lambda)$, is then calculated by applying the power-law model on $b_{bp}(\lambda_0)$ (λ_0 = 555 or 670 nm). Total absorption at all wavelengths, $\alpha(\lambda)$, is derived based on $R_{rs}^{M99+ship}(\theta,\varphi)$ and $b_{bp}(\lambda)$. The bidirectional effect corrected reflectance, $R_{rs}^{M99+ship}(0,0)$, is then calculated using the following equation:

$$\boldsymbol{R_{rs}^{M99+ship}(0,0,\theta_0,\lambda) = \left[G_0^w(0,0,\theta_0,\lambda) + G_1^w(0,0,\theta_0,\lambda) * \frac{b_{bw}(\lambda)}{k(\lambda)}\right] * \frac{b_{bw}(\lambda)}{k(\lambda)} + \left[G_0^p(0,0,\theta_0,\lambda) + G_1^p(0,0,\theta_0,\lambda) * \frac{b_{bp}(\lambda)}{k(\lambda)}\right] * \frac{b_{bp}(\lambda)}{k(\lambda)}} \tag{7}$$

where k is the summation of $\alpha(\lambda), b_{bp}(\lambda)\ and\ b_{bw}(\lambda)$. $G_0^w, G_1^w, G_0^p, G_1^p$ are model coefficients for water and particles and are dependent on angular geometry and phase function but independent of water IOPs (Lee et al., 2011).

2.2.2.2.6 *Water types clustering and data quality evaluation*

Optical water types clustering methods can generally be grouped into two categories. The first category focuses on the spectral magnitude of R_{rs}, such as in Le et al. (2011), Moore et al. (2009, 2014), and Jackson et al. (2017). The second category considers the spectral shape of R_{rs} for optical water types clustering. For example, Wei et al. (2016) (hereafter referred to as W16) compare the target spectral shape to a database composed of various global waters, divided into 23 water types including clear blue oceanic waters (type 1) and yellowish sediment-laden waters (higher types). W16 has been proven effective in categorizing various water types and can also be used to evaluate the quality of independent above-water spectra (Barnes et al., 2019), and it is therefore used also in this research. As it focuses on the spectral shape of R_{rs} rather than its magnitude, this shape-based classification method minimizes the effect of R_{rs} magnitude on the water types clustering. The subsequent quality assurance also follows method developed by W16:

Step 1: After applying the corrections for sky glint, ship perturbation and BRDF effects on R_{rs}^{0+}, the final reflectance is denoted as R_{rs}, which was convoluted to the corresponding Sentinel 3A-OLCI 11 bands from 400 to 709 nm using the Sentinel-3A OLCI Spectral Response Functions (SRF) available from the European Space Agency (2021). Sentinel-3A OLCI bands are considered in this study, since the products generated from this satellite are the main focus of a broader program on the coast of British Columbia (Giannini et al., 2021). However, the adopted approach can easily be extended to any satellite-derived R_{rs}^{0+}. The seven selected OLCI spectral bands (412, 443, 490, 510, 560, 665 and 681 nm) are the closest to those adopted by W16.

Step 2: Each OLCI R_{rs} spectrum was normalized to the root-sum-squares of R_{rs} corresponding to all wavelengths of the spectrum:

$$\boldsymbol{nR_{rs}(\lambda)} = \frac{\boldsymbol{R_{rs}(\lambda)}}{\sqrt[2]{\boldsymbol{\sum_{i=1}^{n} R_{rs}(\lambda_i)^2}}} \qquad (8)$$

where i =1, …,7 indicates each specific band. Each spectrum was assigned to one of the W16’s water types by calculating the “spectral angle”, $\cos\beta$, between the predefined reference spectrum, $nR_{rs}{}^{*}$, and nR_{rs} (Kruse et al., 1993):

$$\boldsymbol{\cos\beta} = \frac{\sum_{i=1}^{n}[\boldsymbol{nR_{rs}}^{*} * \boldsymbol{nR_{rs}}]}{\sqrt{\sum_{i=1}^{n}[\boldsymbol{nR_{rs}}^{*}(\boldsymbol{\lambda_i})]^2 \sum_{i=1}^{n}[\boldsymbol{nR_{rs}}(\boldsymbol{\lambda_i})]^2}} \qquad (9) \quad .$$

Step 3: A quality score is computed as the ratio of the number of wavelengths in nR_{rs} falling within the upper and lower bounds of $nR_{rs}{}^{*}$ given by the corresponding W16 water type. Five quality assurance (QA) scores are possible in this analysis (1.00, 0.86, 0.71, 0.57, 0.43), corresponding to 7, 6, 5, 4 or 3 wavelengths of nR_{rs} falling within the range of one of the W16 water types. Spectra with a QA >= 0.71 were deemed of high quality and used for further analysis.

2.2.2.3 FerryBox ancillary data

Ancillary data were collected with a FerryBox system measuring salinity (PSU) with a SeaBird SBE45 thermosalinograph, Chl-a concentration (ug l^{-1}) with a WET Labs ECO Triplet fluorometer, and CDOM fluorescence (ppb) and turbidity (NTU) with a WET Labs ECO Triplet BBFL2 scattering fluorescence sensor. Data processing details, including biofouling correction of the sensors and quenching correction for Chl-a measurements, are reported in Travers-Smith et al. (2021).

2.3 Results

2.3.1 Meteorological flags

Flags 1 and 2 were defined in Section 2.2.2.2.2. The mean (u), standard deviation (σ), and the calculated threshold (u^{*}) for r used to define meteorological Flag 3 (Eq. 1) for the four weather conditions are displayed in Table 2. Generally, rainy conditions are associated with the lowest mean value of r (0.86 +/- 0.05), and the defined range for this weather condition is r<0.92. The value of u^* discriminating between overcast and variable cloudy conditions is 1.1, while clear sky conditions exhibited the highest average of r (1.29, +/- 0.04), and u^*=1.26 is obtained between clear sky and variable clouds. Figure 3 illustrates the variability of r and the associated humidity measurements and photographs of the sky for June 27, 2016, which experienced different cloudy conditions. Note that for cloudy conditions, r is mostly lower than 1.26, thus allowing successful isolation of such measurements, as confirmed by the confusion matrix (Table 3). The matrix shows that clear sky conditions are correctly classified in about 98.5% of the measurements, which allows us to easily flag all other sky conditions (cloudy, overcast, rainy) unsuitable for analysis. However, it is important to note that the defined thresholds were ineffective in resolving variable cloud conditions, as about 32% were erroneously classified as clear sky conditions. Still, the r defined for clear sky conditions was implemented in PySciDON (Vandenberg et al., 2017) as part of our operational analysis of valid spectra, and all approved (not flagged) E_s spectra were further inspected for possible cloudy conditions.

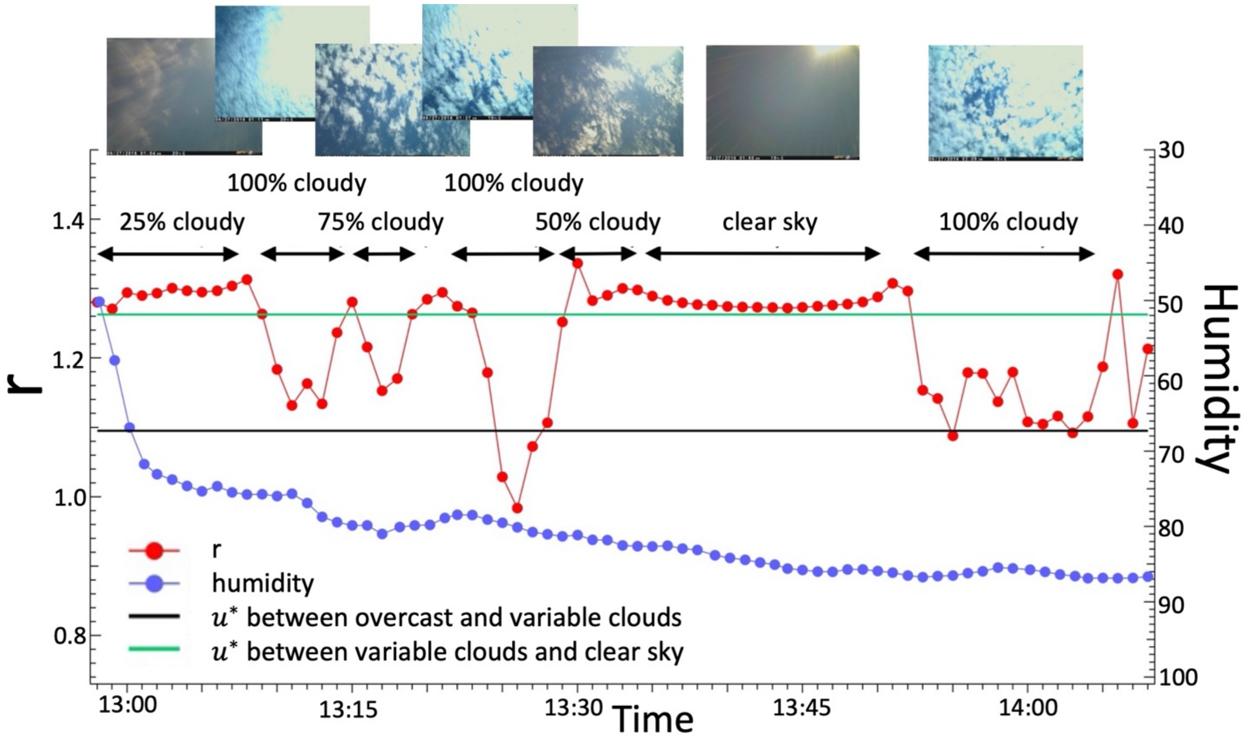

Figure 3| Plot of humidity and r=E_s (λ = 720 nm) / E_s (λ = 370 nm) of June, 27, 2016 which experienced different cloudy conditions. The sky images above correspond to sky conditions at a specific time. The duration of the specific sky condition is indicated by the black arrow lines.

Table 2| Mean, standard deviation, and the r=E_s (λ = 720 nm) / E_s(λ = 370 nm) range between the four weather condition groups.

Group	Mean	Std. Deviation	r range
Rainy	0.86	0.05	< 0.92
Overcast	1.02	0.08	> 0.92 and < 1.1
Variable clouds	1.19	0.1	> 1.1 and < 1.26
Clear sky	1.29	0.04	> 1.26

Table 3| Confusion matrix of four groups of weather conditions.

	Predicted Group Membership (%)			
In-situ Groups	Rainy	Overcast	Variable cloudy	Clear sky
Rainy (N=164)	97.6	2.4	0	0
Overcast (N= 212)	12.7	76.4	9.9	0.9
Variable cloudy (N= 401)	2.2	14.0	51.9	31.9
Clear sky (N= 582)	0.3	0.2	1.0	98.5

2.3.2 R_{rs}^{0+} calculation

SAS-ST data collected in the longitude range (W123.936°, W123.348°) were divided in 49 bins (0.012° longitude step), each corresponding to ~900 m on the ground, which approximates a 3 Sentinel-3A OLCI pixels window as used in Giannini et al. (2021). For the sky glint correction

(R_{rs}^{M99}), these sites were split into groups corresponding to their proximity to two meteorological stations maintained by the Canadian government. Wind speed measurements were taken from Entrance Island (Environment and Climate Change Canada, 2021a) for longitudes between W123.936° and W123.636° (sites 1-25), and from Halibut Bank (Environment and Climate Change Canada, 2021b) for longitudes between W123.636° and W123.348° (sites 26-49). The measured wind speed ranged from 0.7 to 10.7 m/s with the corresponding ρ_s ranging from 0.0355 to 0.0480 (Mobley, 1999). The ρ_s correction typically resulted in a decrease in reflectance for clear waters with the lowest R_{rs} of 48% (blue bands) and 14% (green bands), while typical turbid waters decreased by 27% (blue bands) and 8% (green bands).

Sites 8 to 32 on July 6, 2016, provided data over the waters with the lowest turbidity (turbidity < 2.0 NTU; i.e., <0.5 mg/l)., and the R_{rs}^{M99} from these cases was therefore used to evaluate the correction for the ship superstructure. The R_{rs}^{M99} values of 0.00196 ± 10^{-4}, $0.00202 \pm 8.1*10^{-5}$, $0.00109 \pm 5.7*10^{-5}$, $0.00062 \pm 4.2*10^{-5}$ sr^{-1} were found for 450, 550, 650, 750 nm, respectively. As seen in Figure 4A, there was no indication of an increase in reflectance as the rotator angle approaches from its maximum to minimum values (from -22.5° to -46.7°, corresponding to a distance from the ship wall of 20.9 m and 15.5 m, respectively). At distances below 14 m (α = -51.2°), a decrease in $R_{rs}^{M99}(780)$ was deemed indicative of interference from the ship shadow. Data corresponding to a rotator angle lower than -50° were therefore removed from further analysis. The measured $R_{rs}^{M99}(780)$ corresponds to R_{rs}^{ship}, and the histogram in Figure 4B shows a mean value of u= 0.000612 sr^{-1} and a corresponding standard deviation of σ =0.000030 sr^{-1}. Considering the mean value and a confidence level of 2σ, corresponding to 95%

of the Level 3A $R_{rs}^{M99}(780)$, the retrieved R_{rs}^{ship} was 0.00055 sr^{-1}. This R_{rs}^{ship} value ensures longitude-binned Level 4 $R_{rs}^{M99+ship}(\lambda)$ in the infrared bands from clearest water close to zero and non-negative, and it may vary for a different ship superstructure environment (Hooker and Morel 2003). The $R_{rs}^{M99+Ship}$ value for the clearest water was on average decreased to 0.00141, 0.00147, 0.00054, 0.00007 sr^{-1} for the 450, 550, 650, 750 nm bands, respectively. The R_{rs}^{Ship} correction factor consisted of about 13%, 7% and 22% of the R_{rs}^{M99} for the waters with higher turbidity from the Fraser River plume in the blue, green and red regions of the spectrum, respectively, while it was negligible for spectra collected in coccolithophore bloom conditions.

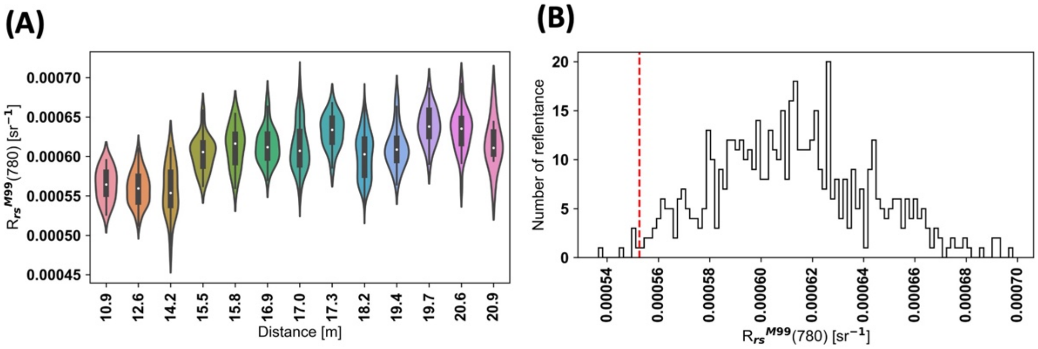

Figure 4|**(A)** The violin plot of L3a resolution $R_{rs}^{M99}(780)$ [sr^{-1}] (N=725) and the water surface footprint in relation to the ship wall distance for July 06, 2016. It is noted that at a distance lower than 14.2 m (α = -51.2°), there is a decrease in $R_{rs}^{M99}(780)$, which indicates the ship shadow influence observed when $\alpha < -50°$; **(B)** The histogram of $R_{rs}^{M99}(780)$ [sr^{-1}] (N=561) for the dataset after deleting 164 spectra influenced by ship shadow. The red dashed line indicates the value determined to represent superstructure contributed reflectance (R_{rs}^{ship} = 0.00055 sr^{-1} for this research).

The IOPs-based BRDF correction was applied to generate the final reflectance, R_{rs}. The R_{rs} dataset was divided into two groups, since the optical properties vary considerably in the presence of a bloom: Group 1 (high and low turbidity waters with no coccolithophore bloom) corresponding to 11 days from June 26 to August 14, 2016 (N=513 spectra), and Group 2 (coccolithophore bloom) corresponding to 5 days from August 15 to August 25, 2016 (N=213 spectra). Figure 5 shows representative R_{rs} spectra for Group 1 and Group 2, and Appendix A Section 2 in the supplementary material shows the summary plot of R_{rs}, together with the accompanying E_s, L_i, L_t for the sampled days. The results of the BRDF correction (Figure 6) show wavelength-dependent differences defined by the percentage difference ε:

$$\boldsymbol{\varepsilon} = \left(\frac{\boldsymbol{R_{rs}}}{\boldsymbol{R_{rs}^{M99+ship}}} - \mathbf{1}\right) * \mathbf{100} \qquad (10)$$

Noticeably, R_{rs} is lower than $R_{rs}^{M99+ship}$ by 5 to 10%, with the more significant differences found at green wavelengths (Figure 6).

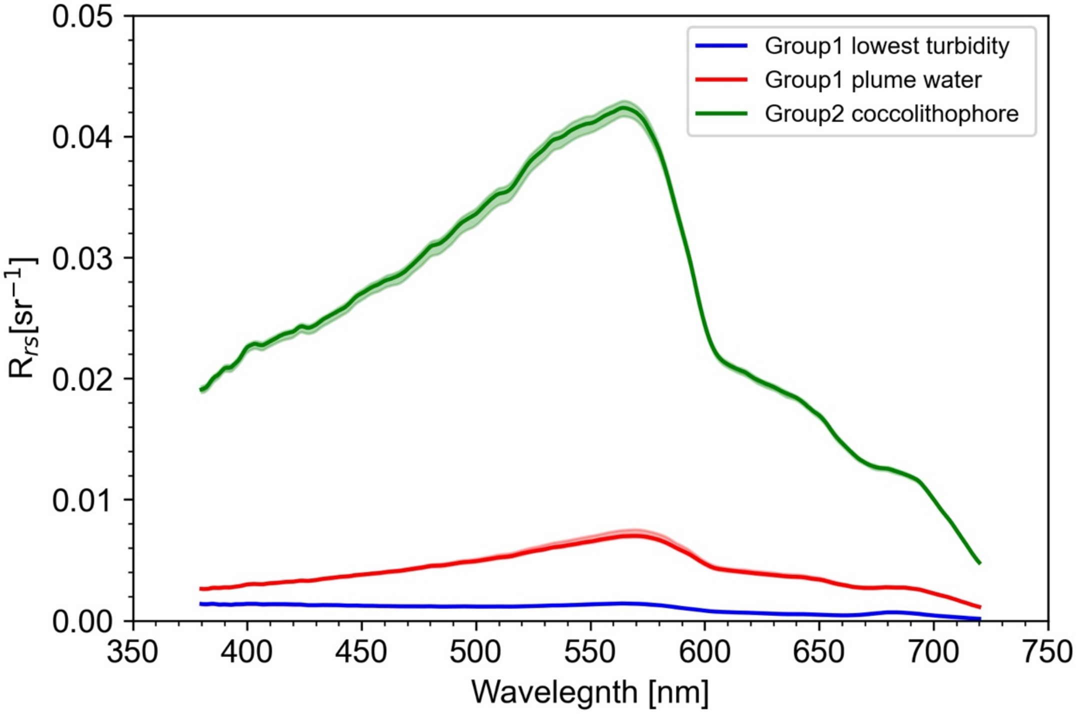

Figure 5| Representative R_{rs}sr^{-1}] with their median (solid lines) and 1st and 3rd interquartile range (shaded areas) based on a ~900 m range, showing typical lowest turbidity, typical plume, and coccolithophore bloom from July 06, 2016, and August 22, 2016.

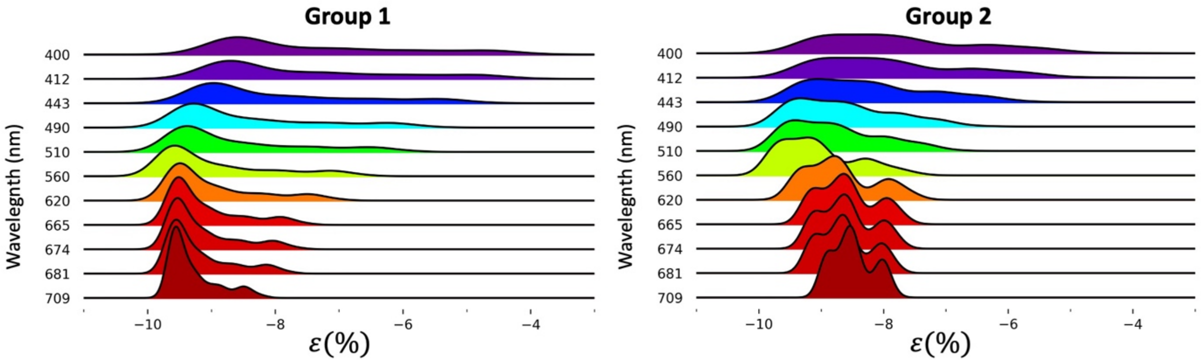

Figure 6| Joyplot for Group 1 (non-coccolithophore bloom conditions) and 2 (coccolithophore bloom conditions) of BRDF correction percentage difference ε for Sentinel-3A bands from 400 to 709 nm.

2.3.3 Quality check and optical water types clustering

For Group 1 (N=513), 92% of the nR_{rs} presented a QA score equal to or higher than 0.71 (Figure 7A, B), meaning that at least five out of seven at specific wavelengths (412, 443, 490, 510, 560, 665 and 681 nm) of individual nR_{rs} spectrum are within the $nR_{rs}{}^{*}$ range for each water type cluster defined by W16. Also, 60% of the spectra have a score of 1.0; the majority of these spectra belong to water type 11, i.e. medium- and high-reflectance waters, as indicated in Figure 7C and D. About 8% (N=41) of the spectra showed the lowest QA score of 0.57, and among these, 78% were found in water type 9. These waters exhibit the lowest reflectance in the dataset, corresponding to the clearest water types. We further investigated the possible source of the low QA scores and found that for these 41 spectra, the nR_{rs} corresponding to bands centred at 490 nm and 510 nm fell out of the boundary defining the W16 water types (Figure 7E). For Group 2 (N=231), 94% of the nR_{rs} showed QA score equal to or higher than 0.71 (Figure 8A, B). Figures 8A and B also show that 78% of the spectra are scored as 1.0. The majority belongs to water type 11, with reflectances evenly distributed across the whole range, as indicated in Figures 8C and D. However, the method reported by W16 does not consider algal bloom conditions, and as such it is not appropriate for evaluating all the spectra in Group 2. Nevertheless, the QA evaluation showed a higher percentage of high-quality scores than for Group 1, likely due to the high reflectance signal measured during the coccolithophore bloom conditions. In these conditions, only about 7% (N=15) of R_{rs} showed a QA score lower than 0.71, mainly from water type 11 (Figure 8A,B). Further analysis of these low QA score spectra showed that bands centred at 490 nm, 510 nm, and 560 nm were not included in any W16 water type (Figure 8E).

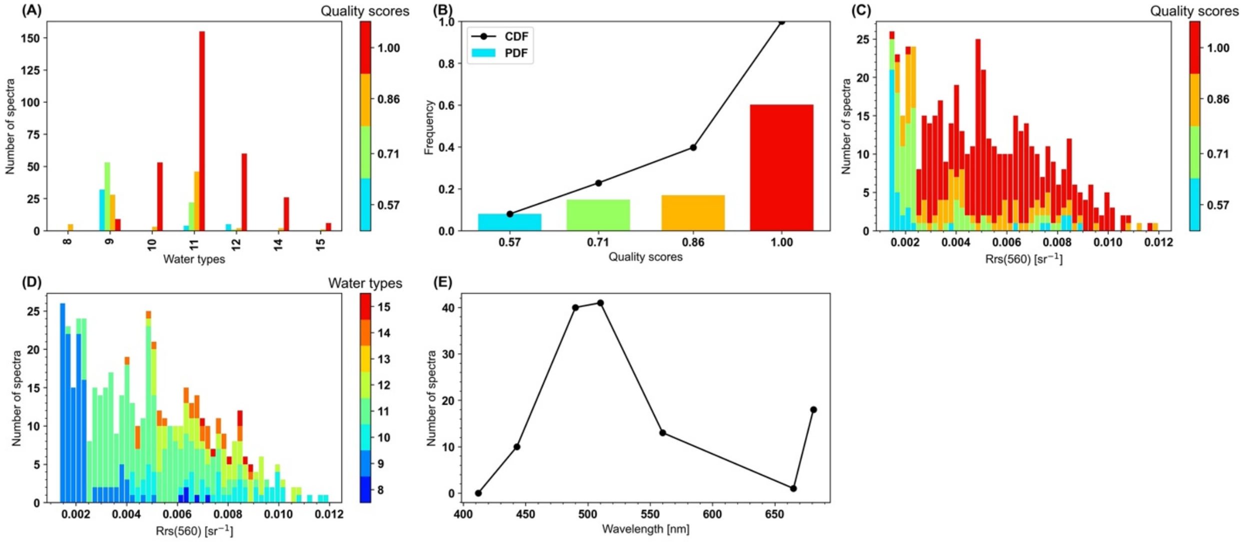

Figure 7| QA quality assurance results for Group 1. **(A)** Bar plot of the number of points at each water type and each quality score; **(B)** Frequency plot of each quality score, PDF represents probability density function, and CDF represents cumulative distribution function; **(C)** Histogram of $R_{rs}(560)$ colour coded by quality scores; **(D)** Histogram of $R_{rs}(560)$ colour coded by water types; **(E)** Number of points fall out the range of each QA cluster in that wavelength for 41 points from Group1 which has a score <0.71.

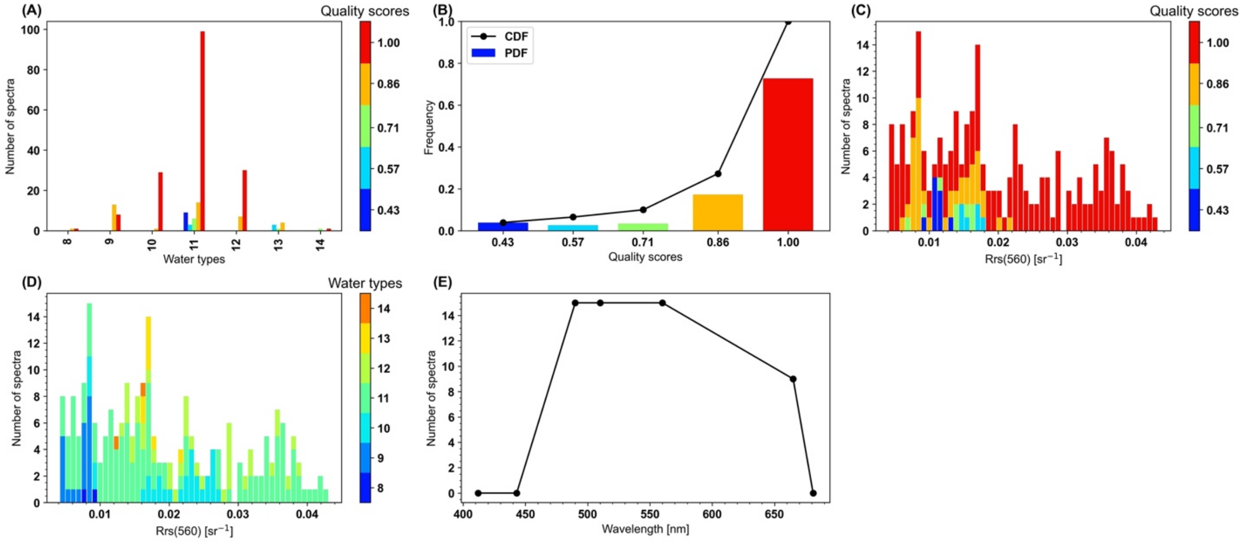

Figure 8| QA quality assurance results for Group 2. **(A)** Bar plot of the number of points at each water type and each quality score; **(B)** Frequency plot of each quality score; **(C)** Histogram of $R_{rs}(560)$ colour coded by quality scores; **(D)** Histogram of $R_{rs}(560)$ colour coded by water types; **(E)** Number of points fall out the range of each QA cluster in that wavelength for 15 points from Group2 which has a score <0.71.

For each group and water type, the R_{rs} varied in magnitude but presented a similar shape (Figure 9 and 10). The nR_{rs} from Group 1 is clustered into optical water types 8 to 15, excluding 13 (Figure 9B). The R_{rs} in Group 1 ranged from 0.001 – 0.006 sr^{-1}, 0.001 – 0.01 sr^{-1}, and 0.0005 – 0.0035 sr^{-1} in the blue, green, and red bands, respectively (Figure 9A). Specifically, the highest R_{rs} (~ 0.01 sr^{-1} at 560 nm) are observed within water types 10 and 11, which are generally associated with slightly higher turbid waters (Figure 11C); the lowest R_{rs} (< 0.002 sr^{-1}) are observed in many of the water types and are associated with low turbidity (< 2.0 NTU; Figure 11C). For Group 2, dominated by coccolithophore bloom conditions, the nR_{rs} are clustered into optical water types 8 to 14 (Figure 10B). For these waters, the lowest R_{rs} at 560 nm (<0.01 sr^{-1}) are associated with oceanic waters (>26 PSU; Figure 12A), which in turn are characterized by lower turbidity (< 3.0 NTU), higher Chl-a (>14.0 ug l^{-1}), and lower CDOM (< 2.0 ppb). The highest R_{rs} at 560 nm (0.03-0.04 sr^{-1}) are for water types 11 and 12, and correspond to the highest turbidity (> 5.0 NTU) and CDOM (> 2.2 ppb), and lowest Chl-a (< 3.0 ug l^{-1}).

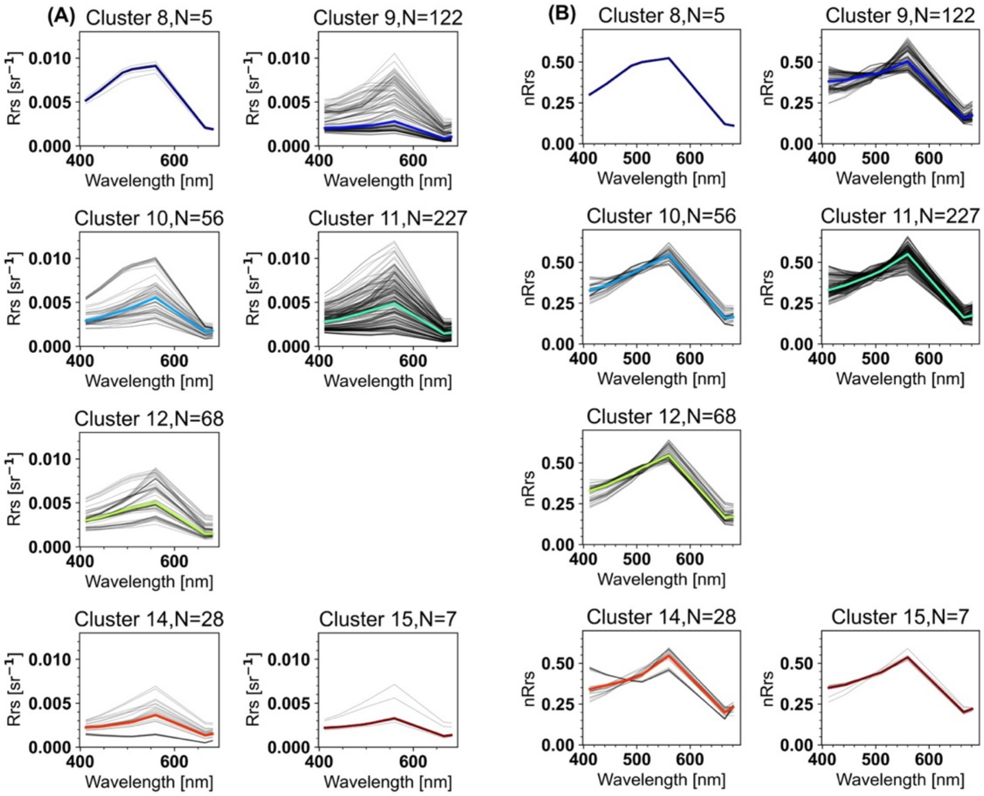

Figure 9| Plots of SAS-ST reflectance R_{rs} [sr^{-1}] **(A)** and normalized reflectance nR_{rs} **(B)** for 513 points from Group 1. Radiometry measurements are clustered into optical water types 8 to 15, excluding 13. A coloured line in each water type indicates the median of the cluster.

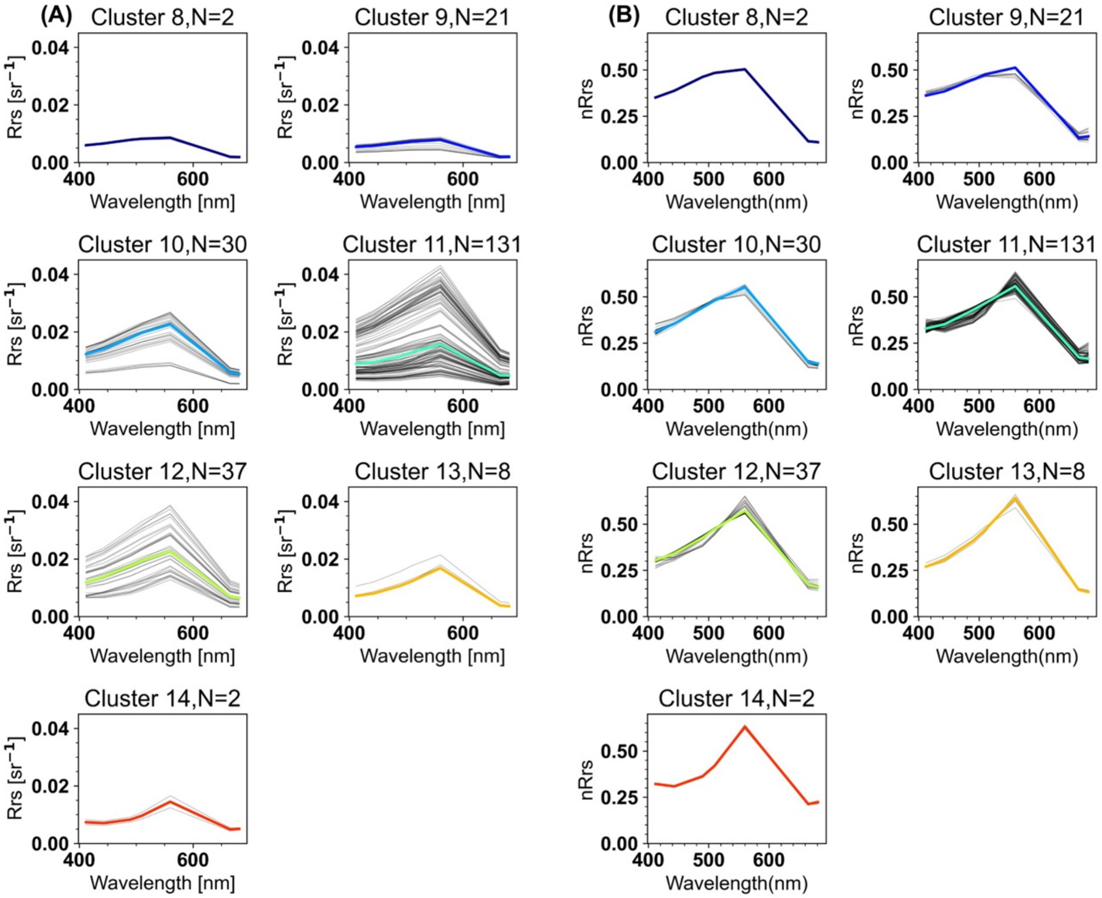

Figure 10| Plot of SAS-ST reflectance R_{rs} [sr^{-1}] **(A)** and normalized reflectance nR_{rs} **(B)** for 231 points from Group 2. Radiometry measurements are clustered into optical water types 8 to 14. A coloured line in each water type indicates the median of the cluster.

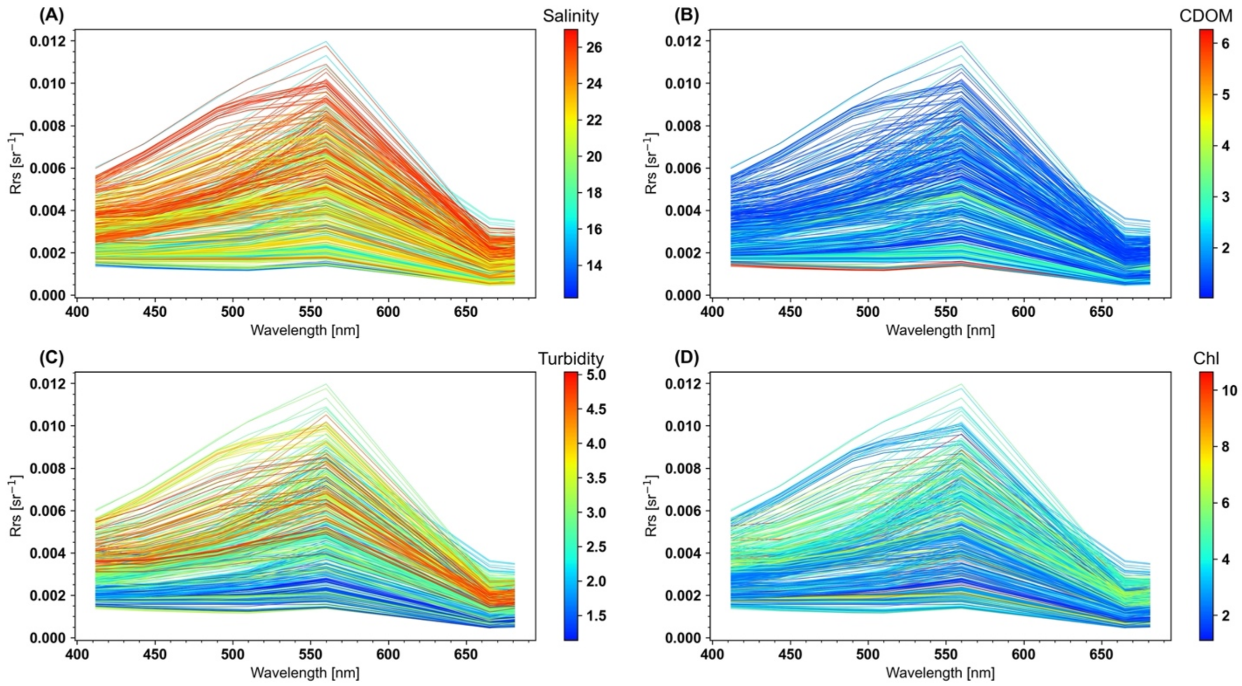

Figure 11| Reflectance R_{rs} [sr^{-1}] from Group 1, which is colour-coded in the corresponding **(A)** Salinity (PSU), **(B)** CDOM fluorescence (ppb), **(C)** Turbidity (NTU), and **(D)** Chlorophyll (ug/l) values.

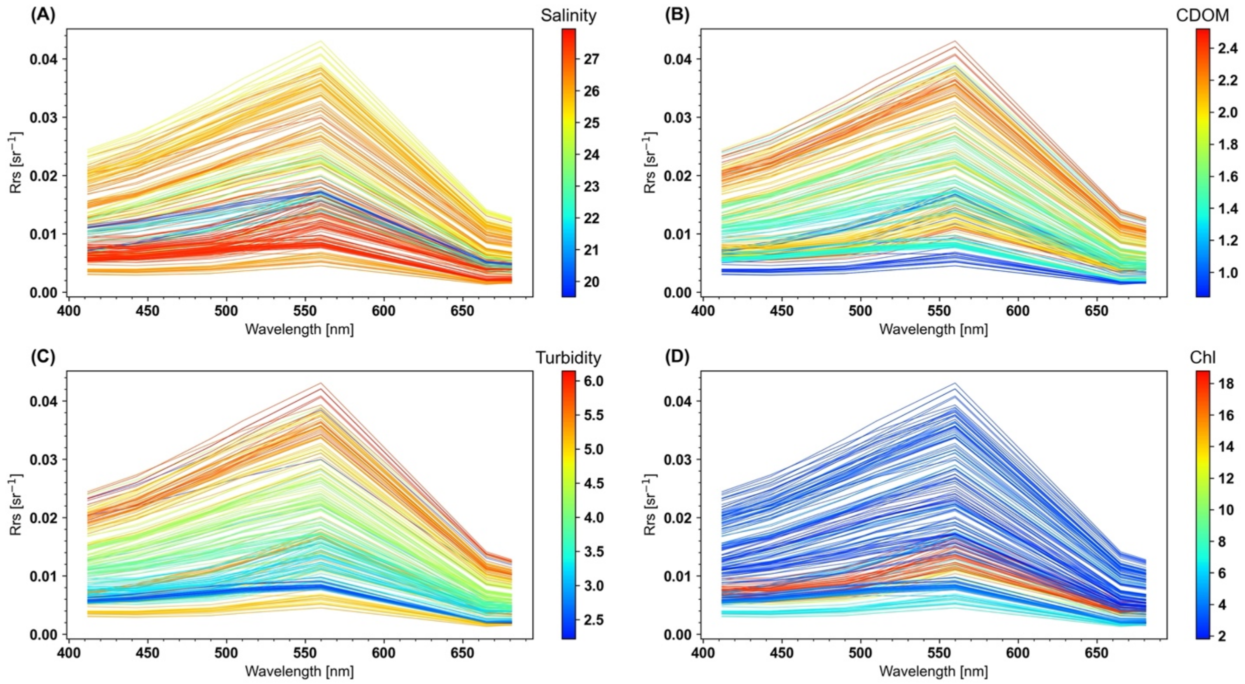

Figure 12| Reflectance R_{rs} [sr^{-1}] from Group 2, which is colour-coded in the corresponding **(A)** Salinity (PSU), **(B)** CDOM fluorescence (ppb), **(C)** Turbidity (NTU), and **(D)** Chlorophyll (ug/l) values.

2.4 Discussion

Our results show that optimizing the geometry of data acquisition, filtering data acquired under unstable illumination conditions (e.g., dawn/dusk, cloudy and rainy), and correcting for skylight radiance, ship superstructure, and BRDF effects, allowed for R_{rs}^{0+} data retrieval with high quality when compared with the W16 quality assurance dataset.

The first consideration for optimal data quality is the geometry of data acquisition (Mobley, 1999; Hooker and Morel 2003; Zibordi et al., 2006; Simis and Olsson 2013; Garaba et al., 2015; Brando et al., 2016; Vansteenwegen et al., 2019; Tilstone et al., 2020). Here, with optimal configuration, the spectral measurements were acquired on the non-sunlit side of the ferry to minimize the reflected ferry signal on the above-water radiance measurements (Hooker and Morel, 2003), and at an adapted sensor viewing zenith angle to avoid ship superstructure shadows and an optimal sensor-Sun azimuth angle to minimize the skylight radiance signal on the above-water radiance measurements (Mobley, 1999). Various skylight radiance correction approaches are available (e.g., Mobley, 1999; Ruddick et al., 2006; Lee et al., 2010; Groetsch et al., 2017) requiring different complexity of input data to successfully correct for skylight radiance. For instance, the method suggested by Gege (2014) and Groetsch et al. (2017) applies a three-component model, in which, using optimized local IOPs, it corrects for the residual sun and sky glint signal on the above-water measurement. We tested (analysis not shown here) this approach with a small set of IOPs measurements collected concomitant to some of the SAS-ST data, and the results were similar to those obtained with the method by Mobley (1999). Although Mobley's method is commonly used, the ρ_s factor is not wavelength-dependent, resulting in higher uncertainties for longer wavelengths (Lee et al., 2010). Still, for similar geometry and environmental conditions (wind speed < 13.0 m/s and clear skies), Garaba and Zielinski (2013) showed that Mobley's method performed similarly to three other approaches, with the advantage of ensuring non-negative R_{rs}^{0+} retrievals in the near-infrared. Also, uncertainties in the wind speed impact the ρ_s factor, especially in the blue bands (Mobley, 1999).

The ship-specific superstructure correction factor R_{rs}^{ship} was determined as 0.00055 sr^{-1}. Although this factor is not commonly addressed in above-water radiometry measurements (e.g., Simis and Olsson 2013; Brando et al., 2016), it can cause significant uncertainties in the final

R_{rs}^{0+}. Talone and Zibordi (2019) have shown that the structure signal (in this case, a fixed tower covered with a white sheet) was relatively more pronounced in the near-infrared than at visible wavelengths, and decreased with the inverse square of the distance between the platform and the sensor footprint. For a similar distance as in our study (15-21 m), Talone and Zibordi (2019) estimated a tower perturbation factor of about 10% to 3% for the 750-800 nm range, resulting in R_{rs}^{ship} = 0.00002 sr^{-1} at 780 nm. This value is one order of magnitude lower than the value determined for the QoOB, likely because of the larger structure of the QoOB (19 m in height and 139 m in length) compared with the experimental tower used by the authors (15 m in height and ~10 m in length). For a smaller ferry, the Queen of Alberni, using the same SAS-ST and ship perturbation approach adopted here, Gianinni et al. (2021) defined R_{rs}^{ship}= 0.00005 sr^{-1}, a value similar to the one in Talone and Zibordi (2019).

A correct evaluation of the dependence of the measured signal on the viewing geometry and the bidirectional effects (Morel and Gentili 1996; Morel et al., 2002; Zibordi et al., 2009; Lee et al., 2011) is important for validating satellite-based retrieved reflectance, or water radiance (Zibordi et al., 2009; Talone et al., 2018) and comparing above-water radiometric data acquired under different geometric conditions (Wei et al., 2016). Here, a BRDF correction was required because the data quality was evaluated against the W16 global R_{rs}^{0+} database, composed of reflectance measurements acquired with a nadir viewing geometry. The BRDF correction was found to decrease R_{rs}^{0+} in this research by ~5-10%, as also found by Talone et al. (2018).

The final evaluation of R_{rs}^{0+} is preferentially performed against *in situ* measurements of below water R_{rs} and/or measurements collected with various instruments at the same location (e.g., Hooker et al., 2002; Lee et al., 2010; Zibordi et al., 2016; Tilstone et al., 2020). However, collecting below-water R_{rs} is not possible with our measurement setup. Instead, our R_{rs} data set was evaluated against a global water dataset. This evaluation was conducted considering two different clusters of data: Group 1, representing clear and turbid waters and Group 2, representing coccolithophore bloom conditions (Ianson et al., 2018). Group 1 exhibited values of R_{rs} well within the ranges of those measured by Komick et al. (2009), Phillips and Costa (2017), Carswell et al. (2017), and Giannini et al. (2021) in the same region. Group 1 consisted of a diverse group of waters, as indicated by the large salinity range (12 to 27 PSU) corresponding to Fraser River plume to oceanic waters (Loos and Costa 2010; Traver-Smith et al., 2021). In these waters, the bio-optical constitutes were generally characterized by a large range of CDOM fluorescence (0.05-6 ppb) and turbidity (1-5 NTU). Higher R_{rs} values are associated with the lower salinity of the Fraser River plume and estuarine waters (Loos and Costa 2010; Phillips and Costa 2017; Travers-Smith et al. 2021). For Group 2, the R_{rs} spectra were well within the ranges observed by Moore et al. (2012), Neukermans and Fournier (2018) and Cazzaniga et al. (2021) for waters under coccolithophore bloom conditions. Specifically, Cazzaniga et al. (2021) have shown high values ($R_{rs}(550) \approx 0.03$ sr^{-1}) for the peak of a coccolithophore bloom, intermediate values ($R_{rs}(550) \approx 0.02$ sr^{-1}) for receding bloom conditions, and low values ($R_{rs}(550) < 0.01$ sr^{-1}) for the start and the end of bloom. Similarly, our spectra showed $R_{rs}(560) > R_{rs}(500)$ likely representing the start of the bloom (water types 11 and 12; Figure 10). Other spectra showed an increase at $R_{rs}(500)$(water types 8, 9, and 10), probably associated with a high concentration of detached coccoliths indicative of receding bloom conditions (Neukermans and Fournier, 2018; Cazzaniga et al., 2021).

The evaluation of R_{rs} data showed an overall high quality, with about 92% of Group 1 and 94% of Group 2 with a QA score >=0.71. A QA score <0.71 was only observed for 8% (N=41) of Group 1, and corresponded to the lowest R_{rs} for which the out-of-range wavelengths were 490 and 510 nm. This was not expected, since uncertainties of R_{rs} retrievals are mostly associated with shorter wavelengths (Mobley, 1999; Hlaing et al., 2013; Wei et al., 2020). However, the W16 method relies on normalizing R_{rs} at each wavelength with respect to the integral over all R_{rs} (Eq. 8). Erroneous values of R_{rs} at 412 and 443 nm can therefore influence the shape of the corresponding nR_{rs}, and consequently, the water type to which it belongs.

Although our protocols for R_{rs}^{0+} measurements with the SAS-ST followed rigorous criteria for data acquisition and processing, there is still a level of data variability and uncertainty that it is difficult to account for (Ruddick et al., 2019; Vabson et al., 2019; Tilstone et al., 2020; Alikas et al., 2020). These uncertainties may also explain the 8% of acquired spectra with lower quality (QA <0.71). Recent evaluations of international field-based radiometers (Tilstone et al., 2020), including similar Satlantic HyperOCR radiometers as those used here, indicated that the inaccuracies in downwelling-irradiance measurements resulted in the largest R_{rs} variability, especially for the blue (3.5%) and red (3.0%) wavelengths. The E_s spectra collected for this research at around solar noon (see Appendix A, Sec. 2) exhibited very low variability in clear-sky conditions; thus, we do not expect the same level of uncertainties reported in Tilstone et al. (2020). The quantification of specific uncertainties in R_{rs} measurements is challenging, especially considering the lack of simultaneous, below-water reflectance measurements. Our R_{rs} data showed high quality, and has been effectively used for the evaluation of atmospheric correction procedures for Sentinel-3A OLCI (Gianinni et al., 2021). To provide vicarious calibration for satellites, an uncertainty budget of the FRM is a requirement, which should be further investigated by accounting for the environmental conditions during data acquisition, such as in Alikas et al. (2020).

2.5 Conclusions

Validation of ocean colour satellite R_{rs} retrievals requires a large number of high-quality R_{rs}^{0+} matchups (Müller et al., 2015; Werdell et al., 2018; Valente et al., 2019). However, the availability of such matchups is often limited due to the difficulty of acquiring high-quality data over large spatial and temporal domains (Tilstone et al., 2020). These constraints are reported for many study regions (e.g., Valente et al., 2019, Tilstone et al., 2020, Gianinni et al., 2021), and it is specifically an issue along the west coast of Canada (Komick et al., 2009; Carswell et al., 2017; Hilborn and Costa, 2018; Gianinni et al., 2021). Autonomous radiometers mounted on fixed towers, such as AERONET-OC (Zibordi et al., 2006, 2009), the newest WATERHYPERNET hyperspectral network (Vansteenwegeno et al., 2019; Vanhellemont and Ruddick 2021) can also provide a large number of high-quality matchups. Another option is to utilize mobile platforms such as ships. We presented the protocols to deploy the SAS-ST instrument on a commercial ferry, together with the evaluation of the large volume of high-quality R_{rs}^{0+} data acquired along the coastal waters of BC, Canada. The summary of our results and recommendations are as follows:

1. The application of meteorological flags in PySciDon successfully identified 98.5% of the spectra as acquired under clear-sky conditions. The remaining 1.5% of E_s spectra were manually inspected.

2. The ship-specific superstructure perturbation signal amounted to R_{rs}^{ship}= 0.00055 sr^{-1}. This value is about 25% of the R_{rs}^{0+} signal in blue and green bands for relatively clear waters, and about ~10% in the same bands for waters with higher reflectance (Appendix A, Sec. 2). Therefore, an accurate estimate of R_{rs}^{ship} is critical to successfully retrieve the reflectance in blue and green bands, especially for low-reflectance waters.

3. The correction for the BRDF effects lowers R_{rs}^{0+} by ~5-10%, allowing for proper comparison among R_{rs}^{0+} measurements from the literature and matchups used to validate satellite retrievals.

4. Quality evaluation showed overall high scores: ~92% of Group 1 and 94% of Group 2 are associated with a score >=0.71, implying that the data can be used for validation of atmospheric corrected satellite-retrieved R_{rs}.

The methodology presented here is adaptable to other ships, to enable surveys of different water types and complement fixed platforms such as AERONET-OC (Zibordi et al., 2009) and WATERHYPERNET (Vanhellemont and Ruddick 2021). Further work will focus on providing the error budget based on estimates of the uncertainty contribution from the sensor's calibration, data processing and environmental variability, essential for FRMs (Zibordi et al., 2015b; Vabson et al., 2019; Tilstone et al., 2020; Alikas et al., 2020).

Chapter 3: A machine learning algorithm for monitoring coccolithophore blooms using autonomous shipborne *in situ* and Sentinel-3A reflectance data in the Salish Sea, Canada

Abstract

Coccolithophores, a unique phytoplankton species, are enveloped in calcium carbonate plates called coccoliths, which can be shed during the later phase of the blooms, greatly enhancing water reflectance. These organisms influence the biogeochemical processes related to oceanic calcium and carbonate cycling due to their crucial role in calcite generation and carbon exportation within marine ecosystems. This study is focused on analyzing the spectral characteristics of the remote sensing reflectance (R_{rs}) during coccolithophore blooms that occurred in 2016 in the Salish Sea, Canada, utilizing the temporally continuous hyperspectral radiometric dataset obtained from the SAS Solar Tracker (denoted as SAS-ST) radiometer deployed onboard a commercial ferry, alongside satellite images from the Ocean and Land Colour Instrument (OLCI) aboard the Sentinel-3A satellite. This research succeeded in identifying the occurrence of a large coccolithophore bloom and further categorized the bloom spectra into the growing and decaying stages. The comparison of Sentinel-3A OLCI satellite spectra versus SAS-ST *in situ* data indicates that R_{rs} acquired by OLCI is underestimated, especially in the 400-443 nm range and during the decaying phase. A modified machine learning algorithm is developed based on wavelengths from 490 nm to 709 nm, resulting in an increase in overall prediction accuracy for OLCI-measured coccolithophore spectra from 79.4% to 89.1%, an improvement in the accuracy for detecting decaying blooms from 29.5% to 65.3%, and an increase in the Kappa coefficient from 0.14 to 0.66.

3.1 Introduction

Coccolithophores are characterized by a unique exoskeleton encompassing an assemblage of individual calcium carbonate plates, called coccoliths, which make them distinctive among phytoplankton species (Young et al., 2003). These marine organisms synthesize particulate organic carbon (POC) through the process of photosynthesis and generate particulate inorganic carbon (PIC) via calcification (Krumhardt et al., 2017), which exerts an impact on the oceanic calcium and carbonate cycling and associated biogeochemical process (Balch et al., 2011; Bach et al., 2015). Within diverse coccolithophores species, *Emiliania huxleyi* emerges as the most prevalent species, flourishing from tropical to subpolar oceans (Holligan and Balch, 1991; Tyrrell and Merico, 2004). Rising global temperatures linked to climate change may cause a significant increase in coccolithophore populations across most oceanic waters, with research based on field data and satellite remote sensing indicating their migration towards higher latitudes in response to these changes (Winter et al., 2014; Balch, 2018; Neukermans et al., 2018).

Their ecological importance and sensitivity to climate changes underscores the necessity for coccolithophore monitoring, with satellite remote sensing serving as an important tool due to the scarcity of *in situ* observations (Balch and Mitchell, 2023). Spectrally, these organisms increase the total water reflectance due to the high light backscattering by coccospheres and, in the later phases of the bloom, by detached coccoliths (Balch, 2018). As a result, they impart a vivid milky-turquoise hue to the ocean, making these distinctive blooms readily detected using ocean colour satellite imagery (Gordon et al., 2001; Balch et al., 2005; Balch and Mitchell, 2023).

Advances in satellite technology have made satellites essential tools for monitoring coccolithophore blooms due to their capability to provide large-scale, synoptic views of oceanic conditions and phytoplankton distributions. These advancements have further facilitated the exploration of coccolithophore bloom extension across the global ocean and their migration towards higher latitudes as a response to climate change (Winter et al., 2014; Neukermans et al., 2018). Different methodologies have been established for identifying coccolithophore bloom occurrences from satellite observations. For instance, Brown and Yoder (1994) initially applied a coccolithophore detection flag based on thresholds of normalized water-leaving radiance (L_{wn}) and their ratios for three bands at 440 nm, 520 nm and 550 nm on Coastal Zone Colour Scanner (CZCS) imagery. Iglesias-Rodríguez et al. (2002) subsequently modified the coccolithophore bloom classification algorithm for application to the Sea-viewing Wide Field-of-view Sensor (SeaWiFS) imagery by making minor wavelength adjustments to 443 nm, 510 nm, and 555 nm and the corresponding thresholds. This algorithm, as coded into NASA's Ocean Colour processor (l2gen of SeaDAS), is also currently implemented on the Moderate Resolution Imaging Spectroradiometer (MODIS) and the Visible Infrared Imaging Radiometer Suite (VIIRS) imagery. In this implementation, $L_{wn}(510)$ is substituted by $L_{wn}(531)$ or $L_{wn}(489)$, respectively, an adjustment made while recognizing the potential for diminished efficacy (Moore et al., 2012; Cazzaniga et al., 2021). This algorithm, as coded into NASA's Ocean Colour processor (l2gen of SeaDAS), is also currently implemented on the Moderate Resolution Imaging Spectroradiometer (MODIS) and the Visible Infrared Imaging Radiometer Suite (VIIRS) imagery, with $L_{wn}(510)$

being substituted by $L_{wn}(531)$ or $L_{wn}(489)$, respectively, an adjustment made while recognizing the potential for diminished efficacy (Moore et al., 2012; Cazzaniga et al., 2021). Alternatively, remote sensing reflectance (R_{rs}) is used to produce optical water type membership maps, which portray the degree of membership to the given coccolithophore optical water type (Moore et al., 2012).

Other approaches for coccolithophore detection are the estimation of PIC concentration from ocean colour imagery, given that the optical PIC backscattering in the sea is primarily associated with coccolithophores and their detached coccoliths (Tyrrell et al., 1999; Smyth et al., 2002; Donlon et al., 2012). The larger PIC particles, predominantly associated with foraminifera and pteropods, contribute negligible backscattering per unit mass, and therefore exert minimal influence on optical properties (Balch et al., 1996). The standard NASA PIC algorithm is based on the particulate backscattering coefficient (b_{bp}, m^{-1}) derived from two or three spectral bands (Gordon et al., 2001; Balch et al., 2005). Mitchell et al. (2017) introduced a more recent methodology, known as the two-band colour index algorithm, which takes advantage of the relationship between PIC concentrations and differences in reflectance at green and red wavebands. The above PIC detection methods for coccolithophores rely on analyzing satellite reflectance data, applying algorithms that can distinguish high reflectance associated with coccolithophore blooms, and establishing thresholds based on empirical relationships between reflectance and coccolithophore concentrations (Balch and Mitchell, 2023).

Despite the extensive use of satellite observations and associated algorithms for coccolithophore bloom research, particularly in recent decades (Neukermans et al., 2018; Balch and Mitchell, 2023), very few *in situ* reflectance data associated with coccolithophores are documented in the literature. For example, Garcia et al. (2011), Iida et al. (2002), and Smyth et al. (2002) recorded only 16, 9, and 4 coccolithophore spectra, respectively, over several days of fieldwork. A notable exception is the study by Cazzaniga et al. (2021), which utilized *in situ* AERONET-OC measurements, autonomous multispectral radiometer systems deployed on fixed offshore structures that are part of the Ocean Colour component of the Aerosol Robotic Network (Zibordi et al., 2009). This setup allowed the study to capture four coccolithophore bloom events, each lasting approximately two months.

Given the scarcity of *in situ* coccolithophore bloom spectra, *in situ* hyperspectral measurements from Case 2 waters are needed to provide ground-truth data for satellite observations including the new hyperspectral satellite sensors, PACE (Werdell et al., 2019), PRISMA (Loizzo et al., 2018), EnMap (Guanter et al., 2015), and multispectral Sentinel-3 satellites. *In situ* data can also be used to calibrate and refine remote sensing algorithms, ensuring accurate representation of the biological and optical properties of coccolithophores across different environmental conditions. Such calibration is crucial for enhancing the reliability of satellite-derived estimates of coccolithophores and their associated PIC (Balch and Mitchell, 2023). Further, *in situ* spectral measurements are also important to fill knowledge gaps in space and time due to the inherent limitations in satellite spatial resolutions (300 to 1000 m) and data processing procedures. Although it is commonplace to generate 5-day, 8-day, or even monthly global composites of satellite imagery to address cloud cover and the temporal discontinuity of satellites (e.g., Brown and Yoder,1994; Iglesias-Rodríguez et al. 2002; Moore et al. 2012), this practice poses significant challenges. Temporal averaging of satellite data can obscure the fine temporal resolution required to detect critical changes in the reflectance of blooms at various coccolithophore developmental stages. Due to the rapid development and dissipation of coccolithophore blooms, frequent monitoring, potentially on a daily or even hourly basis, may be required to capture their distinct evolving stages accurately. Near-real-time information about coccolithophore blooms is crucial for managing fisheries, monitoring ecosystem health, and assessing broader environmental changes in marine systems (Balch and Mitchell, 2023). In contrast to satellite data, *in situ* observations, whether through autonomous moving platforms (e.g., Tilstone et al., 2020; Wang and Costa, 2022) or fixed platforms such as AERONET-OC (Zibordi et al., 2009) and WATERHYPERNET (Vanhellemont and Ruddick, 2021), offer a more temporally continuous dataset, that allows a better understanding of the dynamic of coccolithophore blooms than binned satellite data.

Existing methodologies for identifying coccolithophore blooms from satellite observations are primarily developed for Case 1 waters, where ocean colour variability is driven solely by phytoplankton and co-varying components (Sathyendranath et al., 2017; Balch and Mitchell, 2023). These existing remote sensing algorithms are based on two or three spectral bands, which primarily rely on knowledge about the water's optical properties. However, in complex Case 2 waters, such as the Salish Sea in this study, the optical properties are more variable and not always accessible, with significant optical constituents like coloured dissolved organic matter (CDOM) and suspended particles from the Fraser River plume. This variability makes it challenging to monitor coccolithophore blooms accurately in these regions, and models for satellite-based coccolithophore monitoring in Case 2 waters are scarce. Machine learning techniques, as discussed below, can overcome these challenges by learning directly from complex, high dimensional data without the need for prior knowledge of optical properties.

The proliferation of accessible machine learning algorithms, along with their demonstrated success in inference and classification tasks in the sciences, has driven their growing adoption in ocean remote sensing, including ocean colour remote sensing (Gray et al., 2024). Machine learning methods have been extensively applied in a range of tasks involving ocean colour data. For instance, machine learning algorithms have been developed to retrieve inherent optical properties (IOPs) from remote sensing reflectance (R_{rs}) data (e.g., Ioannou et al., 2013; Fan et al., 2021) . Additionally, machine learning has been employed to estimate chlorophyll-a (Chla) concentrations from satellite-derived reflectance in global waters (e.g., El-Habashi and Ahmed, 2019; Kolluru and Tiwari, 2022). In applying machine learning to coccolithophore bloom detection, Shutler et al. (2010) characterized bloom events in shelf seas and coastal zones affected by suspended particulates. Their approach leveraged both the spectral characteristics of dense coccolithophore blooms and their spatial and temporal features to distinguish true coccolithophore blooms from false positives caused by resuspended lithogenic sediments (Balch and Mitchell, 2023). After filtering the normalized water-leaving radiance (L_{wn}) to eliminate background suspended particulates signals, the filtered L_{wn} data were processed using the established spectral coccolithophore detection algorithm by Brown and Yoder (1994) for further coccolithophore classification. Essentially, this approach aligns with Brown and Yoder (1994) coccolithophore detection algorithm, with the addition of a preliminary step for background particle signal filtering.

To address the shortage of reflectance-based algorithms for monitoring coccolithophore blooms in Case 2 waters influenced by river plumes, my goal is to develop a robust methodology for detecting and classifying the developmental stages of these blooms, including growth and decay in Case 2 waters, using remote sensing data. The research integrates an unprecedented time series of daily hyperspectral above-water measurements of coccolithophore bloom spectra, collected using the SAS Solar Tracker radiometer (SAS-ST; Satlantic Inc./Sea-Bird) onboard a commercial ferry in the Salish Sea, British Columbia, Canada, with satellite imagery from the Ocean and Land Colour Instrument (OLCI) aboard Sentinel-3A. These large volumes of datasets are processed using advanced machine learning techniques to achieve the study's objectives. The specific objectives are: (1) to develop a novel machine learning algorithm trained on the SAS-ST *in situ* dataset to classify coccolithophore bloom stages based on their unique reflectance characteristics, and (2) to further apply the model to OLCI satellite imagery to enable large scale detection of coccolithophore bloom in optically complex Case 2 waters. This work contributes to the field of ocean colour remote sensing by providing a transferable framework for coccolithophore monitoring in coastal waters and advancing the understanding of coccolithophore bloom dynamics in complex aquatic environments.

3.2 Materials and methods

3.2.1 Study area

Situated in the southwestern region of Canada, the Salish Sea is an estuarine system, stretching approximately 200 km in length and 30 km in width, with a mean depth of 150 m (Figure 13). It comprises three main components: the Strait of Georgia (SoG), Puget Sound, and the Juan de Fuca Strait. This network of water bodies interfaces with the Pacific Ocean through the southern Juan de Fuca Strait and the northern Johnstone Strait. Due to the constriction of the northward route, the southern passage predominantly facilitates water exchange between the Salish Sea and the Pacific waters (Masson, 2002; Pawlowicz et al., 2019). An essential characteristic of the SoG is the considerable influx of freshwater from the Fraser River, which promotes southward estuarine circulation (Johannessen et al., 2003; Yunker and Macdonald, 2003). The resultant river plume traverses and occasionally pervades the entire central and southern areas of the SoG (Li et al., 2000; Halverson and Pawlowicz, 2008, 2011; Pawlowicz et al., 2017, 2019). The river plume contains elevated levels of total suspended matter (TSM) and coloured dissolved organic matter (CDOM), thereby generating optically complex waters characterized by high light attenuation, particularly during the spring and summer periods (Loos and Costa, 2010; Phillips and Costa, 2017). The outflow from the Fraser River typically culminates in a freshet around mid-June due to the melting of the snowpack (Masson, 2002; Masson, 2006). Given the substantial particulate outflow from the Fraser River, the Salish Sea exhibits considerable optical dynamics, thus characterizing it as an optically complex coastal system (Loos and Costa, 2010).

From a biological perspective, the Salish Sea typically experiences a cyclical pattern with an intense diatom-led spring bloom followed by relatively milder fall bloom events (Allen and Wolfe, 2013; Suchy et al., 2019; Marchese et al., 2022; Vishnu et al., 2022; Pramlall et al., 2024). The occurrence of the spring phytoplankton bloom is subject to interannual variations, primarily driven by factors such as the availability of light contingent on cloud cover, wind dynamic patterns, and the temporal occurrence of spring freshwater discharge (Collins et al., 2009; Masson and Peña, 2009; Allen and Wolfe, 2013; Suchy et al., 2019). Dinoflagellates constitutes this region's second most abundant group of phytoplankton, showing maximum biomass in summer and early autumn (Pospelova et al., 2010; Vishnu et al., 2022). Calcifying phytoplankton, such as coccolithophore (*Emiliania huxleyi*), are rarely found within the SoG (Haigh et al., 2015). However, in July and August 2016, concurrent with the data acquisition period for this research, the Salish Sea region witnessed an extraordinary coccolithophore bloom of *Emiliania huxleyi*, marking an unprecedented event in the recorded history of coccolithophore occurrences in this area (NASA 2016; Chandler et al., 2017; Simpson et al., 2022; Nemceka et al., 2023). Approximately 100 km northwest of the track of SAS-ST (Figure 13), water samples collected on August 14, 2016 revealed coccolithophore cell concentrations as high as 40,000 cells/mL in the bright turquoise waters (Esenkulova et al., 2021), significantly exceeding the typical concentrations of thousands of cells per milliliter in the literature and could be recognized as intense coccolithophore bloom (Hovland et al., 2014; Balch and Mitchell, 2023).

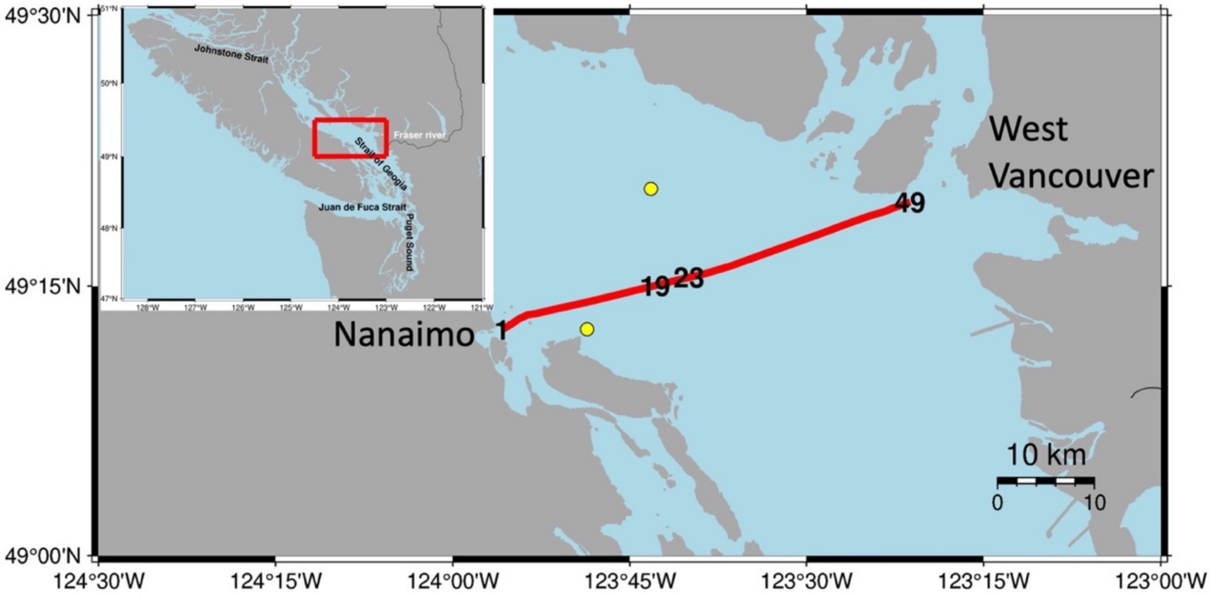

Figure 13| The Salish Sea study area. The red line indicates the track of the Queen of Oak Bay, approximately 55 km. The numbers indicate the location of the stations. Data was measured while the Queen of Oak Bay sailed from Departure Bay, Nanaimo, to Horseshoe Bay, West Vancouver, BC (in the direction from station 1 to 49). Two yellow dots are Entrance Island (49.21 N, 123.81 W) and Halibut Bank (49.34 N, 123.72 W) for local wind measurement used in SAS-ST R_{rs} calculation.

3.2.2 Dataset

To confidently utilize Sentinel-3A OLCI data in regions with coccolithophore blooms, an evaluation of the uncertainties of the remote sensing radiometric products is essential. To achieve this, ground truth above water radiometric data were collected using SAS-ST and processed following stringent protocols, serving as a reference for the satellite data. Secondly, optical constituents measured by the BC FerryBox system aided in understanding and classifying the diverse coccolithophore bloom spectra captured concurrently by SAS-ST. Finally, properly atmospherically corrected Sentinel-3A OLCI images underwent thorough screening to ensure reliable satellite data products for further R_{rs} evaluation.

3.2.2.1 ***In situ*** **Reflectance: SAS-ST**

SAS Solar Tracker, a suite of hyperspectral radiometers equipped with autonomous solar tracking capability, was installed aboard a ship of opportunity, the Queen of Oak Bay (QoOB) ferry, which traverses the Salish Sea multiple times daily. In addition to increased wavelength resolution provided by the hyperspectral capacity of SAS-ST (spectral ranges from 350 to 798 nm), SAS-ST also enables spatially continuous measurement of the water body when deployed on mobile platforms, different from stationary above-water sensors such as AERONET-OC (Zibordi et al., 2006, 2009) and WATERHYPERNET (Vanhellemont and Ruddick, 2021). SAS-ST data collection was scheduled during the ferry run from 12:50 to 14:30 local time in the spring and summer to approximately align with the image acquisition times of several operational ocean colour satellites. This research employs a dataset comprising 15 clear sky days from August 11, 2016, to August 30, 2016.

Raw SAS-ST data underwent calibration utilizing the PySciDON software (Vandenberg et al., 2017) and the application of the screening flags, followed by sky glint and ship perturbation corrections as detailed in Wang and Costa (2022). Specifically, the remote sensing reflectance was calculated following Mobley (1999) (denoted as R_{rs}^{M99}) to correct for skylight contributions through:

$$\boldsymbol{R_{rs}^{M99}(\lambda) = \frac{L_t(\lambda) - \rho_s L_i(\lambda)}{E_s(\lambda)}}$$

In the equation, the numerator corresponds to the water-leaving radiance, $L_w(\lambda)$, and ρ_s is the fraction of sky radiance (L_i) that is measured by the sea viewing sensor (L_t), with the value of ρ_s determined based on local wind speed measured at Entrance Island (49.21 N, 123.81 W) and Halibut Bank (49.34N, 123.72W) (Figure 13). Then, the ship superstructure introduced reflectance, R_{rs}^{ship}, was subtracted from R_{rs}^{M99}. The ship-specific superstructure correction factor, R_{rs}^{ship}, determined as 0.00055 sr^{-1} for the QoOB by Wang and Costa (2022), was subtracted from R_{rs}^{M99} through:

$$\boldsymbol{R_{rs}^{M99+ship}}(\boldsymbol{\lambda}) = \boldsymbol{R_{rs}^{M99}}(\boldsymbol{\lambda}) - \boldsymbol{R_{rs}^{ship}}$$

with $\boldsymbol{R_{rs}^{M99+ship}}$ representing sky glint and ship superstructure perturbation corrected reflectance. Lastly, $\boldsymbol{R_{rs}^{M99+ship}}$ was corrected for bidirectional effects following the inherent optical properties approach for optically complex waters proposed by Lee et al. (2011) with code developed by Wang and Costa (2022) to have the final reflectance for further analysis. The final reflectance (denoted as Rrs^{SST} hereafter) from each day were binned in 0.012° longitude intervals, equivalent to ~900 m on the ground and approximates a 3x3 Sentinel-3A OLCI pixel window as explained in Section 2.2.3. For this research, each day corresponded to 49 stations (except for station 29 on August 18, 2016, which was filtered out), amounting to 734 stations collected by SAS-ST for all 15 days.

3.2.2.2 FerryBox data: optical constituents

Biogeochemical data derived from the BC FerryBox, an automated system that measures various oceanographic environmental parameters such as chlorophyll-a concentration (ug/L), turbidity (NTU), CDOM fluorescence (ppb) and salinity (PSU), facilitated the understanding and categorization of diverse coccolithophore bloom spectra measured concurrently by the SAS-ST. Salinity (PSU) was measured via a SeaBird SBE45 thermosalinograph, the concentration of chlorophyl-a (Chla, ug/l) was measured through a WET Labs ECO Triplet fluorometer, and the fluorescence of CDOM (ppb) and turbidity (NTU) were measured by employing a WET Labs

ECO Triplet BBFL2 scattering fluorescence sensor. Detailed data processing procedures, including biofouling correction for the sensors and quenching correction for Chla measurements are presented in Travers-Smith et al. (2021).

3.2.2.3 Sentinel-3A OLCI reflectance

Level 1 Sentinel-3A OLCI images (Donlon et al., 2012) for the Salish Sea area were processed with POLYMER v4.14 (Steinmetz et al, 2016), which has shown the best performance compared with official L2, C2RCC and C2RCCNN in the area of study as shown in Giannini et al. (2021). The primary objective of the POLYMER algorithm is to segregate the atmosphere and residual sun glint signal from those scattered by the seawater (Steinmetz et al, 2016). This processor employs a three-parameter polynomial configuration to model atmospheric contribution and residual sun glint, and models oceanic reflectance with two variable parameters: the chlorophyll concentration, Chl (mg/m^3), and a scaling coefficient, f_b, for particle backscattering (Park and Ruddick, 2005; Steinmetz et al, 2016). The water reflectance model applies to both Case 1 and Case 2 waters and considers BRDF effects (Park and Ruddick, 2005; Steinmetz et al, 2016). Ultimately, the algorithm employs a spectral matching technique to optimize the parameters of the models mentioned above using 7 OLCI bands ranging from 412 nm to 665 nm, facilitating the best spectral fit for the total reflectance measured by the sensor.

A total of 8 images with 389 corresponding SAS-ST station matchups were analyzed. Matchup data from the OLCI (denoted as Rrs^{OLCI} hereafter) were extracted from a 3x3 macro-pixel window centered on the SAS-ST *in situ* station location, with a temporal difference not exceeding 3 hours. Within the 3x3 window, spectra for 9 pixels were exported with SNAP 9.0.0

using the following procedure: First, pixels with bitmasks of 2 (indicating cloud) and 3 (indicating land and cloud) were filtered out, while bitmasks of 2048 (indicating out-of-bands) and 0 were kept for a further quality check, as suggested by Steinmetz et al. (2016). It is worth noting that no Case 2 flags are shown for our highly reflective coccolithophore water. Second, outlier pixels within the 3x3 macro-pixel were defined as those with Rrs at 560 nm more than 1.5 times the standard deviation (SD) from the median; these outliers were eliminated to avoid their adverse influence on the matchup statistical analysis (Bailey and Werdell, 2006; Cui et al., 2010).

Further, it was required that a minimum of five pixels within the 3x3 window remain unflagged and that their coefficient of variation (CV) at 560 nm falls below the threshold of 0.15 (Bailey and Werdell, 2006). Finally, median values of the 384 macro-pixels were further evaluated considering water mass mismatches indicated by dominant surface current direction derived from a local CODAR system (Giannini et al., 2021; Nasiha et al., 2022) for matchup analysis with *in situ* SAS-ST data. From this step, we eliminated 45 macro-pixels recognized as water mass mismatches, reducing the number of macro-pixels (or samples hereafter) to 339 for matchup analysis.

3.2.3 Data analysis

The following data analysis procedures were performed: (1) classifying the coccolithophore bloom Rrs^{SST} data into three groups concerning its evolutionary stages based on their spectra characteristic; (2) using Rrs^{SST} as input features to train supervised machine learning models, specifically random forest classifiers (RFC); (3) selecting the optimal model considering the evaluation of Rrs^{OLCI} data for the different bands against time and spatially corresponding Rrs^{SST}, which was then applied to Rrs^{OLCI} spectra.

3.2.3.1 Classification of coccolithophore bloom stages

The coccolithophore bloom classification relies on the spectral characteristics of the hyperspectral Rrs^{SST} and the corresponding $nRrs^{SST}$ normalized at 560 nm. This classification was based on the spectral features located in the 400-550 nm range and around 670 nm, along with the reflectance magnitude. Based on these features, three distinct bloom stages were identified: no bloom, growing coccolithophore bloom, and decaying coccolithophore bloom. Due to the lack of *in situ* water samples to enable cell identification, the absorption and R_{rs} features of coccolithophore from Neeley et al. (2015) and Neukermans and Fournier (2018) were used for classification of coccolithophore bloom development stages.

During the growing bloom stage, *E. huxleyi* cultures exhibit significant absorption, peaking within 400-470 nm and gradually decreasing towards 550 nm, alongside a moderate absorption around 670 nm (Neeley et al. 2015). This strong absorption by photosynthetic pigments potentially leads to a decline of reflectance in the corresponding wavelengths. Groom and Holligan (1987) and Cazzaniga et al. (2021) also noted a comparable phenomenon wherein the blue reflectance typically diminishes relative to the green at the onset of bloom due to an elevated pigment concentration or cell-to-coccoliths ratio. This observation is supported by the radiative transfer simulations of reflectance from *E. huxleyi* blooms conducted by Neukermans and Fournier (2018). These authors showed that during the initial bloom phase, the absorption originating from the coccolithophore affects the magnitude and shape of the R_{rs} by diminishing the reflectance in the blue wavelengths.

For the decaying bloom stage, Figure 8 by Neukermans and Fournier (2018) illustrates that the initial and final stage spectra of coccolithophore blooms, with varying initial cell densities, are characterized by the presence or absence of two absorption features around 470 nm and 670 nm, linked to pigments within the cell cores. Notably, when all coccoliths have been shed and no living cores remain at the final stage, these absorption features flatten, and the R_{rs} magnitude increases several-fold. The presence of the highly scattering detached coccoliths suspended in the water during the final stage of the bloom is linked to the stereotypical bright milky turquoise colour typically observed during coccolithophore blooms (Balch et al., 2005). Figure 9A and 9B from Neukermans and Fournier (2018) also demonstrate that nR_{rs} exhibit minimal spectral shape variability during the decaying bloom stage, particularly in the blue wavelengths.

In brief, the coccolithophore bloom initial stage, defined as the growing bloom phase, was characterized based on the shape of the reflectance, particularly with lower nR_{rs} values in the 400-550 nm range and moderately lower values around 670 nm. Additionally, the chlorophyll-a fluorescence signal around 680-685 nm in nR_{rs} is prominent in this phase due to the active photosynthetic pigments. For the following stage, defined as the decaying bloom phase (coccoliths shed and no living cores remain), the reflectance absorption features around the 470 nm flatten, and the magnitude increases several folds, along with minor spectral shape variability in nR_{rs}. Spectra when coccolithophore blooms are not occurring exhibit low and flat reflectance signals over the entire spectra – indicating clear water (Phillips and Costa, 2017; Giannini et al., 2021; Nasiha et al., 2022; Wang and Costa, 2022).

3.2.3.2 Evaluation of OLCI Sentinel-3A R_{rs}

To ensure the accuracy and reliability of remote sensing data and to facilitate a more robust understanding of coccolithophore bloom dynamics, R_{rs} retrieved from OLCI was evaluated against *in situ* SAS-ST matchup samples across three different coccolithophore bloom spectral groups. The following statistics were used: the root mean square error (RMSE), mean absolute relative difference (MAD, expressed in %), mean relative difference (MRD, expressed in %), being determined as (Concha et al., 2021):

$$RMSE = \sqrt{\frac{1}{N}\sum_{i=1}^{N}(Rrs_i^{OLCI} - Rrs_i^{SST})^2}$$

$$MAD = 100\frac{1}{N}\sum_{i=1}^{N}\frac{\left|Rrs_i^{OLCI} - Rrs_i^{SST}\right|}{Rrs_i^{SST}}$$

$$MRD = 100\frac{1}{N}\sum_{i=1}^{N}\frac{(Rrs_i^{OLCI} - Rrs_i^{SST})}{Rrs_i^{SST}}$$

where Rrs^{OLCI} is the Sentinel-3 OLCI derived $Rrs(\lambda)$, Rrs^{SST} is the SAS-ST measured *in situ* $Rrs(\lambda)$, and N is the number of matchup samples. The regression slope, intercept, and determination coefficient (r^2) values between Rrs^{OLCI} and Rrs^{SST} were calculated using simple linear least-squares regression techniques (Cazzaniga et al., 2021).

3.2.3.3 Machine learning algorithm development with Rrs^{SST} and application on Rrs^{OLCI}

Methodologies for identifying coccolithophore blooms from satellite observations are typically designed for Case 1 waters, in which inorganic particulates and dissolved organic matter are not dominant (Balch and Mitchell, 2023). Recognizing the existing methodological limitations for identifying coccolithophore blooms from satellite observations in Case 2 waters (e.g., Brown and Yoder, 1994; Gordon et al., 2001; Iglesias-Rodríguez et al., 2002; Balch et al., 2005; Moore et al., 2012), the following work scheme was adopted to develop a novel machine learning approach that utilizes computational intelligence to implicitly handle the complex relationships among optical water constituents in Case 2 waters (Hu et al., 2021). Here, we present the steps (Figure 14) for developing a (i) random forest model using 10 bands of OLCI (RFC10, 400-709 nm) and (ii) an adapted RFC using 7 bands of OLCI (RFC7, 490-709 nm). The adapted model was developed due to the observed relatively poor performance of Rrs^{OLCI} retrievals at short blue wavelengths. The following steps were adopted:

Step 1 Data organization: The hyperspectral Rrs^{SST} data were labeled as one of the three groups (no bloom, growing bloom and decaying bloom) following the method detailed in Section 2.3.1. Among the 734 Rrs^{SST} samples, 374 were labeled as no bloom, 193 as growing bloom and 167 as decaying bloom. Following this, each spectrum was convoluted to the corresponding Sentinel-3A OLCI 10 bands from 400 to 709 nm using the Sentinel-3A OLCI Spectral Response Functions (SRFs) available from the European Space Agency (2021). Since the classification of coccolithophore blooms relies on the spectral characteristics of the hyperspectral Rrs^{SST} and the corresponding $nRrs^{SST}$ normalized at 560 nm (Neeley et al., 2015; Neukermans and Fournier, 2018), both the classified convoluted Rrs^{SST} at 10 wavelengths and the corresponding $nRrs^{SST}$ normalized at 560 nm at the same OLCI 10 wavelengths are employed as predictor variables (20 in total) for a supervised machine learning classifier to predict the target variable, which has three categorical levels: no bloom, growing bloom, and decaying bloom. Ratios between different wavelengths, which could capture important relationships between spectral bands, were tested as additional predictor variables during the machine learning model training. However, since they did not enhance the model's performance (results not shown here), band ratios were not included in this research. Owing to the incorporation of Rrs^{SST} and $nRrs^{SST}$ from 10 wavelengths in the RFC model, we refer to this model as RFC10 hereafter.

Step 2 RFC10 machine learning model development: Among different machine learning algorithms, the random forest classifier (RFC) was selected for this research due to its superior classification accuracy (Breiman, 2001), exceptional tolerance towards outliers and noise, resilience against overfitting (Tyralis et al., 2019) and its ability to provide a ranking of the predictor variable importance (Cutler et al., 2007). The RFC operates as an integrated algorithm grounded in the assembly of decision trees (Breiman, 2001). Combining the corresponding classification decision result from each decision tree, the RFC achieves the outcome through a voting process, in which the single category prediction with the highest votes is deemed the final result. This process enhances the overall model's precision and capacity to generalize, thereby elevating its predictive performance (Breiman, 2001).

The structure of a RFC requires specifying key hyperparameters, such as the number of trees (n_estimators) and the maximum depth of each decision tree (max_depth). A training dataset, randomly selected from the total sample set (N=734), consisting of 513 samples (70% of the total: 255 no bloom, 138 growing bloom, and 120 decaying bloom), was used to train the

RFC. The remaining 221 samples (30% of the total: 119 no bloom, 55 growing bloom, and 47 decaying bloom), designated as unseen data for the RFC trained on the training dataset including 513 samples, were used as a test dataset to provide a final unbiased evaluation of the model's performance.

During the training process, five-fold cross-validation was applied to ensure near-optimal model performance by iterating over different hyperparameter combinations (using GridSearchCV from the Python-based sklearn library) and obtaining the corresponding model's accuracy and standard deviation at certain hyperparameters combinations. A five-fold cross-validation operates by dividing the training dataset into five equally sized "folds" or subsets. The model is then trained and tested five times, each time designating a different fold (1/5 of the training dataset) as the test set while using the remaining four folds (4/5 of the training dataset) as the training set; this process repeats across all five folds. For each combination, the model's performance was evaluated by calculating the mean accuracy, which is the proportion of correctly classified instances in each fold and averaged to obtain a more reliable overall accuracy and the standard deviation (std) of the accuracy across the five folds. The Python code for this machine learning algorithm can be find in Appendix B. The hyperparameter max_depth=8 and n_estimators=100 were defined for RFC10, which resulted in an optimal accuracy of 0.967±0.0131 (mean ± standard variation).

Step 3 Optimization of the RFC10 model-RFC7: Due to the poor performance of the Rrs^{OLCI} compared with Rrs^{SST} at 400-443 nm range (Section 3.3), a modified machine learning model (RFC7) was developed to address this limitation. This modification involved selecting only seven specific wavelengths from *Rrs^{SST}* as input variables for the model, excluding the wavelengths within the 400-443 nm range due to their demonstrated poor performance in SAS-ST's OLCI matchup samples. The modified RFC7 model was trained using the same methodological framework as described earlier, with these seven wavelengths to train the classifier and evaluate its performance. RFC7 resulted in an accuracy of 0.967±0.0145 with the hyperparameters setting max_depth = 12 and n_estimators = 100.

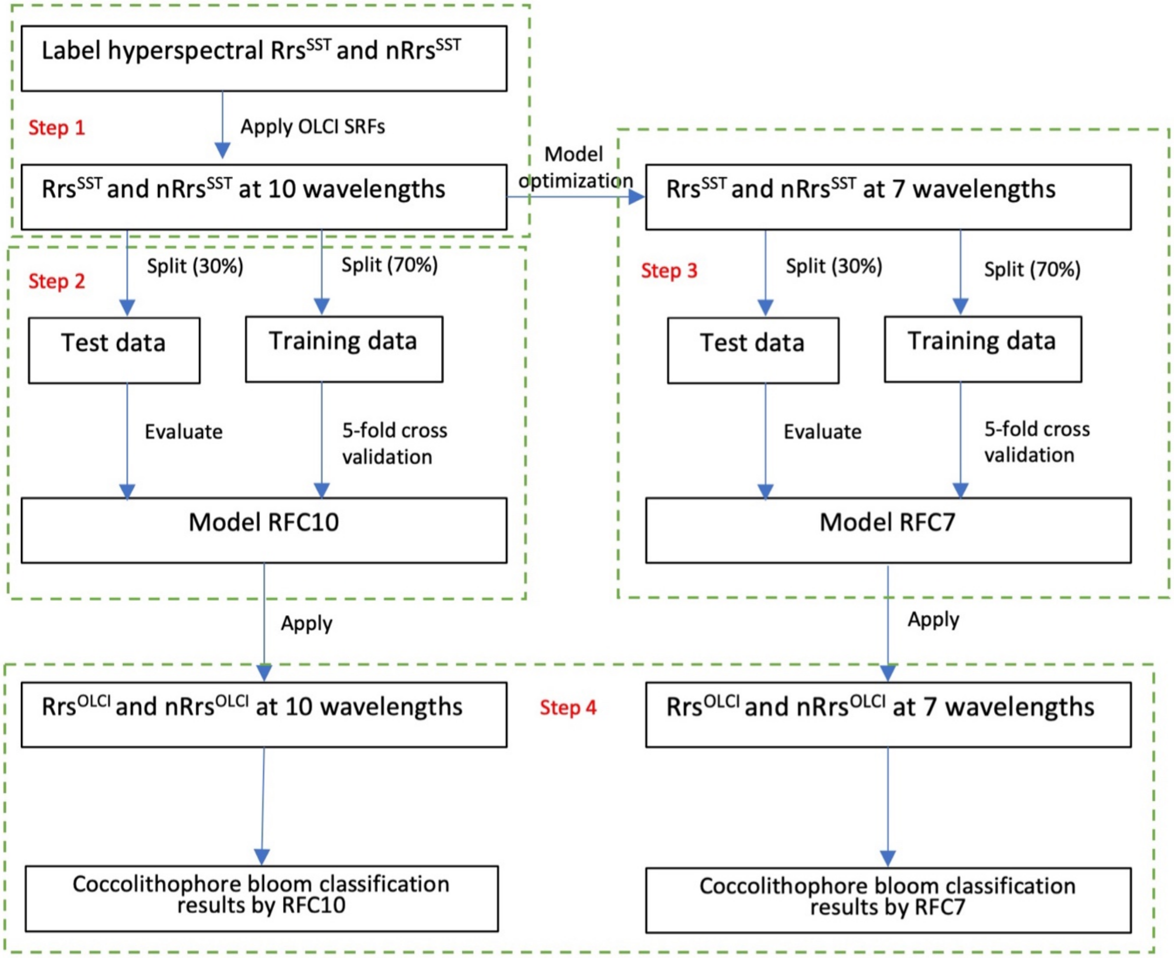

Figure 14| Flow chart showing the development of the random forest classifier using *in situ* *Rrs^{SST}* data and its application to satellite data *Rrs^{OLCI}* for coccolithophore bloom classification.

Step 4 RFC10 and RFC7 application on OLCI data: The final step was the evaluation of both models' accuracy in classifying OLCI retrieved spectra into non-bloom, growing bloom, and decaying bloom categories. For this, we used 339 OLCI retrieved Rrs^{OLCI} spectra as samples (no bloom 211, growing bloom 33, and decaying bloom 95). A confusion matrix, which summarizes the actual versus predicted classifications (Rosenfield and Fitzpatrick-Lins, 1984), was used to evaluate the classification accuracy, along with various derived evaluation metrics: precision and recall, frequently referred to as user's accuracy (UA), producer's accuracy (PA), and the Kappa coefficient (KC) and overall accuracy (OA) (Congalton, 1991). The four metrics' definitions are listed below:

- UA: the ratio of the total number of correct classifications for a particular category to the total number of samples predicted as that category.
- PA: the ratio of the total number of correct classifications for a particular category to the actual total number of samples referenced in that category.
- OA: the ratio of the total number of correctly classified samples to the total number of test samples.
- KC: quantifies the degree of agreement by considering the correctly classified samples potentially attributable to random occurrence. KC spans from -1 to 1, where a positive value indicates more agreement than would be anticipated by chance, with the agreement becoming stronger as the value approaches 1.

3.3 Results

3.3.1 Optical constituents: FerryBox data

Figure 15 illustrates the continuous spatial and temporal distribution of chlorophyll concentration (ug/L), turbidity (NTU), CDOM fluorescence (ppb) and salinity (PSU) obtained by the FerryBox system installed on QoOB. The route from Nanaimo to West Vancouver is designated as stations 1 through 49, with their specific locations depicted in Figure 13. Measurements were made from August 11, 2016 (denoted as 0811) to August 30, 2016 (denoted as 0830) as presented in Figure 15.

The concentrations of the optical constituents were highly variable both spatially and temporally. The salinity heatmap indicates a predominantly downward trend in salinity values from west to east along the route, decreasing from approximately 27 PSU on the Nanaimo side to 15-25 PSU on the West Vancouver side, except for a nearly stable measurement at ~ 28 PSU on 0818 (note that August 18, 2016 is denoted as 0818; Figure 15A). Additionally, the general temporal trends in surface water Chla concentration, turbidity, and CDOM fluorescence followed similar patterns during the study period. The FerryBox chlorophyll heatmap illustrates that the period from 0816 to 0820 generally exhibits higher Chla fluorescence signals (Figure 15B). Notably, some stations (e.g., stations 19-23) recorded Chla values exceeding 9 ug/L for most of that period, while stations 25-49 on 0818 show a Chla peak value (18 ug/L). Those high values reflect the accelerated proliferation of coccolithophore cores, subsequently leading to elevated pigment concentrations.

The turbidity heatmap displays heightened turbidity levels from 0815 to 0823, during which certain stations recorded turbidity values exceeding 5 NTU (Figure 15C). Moreover, for stations 21-25 in 0820 and 0822, turbidity exceeded 6 NTU, reaching a peak of 6.5 NTU at station 25 in 0820. Note that, spatially, the stations with high turbidity are not associated with Fraser River plume waters, thus indicating an association with coccolithophore blooms. The elevated turbidity period generally mirrors the higher chlorophyll levels observed during a similar timeframe. Regarding the peak days of Chla and turbidity measurements, there is a two-day shift, with Chla peaking two days earlier than turbidity. Observations of CDOM fluorescence display a trend analogous to that of Chla and turbidity measurements, starting with lower values in the initial days (<2 ppb), followed by an increase from 0817 to 0823, especially at the middle stations of the route, reaching a peak value of 3.1 ppb, before diminishing to lower levels once again (Figure 15D).

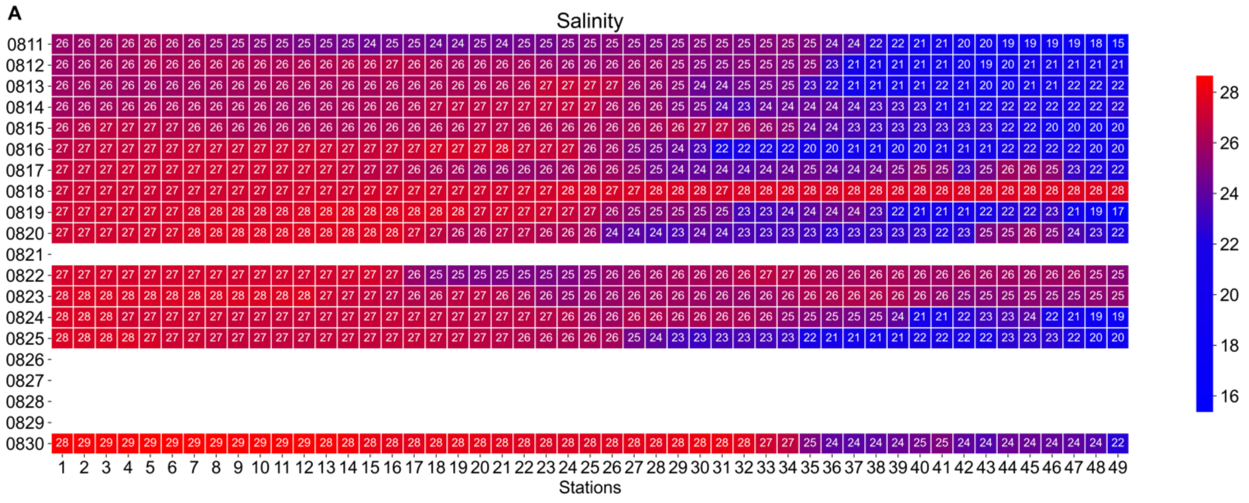

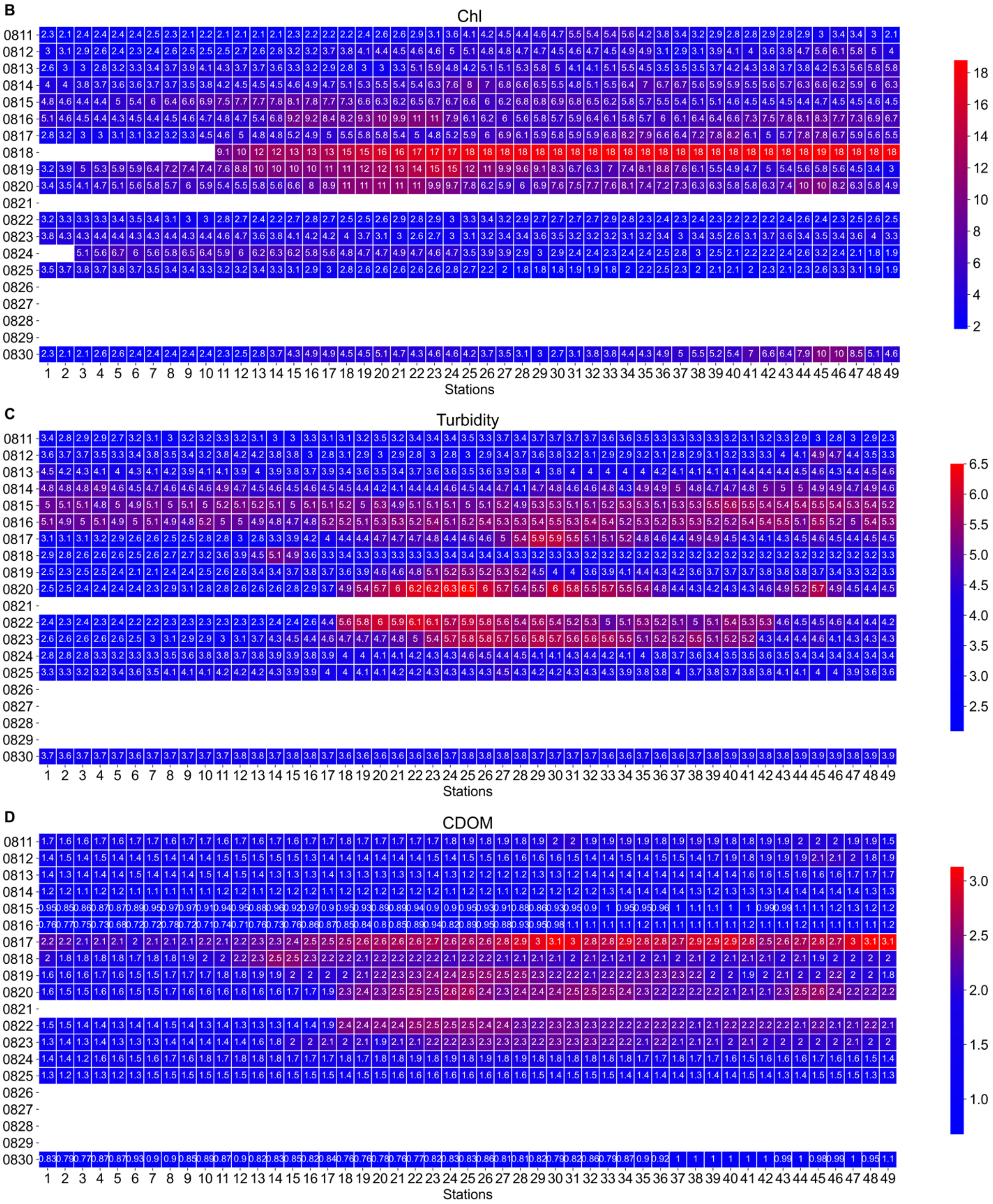
B
Chl
0811
0812
0813
0814
0815
0816
0817
0818
0819
0820
0821
0822
0823
0824
0825
0826
0827
0828
0829
0830
1 2 3 4 5 6 7 8 9 10 11 12 13 14 15 16 17 18 19 20 21 22 23 24 25 26 27 28 29 30 31 32 33 34 35 36 37 38 39 40 41 42 43 44 45 46 47 48 49
Stations
18
16
14
12
10
8
6
4
2
C
Turbidity
1 2 3 4 5 6 7 8 9 10 11 12 13 14 15 16 17 18 19 20 21 22 23 24 25 26 27 28 29 30 31 32 33 34 35 36 37 38 39 40 41 42 43 44 45 46 47 48 49
Stations
6.5
6.0
5.5
5.0
4.5
4.0
3.5
3.0
2.5
D
CDOM
1 2 3 4 5 6 7 8 9 10 11 12 13 14 15 16 17 18 19 20 21 22 23 24 25 26 27 28 29 30 31 32 33 34 35 36 37 38 39 40 41 42 43 44 45 46 47 48 49
Stations
3.0
2.5
2.0
1.5
1.0

Figure 15| FerryBox heatmap of (A) salinity (PSU), (B) Chlorophyll-a fluorescence (ug/L) values, (C) turbidity (NTU), and (D) CDOM fluorescence (ppb). The X axis represents stations ranging from 1 to 49, corresponding to samples acquired along the ferry route from Nanaimo to West Vancouver, as shown in Figure 13. The Y axis indicates the date and the measured values of the variable over consecutive days during the coccolithophore bloom period from August 11 (0811) to August 30 (0830), 2016. Blue and red refer to the lowest and highest values, respectively.

3.3.2 Classification of coccolithophore bloom development stages

According to the spectral analysis method described in Section 3.2.3.1 for reflectance (Rrs^{SST}) and normalized reflectance ($nRrs^{SST}$), the results showed that the 734 samples were partitioned into three classes, no bloom (n=374), growing bloom (n=193), and decaying bloom (n=167). Figure 16 shows the coccolithophore spectra classification through a time series *of* Rrs^{SST} and $nRrs^{SST}$ data from 0811 to 0830 captured at station 19 (Figure 13), which is approximately at the middle of the ferry route and has representative high concentrations of optical constituents as indicated in Figure 15. Note that during the no bloom phase (0811-0815 and 0830), Rrs^{SST} exhibited relatively uniform and low values across the wavelengths, with the peak values fluctuating around 0.006 sr^{-1}, except for the data collected on 0811. The corresponding $nRrs^{SST}$ exhibited the smoothest spectra among the three phases, lacking the concavity around 470 nm typically associated with phytoplankton pigment absorption. This uniformity in both Rrs^{SST} and $nRrs^{SST}$ supports the classification of this period as the no bloom phase, characterized by the reflectance signal indicative of clear water with low particulate matter.

The growing bloom class (0816-0820) exhibited higher *Rrs*^{SST} values (0.008-0.028 sr^{-1}) and a more irregular *nRrs*^{SST} shape, reflecting an increased concentration of coccolithophores. A decline of reflectance in the 400-550 nm is clearly evident in the *nRrs*^{SST} curves, likely associated with the strong absorption by photosynthetic pigments (Figure 16B). Specifically, *nRrs*^{SST}(470) decreased from above 0.60 (0811 to 0815 and 0822 to 0830) to about 0.44-0.56 (0816 to 0820). The secondary *nRrs*^{SST} pigment absorption concave around 670 nm is also representative of growing bloom days (Figure 16C). Further, the Chla fluorescence signal around 680-685 nm on those days showed evident peaks (Figure 16C). It is also evident that *Rrs*^{SST} (560) during those days generally continued to increase from below 0.008 sr^{-1} before 0816 (except 0811) to nearly 0.03 sr^{-1}. This increase corresponds to the growing bloom stage, as indicated by the spectral fingerprints, which reflect rising cell densities and the associated optical changes characteristic of an actively developing coccolithophore population.

During the decaying bloom phase (0822 - 0825), the two pronounced lower *nRrs*^{SST} signals around 470 nm and 670 nm disappeared, with *nRrs*^{SST}*(470)* rising to a narrow range of 0.64-0.70 and the *nRrs*^{SST} clearly show small spectral shape variability (Figure 16B). Additionally, the absence of significant peaks around the Chla fluorescence at 680-685 nm (Figure 16C) further indicates the decrease of active phytoplanktonic pigments. *Rrs*^{SST}*(560)* increased from 0.028 sr^{-1} on day 0820 to 0.043 sr^{-1} on day 0822, followed by a significant continuous reduction in *Rrs*^{SST} magnitude until day 0825 (*Rrs*^{SST}*(560)* =0.023 sr^{-1}) (Figure 16A).

These spectral patterns indicate the decaying phase of the bloom, characterized by decreased pigment absorption, fluorescence, and scattering, indicating a reduction in the coccolithophore population.

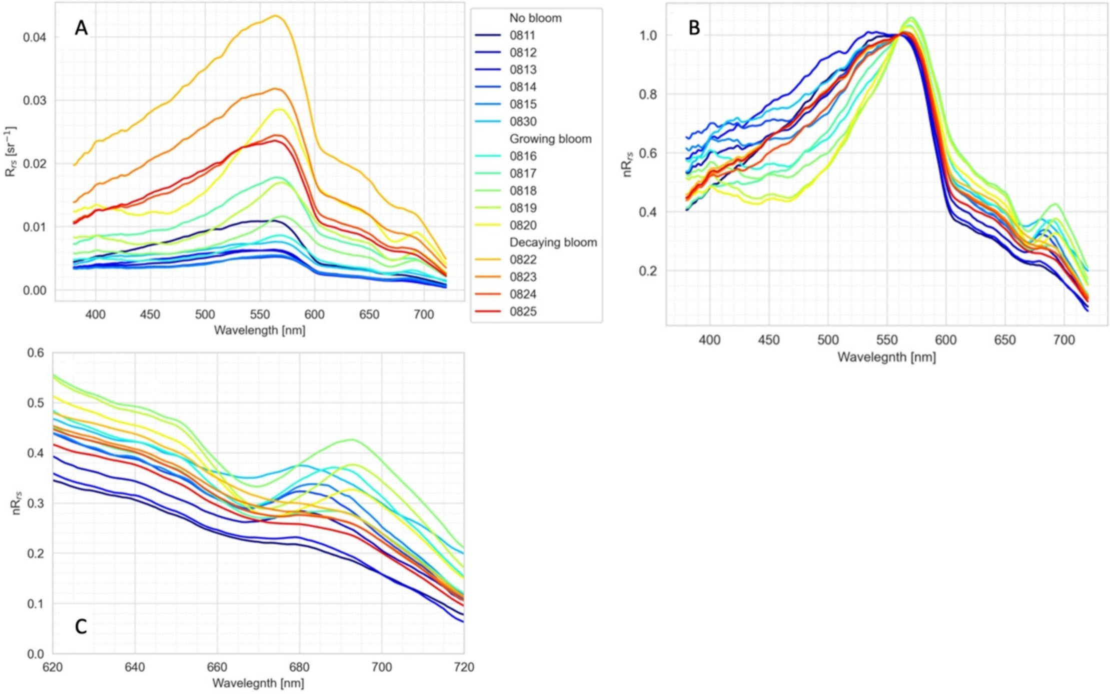

Figure 16| Station 19 time series spectra evolution of (A) Rrs^{SST}, (B) $nRrs^{SST}$ and (C) a zoomed-in view of $nRrs^{SST}$ around 670 nm. The Rrs^{SST} from 15 days are divided into three groups: no bloom (0811-0815 and 0830), growing bloom (0816-0820) and decaying bloom (0822-0825) according to their spectra features and accompanying FerryBox data.

Figure 17 summarizes the spatial and temporal domains of coccolithophore bloom development stages based on their spectral characteristic of Rrs^{SST} , as illustrated above. The figure indicates that the bloom begins in the eastern part of the ferry route (West Vancouver side) and propagates westward (towards the Nanaimo side), with the growing bloom phase starting on 0815. This timing is consistent with the findings of Wang and Costa (2022), rather than 0816 as indicated in Figure 16, which was based solely on the analysis of station 19 instead of all stations.

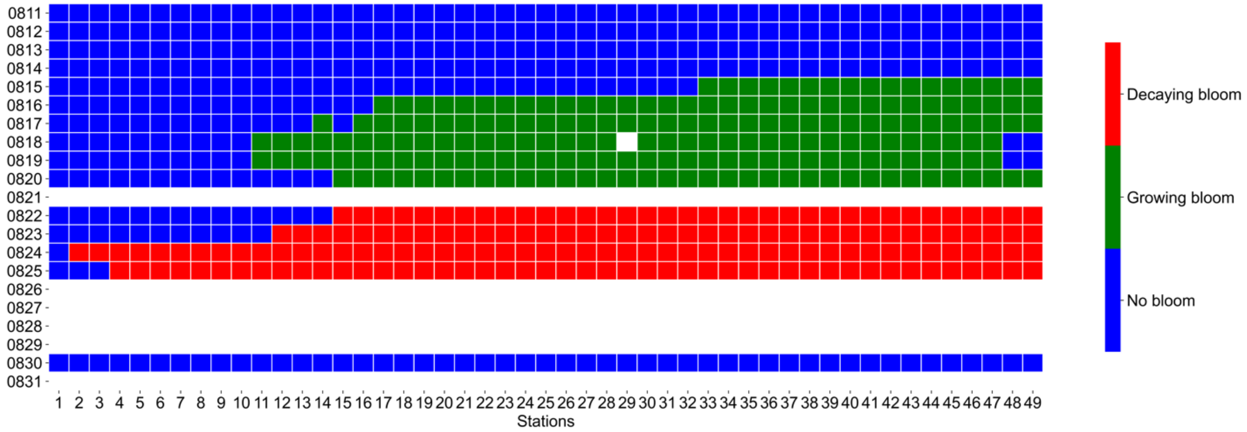

Figure 17| Heatmap of the classification of coccolithophore bloom development stages based on *Rrs*^{SST}. The X axis represents stations ranging from 1 to 49, corresponding to samples acquired along the ferry route from Nanaimo to West Vancouver, as shown in Figure 13. The Y axis indicates the date and the coccolithophore bloom development stages over consecutive days during the coccolithophore bloom period from August 11 (0811) to August 30 (0830), 2016.

3.3.3 Evaluation of *Rrs*^{OLCI} based on *Rrs*^{SST}

The matchup analysis generally showed that *Rrs*^{OLCI} is slightly underestimated, especially in the shorter wavelengths compared with *Rrs*^{SST}. Figure 18 shows that, for the three groups of spectra acquired at different evolutionary stages of the coccolithophore bloom, *Rrs*^{OLCI} is slightly underestimated compared with *Rrs*^{SST}, especially in the shorter blue wavelengths. This underestimation is reflected in negative MRD values across all wavelengths (Figure 19 and

Table 4). Specifically, at 400, 412, and 443 nm, the high negative MRD (<-25.9%) for all three groups indicates a notable underestimation of Rrs^{OLCI} compared with the corresponding Rrs^{SST}. Notably, the Rrs^{OLCI} for decaying bloom group performs the worst, with the MRD dropping below -30.0%.

However, a pronounced enhancement in performance for all groups is observed between 490 and 681 nm, with the absolute minimum MRD lying between -9.4% and -4.3% at 560 nm. For 709 nm, the discrepancy is markedly pronounced for the non-bloom compared to the two bloom groups as shown by the MRD and MAD values. This is because the Rrs^{OLCI} signal is notably reduced in the absence of coccolithophores, and the usages of a relative measure of difference, such as MRD and MAD, rather than absolute ones, like RMSE, may yield unrealistic values when *Rrs* approaches zero. The RMSE values for all three groups at 709 nm fall within a similarly low range of 0.005 to 0.008 sr^{-1}, suggesting that this wavelength exhibits satisfactory matchup performance.

Given the poor performance of the Rrs^{OLCI} at shorter 400-443 nm wavelength range, an alternative RFC model optimization method was developed. Instead of using all 10 OLCI wavelengths for training a coccolithophore bloom classification model (RFC10), a separate model was trained using the remaining seven bands after excluding the 400, 412, and 443 nm bands (RFC7).

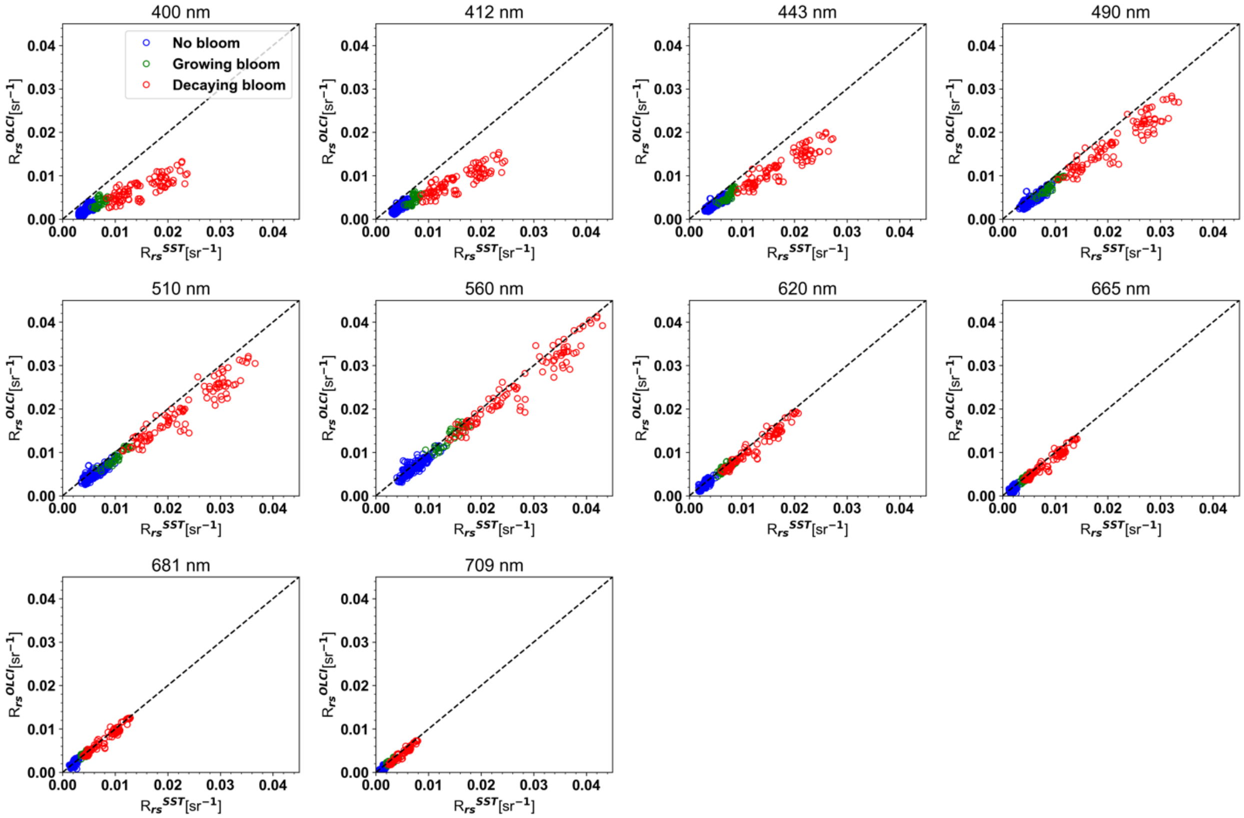

Figure 18| The reflectance matchups between Sentinel-3A OLCI and SAS-ST for 339 samples across 10 wavelengths. The dotted lines represent the one-to-one relationship between Rrs^{SST} and Rrs^{OLCI}.

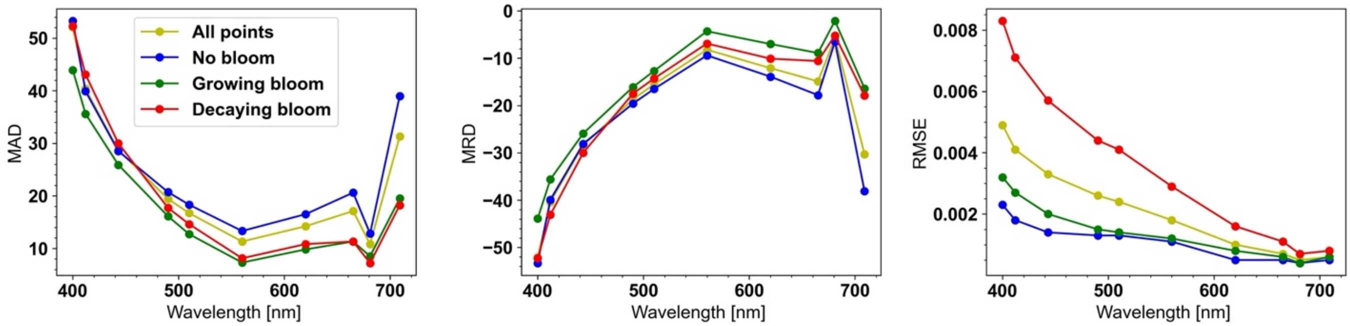

Figure 19| Statistics including the mean absolute relative difference (MAD, expressed in %), mean relative difference (MRD, expressed in %), and root mean square error (RMSE) for all 339 samples and three groups (no bloom, growing, and decaying coccolithophore bloom group).

Table 4| Statistics including the regression slope, intercept, and determination coefficient (r^2) values calculated using simple linear least-squares regression techniques, the mean absolute relative difference (MAD, expressed in %), mean relative difference (MRD, expressed in %), and root mean square error (RMSE) for all 339 samples and three groups (no bloom, growing, and decaying coccolithophore bloom group).

	Wavelengths	Slope	Intercept	r^2	MAD	MRD	RMSE
	400	0.48	0.0001	0.87	52.1	-52.1	0.0049
	412	0.55	0.0003	0.92	40.4	-40.4	0.0041
	443	0.69	0.0002	0.96	28.7	-28.4	0.0033

All samples	490	0.82	-0.0001	0.97	19.4	-18.7	0.0026
	510	0.86	-0.0001	0.97	16.7	-15.5	0.0024
	560	0.94	-0.0002	0.98	11.3	-8.2	0.0018
	620	0.92	-0.0001	0.98	14.2	-12.1	0.0010
	665	0.92	-0.0002	0.98	17.1	-14.9	0.0007
	681	0.96	0.0000	0.98	10.8	-5.7	0.0005
	709	0.93	-0.0004	0.96	31.3	-30.3	0.0006
No bloom	400	0.77	-0.0013	0.55	53.3	-53.3	0.0023
	412	0.79	-0.0008	0.64	39.9	-39.9	0.0018
	443	0.79	-0.0003	0.76	28.5	-28.1	0.0014
	490	0.80	0.0000	0.81	20.7	-19.6	0.0013
	510	0.79	0.0002	0.8	18.3	-16.5	0.0013
	560	0.85	0.0004	0.78	13.3	-9.4	0.0011
	620	0.97	-0.0003	0.7	16.5	-13.9	0.0005
	665	0.95	-0.0002	0.51	20.6	-17.8	0.0005
	681	1.01	-0.0002	0.54	12.8	-6.5	0.0004

	709	0.86	-0.0003	0.36	39	-38.1	0.0005
Growing bloom	400	0.60	-0.0003	0.26	43.9	-43.9	0.0032
	412	0.82	-0.0013	0.38	35.6	-35.6	0.0027
	443	1.13	-0.0028	0.75	25.9	-25.9	0.0020
	490	1.00	-0.0014	0.89	16.1	-16.1	0.0015
	510	0.97	-0.001	0.89	12.7	-12.7	0.0014
	560	0.98	-0.0003	0.82	7.3	-4.3	0.0012
	620	0.86	0.0005	0.63	9.8	-7.0	0.0008
	665	0.83	0.0004	0.58	11.3	-8.9	0.0006
	681	0.84	0.0006	0.57	8.5	-2.1	0.0004
	709	0.69	0.0004	0.59	19.5	-16.4	0.0006
	400	0.46	0.0002	0.66	52.3	-52.3	0.0083
	412	0.55	0.0003	0.76	43.1	-43.1	0.0071
	443	0.68	0.0003	0.85	30.0	-30.0	0.0057
	490	0.8	0.0004	0.89	17.7	-17.5	0.0044

Decaying bloom	510	0.84	0.0005	0.90	14.6	-14.3	0.0041
	560	0.93	0.000	0.93	8.1	-6.9	0.0029
	620	0.92	-0.0003	0.95	10.8	-10.1	0.0016
	665	0.93	-0.0002	0.95	11.3	-10.6	0.0011
	681	0.96	-0.0001	0.95	7.2	-5.2	0.0007
	709	0.99	-0.0007	0.96	18.2	-17.9	0.0008

3.3.4 Rrs^{SST} random forest classifier – RFC10 and RFC7

Figure 20 shows the results of the Rrs^{SST} random forest classifier RFC10 for the coccolithophore bloom classification. Specifically, Figure 20A shows that based on permutation-based feature importance, the 20 predictor variables (Rrs^{SST} and $nRrs^{SST}$) are crucial for identifying the presence of coccolithophore blooms and discerning their various development stages. Notably, *nRrs(510)* and *nRrs(490)*, mainly influenced by the absorption of coccolithophore pigments from 400-550 nm, are the first and fourth most important features of the RFC10. Furthermore, *Rrs(681)*, the second most important feature, is mainly influenced by chlorophyll-a fluorescence, which peaks within the 680-685 nm range.

Figure 20B shows the relationship for the top two predictor features, *nRrs(510)* and *Rrs(681)*, partitioned according to their corresponding bloom groups. The observed high dispersion highlights the potential of these two predictor features to effectively differentiate between the groups, suggesting their importance in coccolithophore bloom classification analysis. It is noticeable that the three groups are well grouped, except for minor overlaps in the boundaries between groups, especially for the growing and decaying bloom groups. No overlap is observed between the no bloom and decaying bloom groups. Specifically, the no bloom group is better separated from the other two groups than the separation between growing bloom and decaying bloom, and the prediction errors generally increase with the increasing overlap area between the two groups. For instance, only six erroneous prediction samples among the test samples (N=221) were observed, corresponding to a prediction accuracy of 97.3% (Table 2). From the erroneous prediction, four out of six samples were error predictions between growing and decaying bloom groups, which happens at the two groups' overlap area (Figure 20B,C). Only one sample is an error prediction between no bloom and decaying bloom, and one sample is an error prediction between no bloom and growing bloom, and both happen in the two groups' overlap area as well.

By comparing the permutation-based feature importance between RFC10 and RFC7 (Figure 20A, Figure 21A), a noticeable reordering of predictor variables is observed. Permutation importance measures the change in a model's performance, such as accuracy in this case, when the values of a specific feature are randomly shuffled while keeping all other features unchanged. The concept is that if a feature is important for predictions, scrambling its values will significantly reduce the model's performance. In contrast, if a feature is less important, shuffling it will have minimal or no impact (Cutler et al., 2007). Here, the most important predictor features in RFC10 remain important in RFC7. Specifically, the top two features in RFC10, *nRrs(510)* and *Rrs(681)*, decreased to third and sixth in importance in RFC7. Conversely, the fourth and sixth features in RFC10, *nRrs(490)* and *Rrs(620)* , rose to become the top two important predictor features in RFC7. *nRrs (490)* replaced *nRrs(510)* likely because both bands are primarily influenced by the absorption of coccolithophore pigments in the 400-550 nm range. Figure 21B presents the scatterplot of RFC7 for the top two crucial predictor features, *nRrs(490)* and *Rrs(620)*, partitioned by their respective bloom. This distribution closely resembles the scatterplot of the top two predictor features in RFC10 (Figure 20B), and similarly, prediction errors tend to increase in the regions where groups overlap. Specifically, seven erroneous predictions were observed within the test samples (N=221), resulting in a prediction accuracy of 96.8% (Table 3). Of the errors, four out of seven were misclassifications between the growing and decaying bloom groups, occurring in the overlap area of these two groups (Figure 21C). Additionally, one error occurred between no bloom and growing bloom, and two between no bloom and decaying bloom, both also in areas of group overlap (Figure 21C).

It is notable that both RFC10 and RFC7 demonstrate similarly strong performance in detecting coccolithophore bloom development stages using reflectance data measured by the ground-truth SAS-ST. However, when applying RFC10 to broader applications, such as Sentinel-3A OLCI, larger classification errors arise, particularly for the decaying bloom group, due to the poor performance of OLCI measurements in the 400-443 nm range, as discussed in Section 3.3. In contrast, applying RFC7 to OLCI improves classification accuracy by discarding the erroneous bands in the 400-443 nm range.

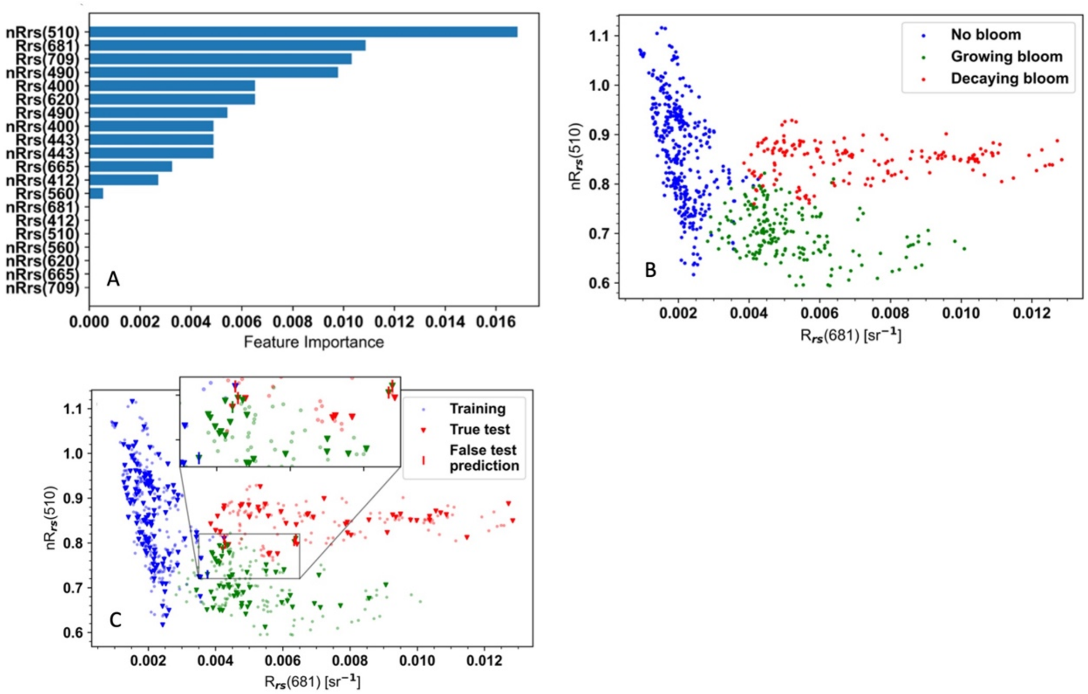

Figure 20| (A) Feature importance of 20 predictor variables used in random forest classifier RFC10. (B) Scatter plot of the two most important predictor variables, *nRrs(510)* and *Rrs(681)*, for all (n=734) SAS-ST samples colour-coded according to the three groups; *Rrs(681)* and *nRrs(510)* were chosen as x and y is because these two best separate the three classes. (C) Scatter plot of *nRrs(510)* and *Rrs(681)* for 70% of the SAS-ST samples as the training dataset for RFC10 (semi-transparent coloured dots) and the remaining 30% as the test dataset (solid coloured triangle). The vertical line indicates the six erroneous prediction samples, with the line colour indicating their false bloom groups and the triangular background colour indicating the true groups.

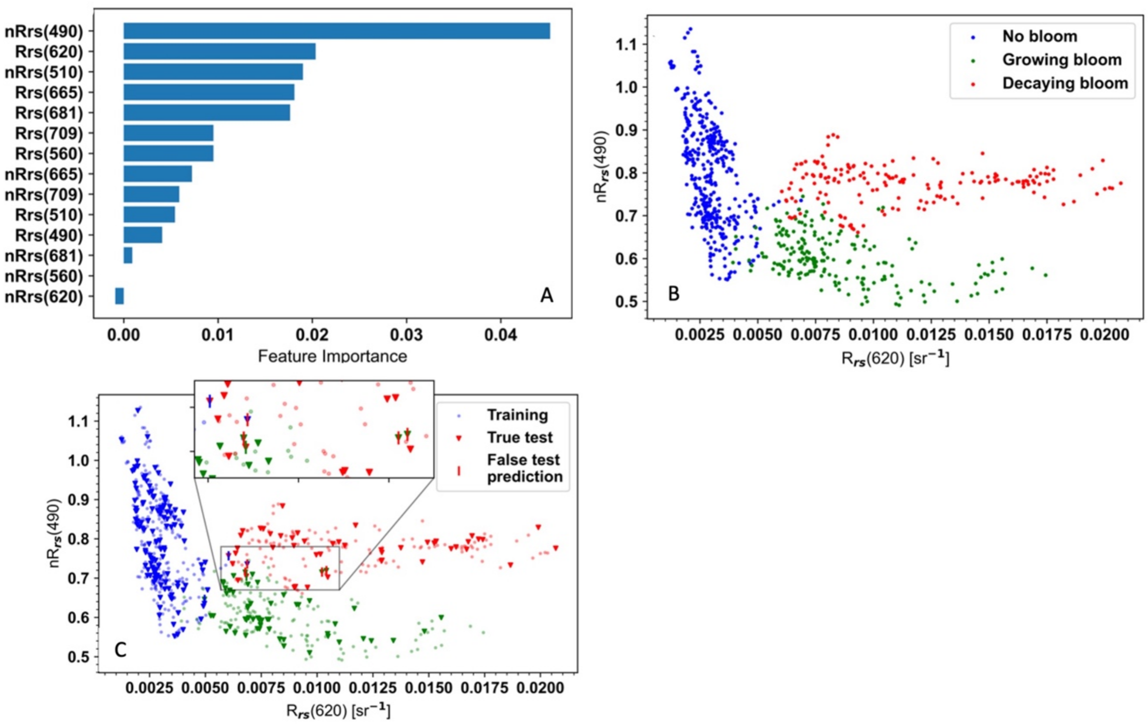

Figure 21| (A) Feature importance of 14 predictor variables used in random forest classifier RFC7. (B) Scatter plot of the two most important predictor variables, *nRrs(490) and Rrs(620)*, for all (n=734) SAS-ST samples colour-coded according to the three groups; *Rrs(620)* and *nRrs(490)* were chosen as x and y is because these two best separate the three classes. (C) Scatter plot of *nRrs(490)* and *Rrs(620)* for 70% of the SAS-ST samples as the training dataset for RFC7 (semi-transparent coloured dots) and the remaining 30% as the test dataset (solid coloured triangle). The vertical line indicates the seven erroneous prediction samples, with the line colour indicating their false bloom groups and the triangular background colour indicating the true groups.

Table 5| Confusion matrix of RFC10 for SAS-ST testing samples (N=221).

	True no bloom	True growing bloom	True decaying bloom
Predict no bloom	118	1	0
Predict growing bloom	0	51	1
Predict decaying bloom	1	3	46
Total	119	55	47
Overall accuracy	97.3%		

Table 6| Confusion matrix of RFC7 for SAS-ST testing samples (N=221).

	True no bloom	True growing bloom	True decaying bloom
Predict no bloom	118	1	1
Predict growing bloom	0	51	1
Predict decaying bloom	1	3	45
Total	119	55	47
Overall accuracy	96.8%		

3.3.5 Coccolithophore bloom Rrs^{OLCI} spectra machine learning classification based on RFC10 and RFC7

Two sets of procedures are presented due to outcomes of the matchup analysis: (i) apply RFC10 on the corresponding Rrs^{OLCI} 10 bands (RFC10, 400-709 nm) and (ii) apply RFC7 on the corresponding Rrs^{OLCI} 7 bands, 490-709 nm).

RFC10 resulted in an overall accuracy of 79.4% (Table 7). Notably, the no bloom group exhibited the most accurate classification results, achieving a user accuracy of 97.7 % and a producer accuracy of 100%. As defined in Section 3.2.3.3, user accuracy (UA) is the ratio of the total number of correct classifications for a particular category to the total number of samples predicted as that category. For example, in the no bloom category, the model correctly identified 97.7% of the cases that were classified as no bloom. Producer accuracy (PA), on the other hand, is the ratio of the total number of correct classifications for a particular category to the actual total number of samples in that category. In the case of the no bloom group, PA was 100%, meaning all the no bloom samples were correctly identified as such. Conversely, the largest misclassification resulted in a producer accuracy from the decaying bloom of 29.5%. Table 7 also indicates that the user accuracy of the RFC10 model is 97.7% in distinguishing no bloom *Rrs* from growing and decaying blooms, and it achieves 100% in distinguishing decaying blooms from the other two categories. However, the accuracy decreases to 31.6% when distinguishing growing blooms from the other two categories.

Table 7| Confusion matrix of Rrs^{OLCI} using model RFC10 trained by Rrs^{SST} (N=339 samples).

	True no bloom	True growing bloom	True decaying bloom	Total	User's accuracy
Predict no bloom	211	3	2	216	97.7%
Predict growing bloom	0	30	65	95	31.6%
Predict decaying bloom	0	0	28	28	100%
Total	211	33	95		
Producer's accuracy	100%	90.9%	29.5%		
Overall accuracy	79.4%	Cohen's kappa	0.14		

Compared to the RFC10, The RFC7 model achieved an overall accuracy of 89.1% (Table 8). Additionally, the Kappa coefficient increased from 0.14 in RFC10 to 0.66 in RFC7, indicating that the adapted classifier has a substantially higher classification agreement than the original classifier, beyond what would be expected by random chance. Specifically, as shown in the confusion matrix of the prediction results (Table 8), RFC7's producer accuracy of the no bloom group and the growing bloom group is over 90.0%, similar to the values in RFC10. The decaying bloom group's producer accuracy increased from 29.5% (RFC10) to 65.3% (RFC7). Regarding user accuracy, the decaying bloom group also attained the highest value of 98.4%, trailed by the no bloom group at 96.8%, similar to the values in RFC10. The user accuracy for the growing bloom group also experienced a substantial enhancement, moving from 31.6% (RFC10) to 50.8% (RFC7).

The results of the confusion matrix are also presented in a spider plot (Figure 22). This effective graphical approach evaluates the behaviour of models across multiple evaluation metrics by providing a synoptic visualization of all considered metrics (Seegers et al., 2018; Giannini et al., 2021). Note that the accuracies in percentage format have been converted to decimal points to accommodate the integration of the Kappa coefficient in this figure. In the spider plot, the center signifies a value of 0, while the outermost circle represents a value of 1, indicating the best performance. Consequently, the largest polygon shape area defines the best overall model performance. As such, the adapted RFC7 demonstrated superior classification accuracy over its original counterpart, as it represents the largest area. Most of the differences are related to RFC7 improved performance for the Kappa coefficient and the producer's accuracy for the decaying bloom group.

Table 8| Confusion matrix of by *Rrs*^{OLCI} using model RFC7 trained by *Rrs*^{SST} (N=339 samples).

	True no bloom	True growing bloom	True decaying bloom	Total	User's accuracy
Predict no bloom	210	2	5	217	96.8%
Predict growing bloom	1	30	28	59	50.8%
Predict decaying bloom	0	1	62	63	98.4%
Total	211	33	95		
Producer's accuracy	99.5%	90.9%	65.3%		
Overall accuracy	89.1%	Cohen's kappa	0.66		

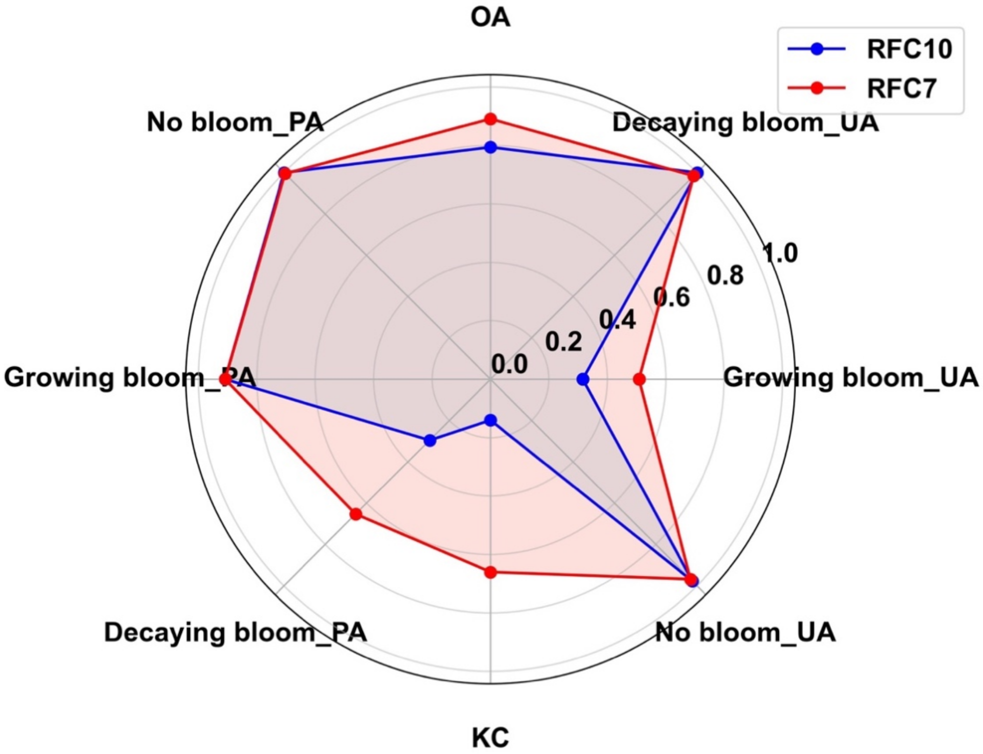

Figure 22| Producer accuracy (PA) and user accuracy (UA) are presented for the three bloom groups under RFC10 (blue) and RFC7 (red) coccolithophore classifier models. Additionally, the overall accuracy (OA) and Kappa coefficient (KC) for the whole dataset are incorporated.

3.4 Discussion

3.4.1 Evolution of the coccolithophore bloom

The FerryBox chlorophyll heatmap (Figure 15) reveals elevated Chlorophyll-a fluorescence readings between 0816 and 0820, indicating increasing phytoplankton biomass. These findings align closely with the $nR_{rs}^{SST}(470)$ concavity observed at the same timeframe

(Figure 16B). This spectral pattern is attributed to increased photosynthetic pigment absorption (Neeley, 2015), which from 0816 to 0820 is associated with the coccolithophore growing phase. Similarly, these days showed elevated CDOM values, likely a consequence of the decomposition of coccolithophore bloom cells during the growing and decaying phase rather than originating from Fraser River discharge. Previous studies in this region have suggested that the Fraser River is the main source of CDOM in this region; however, these studies did not include datasets acquired during coccolithophore bloom conditions (Johannessen et al., 2003; Phillips and Costa, 2017; Giannini et al., 2021). This is further confirmed by the observation that increased CDOM levels in our data are not associated with decreased salinity (Figure 15), which would typically indicate input from the Fraser River (Masson, 2006).

In the Strait of Georgia (SoG), total suspended matter (TSM) is associated both with the dynamics of the Fraser River (Loos and Costa, 2010; Phillips and Costa, 2017) and with spring and summer phytoplankton blooms (Masson and Peña, 2009; Halverson and Pawlowicz, 2016; Phillips and Costa, 2017; Giannini et al., 2021). During the growing phase and a significant part of the decay phases of the coccolithophore bloom observed in this research, the FerryBox turbidity measurements showed elevated turbidity values exceeding 5 NTU. Concurrently, the growing phase of the coccolithophore bloom exhibited Chla concentrations above 9.0 µg/L, as shown in Figure 15. Notably, Figure 15 also shows that higher turbidity is associated with higher salinity levels, suggesting that the TSM does not represent inorganic particles originating from riverine sediments. Given that Phillips and Costa (2017) observed that phytoplankton blooms in the SoG with Chla concentrations up to 7.0 µg/L were linked to elevated TSM levels, it is likely that the high TSM measured by the FerryBox in this research is also associated with the coccolithophore bloom. As Figure 15 shows, the turbidity peak day (6.5 NTU at station 25 on 0820) occurs two days later than the Chla peak (18.0 ug/L on 0818), which may be attributed to the shedding of coccolith shells after 0820.

In addition to the time series spectra plot for station 19 shown in Figure 16, the time series spectra plot for stations 19 to 23, shown in Figure 23, illustrates the shape and magnitude differences, and peak wavelengths shift of the spectra under different water conditions. It is noticeable that Rrs^{SST} for the non-bloom waters is relatively flat in shape and low in magnitude, with the majority peak wavelengths at 562-564 nm and Rrs^{SST} peak values below 0.01 sr^{-1}. For the growing bloom water, while Rrs^{SST} increased to moderate magnitude with peak wavelengths at 564-571 nm and Rrs^{SST} peak values varied around 0.017 sr^{-1}, $nRrs^{SST}(470)$ decreased to below 0.6, which is caused by the strong pigment absorption in this stage (Neeley et al., 2015). For the decaying bloom water, Rrs^{SST} increased to moderate to high magnitude with peak wavelengths at around 564 nm and Rrs^{SST} peak values above 0.023 sr^{-1}, and the absorption feature in $nRrs^{SST}(470)$ disappeared. Rrs^{SST} values were extremely high in the decaying bloom water, peaking on August 22, with $Rrs^{SST}(564)$ reaching 0.043 sr^{-1}. This significant increase contributed to the distinctive bright milky turquoise colouring typical of coccolithophore bloom (Gordon et al., 2001; Balch et al., 2005).

Figure 23C also shows that the peak wavelengths shift at different bloom development stages. Specifically, before the onset of coccolithophore bloom (0811-0815), the majority of the Rrs^{SST} peak was found around 564 nm. When the bloom starts on 0816, the Rrs^{SST} peak wavelength shifts to 570 nm at 0819, then the coccolithophores decay and the peak wavelength shifts back to 564 nm at 0822. Comparable blueward shifts in the *Rrs* maximum wavelength for the coccolithophore bloom decaying stage have been observed in studies by Neukermans and Fournier (2018). Neukermans and Fournier (2018) indicated that during the growing phase, the peak *Rrs* wavelength is situated within the green spectrum, specifically between 500-550 nm, which then transitions towards 400-490 nm wavelengths in the decaying bloom stage. This shift is attributed to the liberation of coccoliths and the absence of remaining cores to absorb light. A discernible disparity in *Rrs* maximum wavelength between the current study and the simulations conducted by Neukermans and Fournier (2018) is evident. Neukermans and Fournier (2018) indicated that the simulated spectra *Rrs* maximum wavelengths consistently range from 400 to 550 nm irrespective of the bloom stages. In contrast, we observed a peak *Rrs* signal within a narrower 562-571 nm range. This discrepancy in *Rrs* maximum wavelength range may be attributed to different waters' distinct background optical properties. Neukermans and Fournier (2018)'s work pertains to Case 1 waters characterized by low concentrations of CDOM and negligible particles backscattering as the background conditions, contrary to Case 2 water in this research. Additionally, Neukermans and Fournier (2018) further incorporated enhanced CDOM absorption into their Case 1 water simulations, highlighting a potential shift in peak wavelength from blue to green bands, similar to what we observed in our data. This simulation was corroborated by Cazzaniga et al. (2021) through in-situ AERONET-OC datasets, where coccolithophore bloom spectral peaks ranging between 490 nm and 560 nm were observed at a site affected by the green-brownish waters from the river plumes, while farther from the river mouth peaks occurred over a narrower range between 490 nm and 530 nm. The river plume-affected measurement aligns with the conditions in our study, suggesting that the likely reason for the reflectance peak at around 560 nm in our data is the presence of background CDOM in the coastal area.

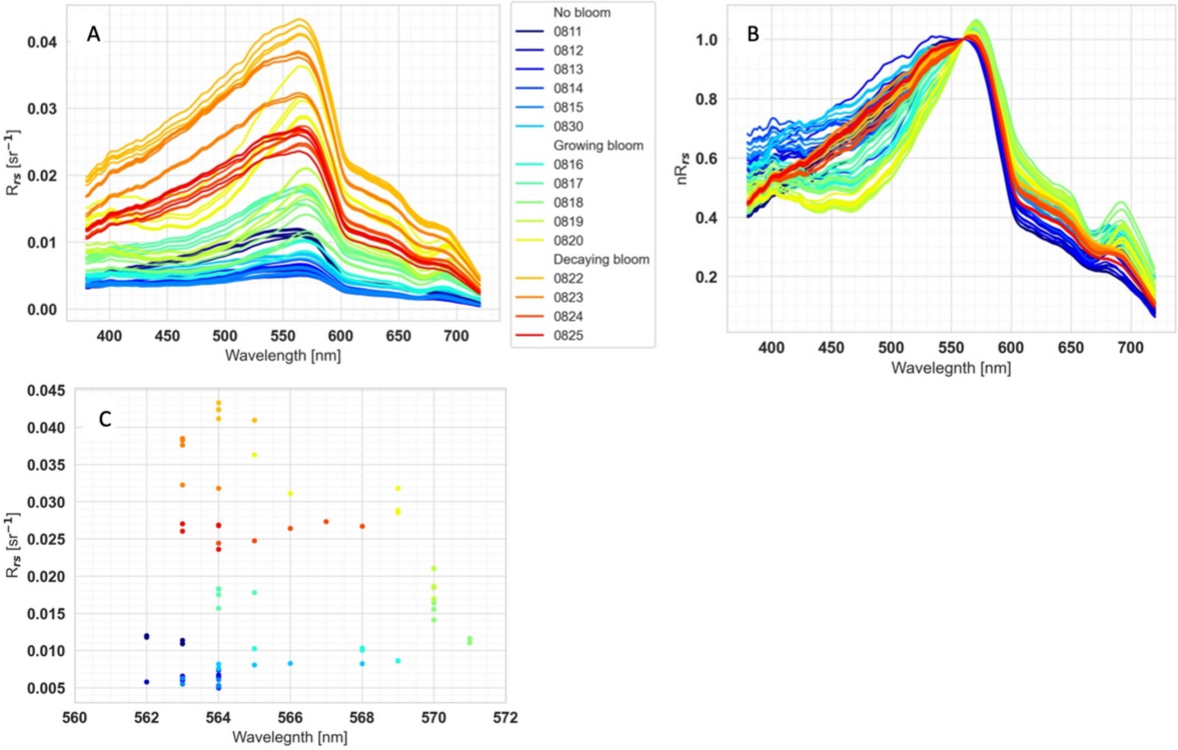

Figure 23| Stations 19-23 time series spectra evolution of (A) R_{rs}^{SST}, (B) nR_{rs}^{SST}, and (C) the peak wavelengths and corresponding R_{rs}^{SST} values for each spectrum in (A). The spectrum and corresponding values are colour-coded to represent measurements from each day.

3.4.2 Evaluation of the Random Forest Classifiers

As shown in Figure 20a, *nRrs(490)* and *nRrs(510)*, the first and fourth most important features used in the RFC10, are influenced by elevated *E. huxleyi* absorption, peaking from 400 to 470 nm and gradually decreasing until 550 nm, similar to Neeley et al. (2015). This pattern contributes to the concavity observed in *nRrs*, serving as a significant characteristic to differentiate the coccolithophore development stages (Figure 16B). However, it is also counterintuitive that, from our results, *nRrs(412)* and *nRrs(443)* are less important than *nRrs(490)* and *nRrs(510)* (Figure 20A). At 412 and 443 nm, the absorption by *E. huxleyi* is even stronger compared to 490 and 510 nm (Neeley et al., 2015), and as such, it should cause a more prominent concavity in *nRrs*. We hypothesize that these results are likely attributable to greater uncertainties in the short blue wavelengths related to the Rrs^{SST} retrievals (Mobley, 1999; Wei et al., 2020; Tilstone et al., 2020), likely because the diffuse skylight (L_i) reflected off the water surface could contaminate the signal detected by the L_t sensor. The skylight is more pronounced at shorter wavelengths because the sky is brightest in the blue bands due to Rayleigh scattering (Mobley, 1999). Despite the proper corrections applied during SAS-ST data processing, as described in Section 3.2.2.1, this contamination can still propagate, leading to increased uncertainties in the blue wavelengths of Rrs^{SST}. Due to the strong resilience of random forest classifiers against noise (Fang, 2011), *nRrs(490)* and *nRrs(510)*, which gernerally have lower reflectance uncertainties (Tilstone et al., 2020), were selected to indicate the influence of pigment absorption on reflectance measurements.

The uncertainties associated with the *Rrs* at shorter blue wavelengths are also prevalent with the RFC10 application on Rrs^{OLCI}. In this case, the suboptimal separation of the decaying and growing bloom groups may stem from the consistent underestimation of Rrs^{OLCI} for the decaying bloom, particularly in the 400, 412 and 443 wavelengths (Figure 18 and Table 4). The underestimation of Rrs^{OLCI} for decaying blooms at these wavelengths resembles the concavity observed in the growing bloom spectra, which results from strong pigment absorption. This similarity in the spectral shape leads to the erroneous classification of 65 decaying bloom observations (68.4% of the total decaying bloom samples) into the growing bloom category (Table 4). However, upon excluding the three problematic 400-443 nm OLCI wavelengths, known for their performance shortcomings, the adapted RFC7 misclassification rate dropped to 28 decaying bloom samples (29.5% of the total decaying bloom samples) being misclassified into the growing bloom category (Table 5). Similar poor performance of *Rrs* values retrieved by OLCI in the blue bands was also reported by Mograne et al. 2019 and Giannini et al. 2021.

3.4.3 Inapplicability of other coccolithophore flags

Following the widely accepted NASA coccolith flag, which is based on thresholds of normalized water-leaving radiance (*Lwn*) and their ratios for three bands from blue and green wavelengths (Brown and Yoder, 1994; Iglesias-Rodríguez et al., 2002), none of the Rrs^{SST} measured in this study were identified as indicative of coccolithophore blooms. However, a large coccolithophore bloom breakout in 2016 in the Salish Sea was reported by NASA (2016), Chandler et al. (2017), Esenkulova et al. (2021), and Simpson et al. (2022). This discrepancy might stem from the inherent nature of our dataset, which pertains to coccolithophore blooms that happened in Case 2 coastal waters, whereas the flag methodology by Iglesias-Rodríguez et al. (2002) was developed for Case 1 open ocean waters (e.g., Moore et al., 2002). The threshold values of the *Lwn* coccolithophore classifier presented by these authors are determined by a parallelepiped algorithm, which categorizes a satellite pixel as either bloom or non-bloom by comparing the spectral properties of the pixel's *Lwn* to the five specific shape and magnitude range that qualify as a bloom. For example, the peak of coccolithophore bloom spectra in our research varied the most within the green wavelengths, divergent from the NASA coccolith flag, which is established on spectral signatures for *Emiliania huxleyi* blooms from several Case 1 open ocean waters, presenting signals at 443 nm surpassing those at 555 nm (Iglesias-Rodríguez et al., 2002). The failure of the NASA coccolith flag has also been observed by Cazzaniga et al. (2021), suggesting that variations in *Rrs* and the corresponding triggering of the NASA coccoliths flag can be impacted by local water optical complexity not related to the bloom phenology. According to Cazzaniga et al. (2021), the algorithm failure could be attributed to the green-brownish optically complex waters of a river plume enriched in sediments and CDOM, in which the spectral peak ranged between 490 nm and 560 nm, similar to the peak wavelengths just over 560 nm of our study. Nevertheless, the authors reported that for the plume-affected waters, only at the decaying bloom stage the coccoliths flag is activated due to the shift of *Rrs* maxima toward the blue center wavelengths with *Rrs(443)* prevailing over *Rrs(551),* thereby inadvertently conforming to the conditions of NASA's coccolith flag. Given these uncertainties and discrepancies in the NASA coccolith flag, the introduction of a machine learning-based coccolith flag for Case 2 water in the Salish Sea area, as delineated in our research, serves as a valuable complement to the existing NASA coccolith flag. It has the added advantage of differentiating the coccolithophore bloom spectral data into two distinct stages of bloom development, enhancing the understanding and identification of coccolithophore phenology.

3.4.4 Limitations of the study

Despite the valuable insights gained regarding coccolithophore bloom classification from this study, several limitations should be acknowledged to comprehensively understand the findings. First, only one water sample, collected approximately 100 km away from the SAS-ST track (Esenkulova et al., 2021), along with satellite imagery (NASA 2016; Chandler et al., 2017), confirmed the coccolithophore bloom outbreak in the Salish Sea in August 2016. To address the limitation of relying on a single *in situ* water sample, future studies could incorporate a larger number of samples analyzed using microscopic examination and flow cytometry to count and identify coccolithophore species and their development stages. Additionally, the acidification method (Riebesell et al., 2011) could be employed to quantify PIC, providing further insights into bloom dynamics.

Second, the generalization of machine learning models, defined as utilizing observed training data to make predictions about new, unseen data, is a critical aspect to consider in developing and deploying these models for real-world applications (Shalev-Shwartz and Ben-David, 2014). Nevertheless, the constrained spatial distribution of the SAS-ST dataset, specifically its coverage of the QoOB route, does not cover the water body closer to the Fraser River, an area characterized by distinct optically active constituents. Consequently, the efficacy of the RFC7 model, as trained on a limited dataset within this research, in applying to a broader geographical scope within the Salish Sea, remains to be assessed.

Lastly, because the full scene OLCI images contain large areas of optically diverse waters influenced by the Fraser River plume, which are not represented in the SAS-ST training dataset, thus applying the RFC7 model beyond the matchup points to the entire image would likely result in misclassification. This is due to the model being trained specifically for scenarios where coccolithophores are the primary variable, without accounting for other sources of optical heterogeneity. Therefore, full-scene classification was beyond the scope of this study and would require additional knowledge of the optically active constituents near the Fraser River, which could be obtained by analyzing FerryBox data collected along the Queen of Alberni route that traverses the Fraser River plume (Travers-Smith et al., 2021). This approach would allow for the quantification of the novel machine learning model's accuracy and help ensure the reliability of coccolithophore bloom classification across broader spatial scales.

3.5 Conclusions

The area extent of coccolithophore bloom is projected to increase across most oceanic water, driven by rising global temperatures associated with climate changes (Winter et al., 2014). Given their ecological importance and sensitivity to climate shifts, monitoring them through satellite remote sensing has become essential, especially due to the limited availability of *in situ* observations and the sheer scale of ocean cover. In August 2016, the Salish Sea experienced an extraordinary coccolithophore bloom of *Emiliania Huxleyi* (NASA 2016; Chandler et al., 2017; Simpson et al., 2022), coinciding with *in situ Rrs* data acquisition for this study. This unprecedented event, the region's largest coccolithophore bloom ever recorded, provided a unique opportunity to investigate coccolithophore dynamics and highlighted the importance of monitoring such blooms in optically complex coastal waters. Below are the main findings of this research:

1. For the non-bloom waters, *Rrs* is relatively flat in shape and low in magnitude. For the growing bloom waters, while *Rrs* increased to moderate magnitude, *nRrs(470)* decreased to below 0.6, as a result of strong pigment absorption in this stage. For the decaying bloom waters, *Rrs* increased to moderate to high magnitude, and the absorption feature in nR*rs(470)* disappeared. *Rrs* peak value exists in the decaying bloom group, with *Rrs(564)* at 0.043 sr^{-1}, i.e., 10 times the lowest value observed during the absence of coccolithophore bloom.

2. The 734 samples acquired by SAS-ST were partitioned into no bloom, growing bloom, and decaying bloom development stages. Their *Rrs* and *nRrs* at 10 OLCI bands were used as predictor variables in a random forest classifier (RFC10) to estimate the belonging groups, with an overall model prediction accuracy of 0.973.

3. *Rrs* acquired by OLCI is underestimated compared with ground truth SAS-ST values, especially in the short and blue wavelengths (400, 412, 443 nm). The decaying bloom group performs worst in these three bands among the three groups. By applying RFC10 to the underestimated OLCI spectra, the satellite spectra could only have a classification accuracy 79.4%.

4. By removing *Rrs* and *nRrs* from 400 nm to 443 nm from the RFC10 model, the coccolithophore bloom classification model RFC7 is developed based on SAS-ST spectra at 7 wavelengths from 490 nm to 709 nm. By applying RFC7 to the OLCI spectra at corresponding 7 wavelengths, the total prediction accuracy increased from 79.4% to 89.1%, an increase in the accuracy for detecting decaying blooms from 29.5% to 65.3%, and an improvement in the Kappa coefficient from 0.14 to 0.66.

In conclusion, this study makes a significant contribution to coastal coccolithophore monitoring efforts (Balch and Mitchell, 2023), providing the first continuous *in situ* hyperspectral observations using a novel autonomous shipborne radiometer system. The integration of *in situ* data from SAS-ST with satellite observations, particularly using OLCI data, demonstrates the successful application of remote sensing for coccolithophore bloom detection using a novel machine learning model in optically complex coastal waters. This approach is novel as it develops a model based on 7 or 10 spectral bands, specifically addressing the unique optical properties of coccolithophore blooms in optically complex Case 2 waters. In contrast, conventional models typically rely on two or three spectral bands and are designed for Case 1 waters. This research also contributes to the global methodology for satellite-based coccolithophore monitoring, offering insights into refining techniques for leveraging satellite data to better capture bloom dynamics in various marine ecosystem.

Chapter 4: Summary and Conclusions

4.1 Thesis Overview

The main goal of this research was to characterize coccolithophore blooms within the Salish Sea, Canada, using autonomous ship-borne *in situ* reflectance and satellite reflectance data. We defined two research objectives to achieve this goal:

(1) In Chapter 2, we develop a methodological framework to facilitate the acquisition, processing, and quality control of above-water remote sensing reflectance obtained with the SAS Solar Tracker system.

We delineated the protocols for deploying the SAS-ST instrument on a commercial ferry and detailed the processing and evaluation procedures for the extensive dataset of high-quality *Rrs* obtained in the coastal waters of BC, Canada. Using autonomous radiometers installed aboard a ship of opportunity, as part of this research crucial steps were developed, including predefined optimal geometry of acquisition, identification and flagging of non-optimal meteorological conditions ($n \approx 1400$), correction for sun glint and skylight contributions, mitigation of structural interferences, and subsequently applying BRDF corrections, and finally *Rrs* quality control ($n=744$). First, despite the constant movement of both the ship and the Sun, optimal viewing geometry was deployed and maintained for SAS-ST to ensure optimal data acquisition, while also avoiding the effects of ship shadow and sea spray, and minimizing perturbations from the ship's superstructure. Second, clear sky conditions were determined based on a meteorological flag derived from the ratio of two wavelengths affected by the Mie scattering of raindrops, successfully identifying 98.5% of the spectra acquired under clear-sky conditions. Third, due to the modification of the radiance field by the existence of the ferry, the ship-specific superstructure perturbation correction factor was applied. This value was determined based on a black-pixel assumption for the infrared band of the lowest-acquired turbid water, resulting in an overall reduction of Rrs^{0+} by 0.00055 sr-1. Fourth, to mitigate the non-isotropic distribution of water-leaving radiances in optically complex waters, a BRDF correction was implemented, resulting in a reduction of $R_{rs}{}^{0+}$ by approximately 5-10%. Finally, quality assessment, employing the method introduced by Wei et al. (2016), revealed consistently high scores for over 90% of Group 1 and Group 2 spectra, indicating that the data are suitable for effectively validating atmospherically corrected satellite-retrieved *Rrs*. These steps were required for minimizing uncertainties associated with above-water *in situ* radiometric measurements, allowing for higher quality reflectance data for further use in the random forest coccolithophore bloom classification model and evaluation of Sentinel-3A OLCI reflectance.

(2) In Chapter 3, we utilized *in situ* measurements collected with SAS-ST as validation matchups for satellite-derived (OLCI from Sentinel-3A) atmospherically corrected Rrs^{0+}, and leveraged both datasets to develop and assess regional machine learning models aimed at monitoring coccolithophore blooms.

Through the analysis of a temporally continuous hyperspectral dataset of coccolithophore bloom reflectance measured by SAS-ST in the Salish Sea region (n=734), following the processing and evaluation protocols outlined in Chapter 2, we successfully identified coccolithophore blooms and categorized spectra into no bloom, growing bloom, and decaying bloom classes. Utilizing *in situ* SAS-ST measured *Rrs* and *nRrs* at 10 OLCI bands as predictor variables in a random forest classifier (RFC10) enabled us to estimate the spectra's belonging groups with an overall model prediction accuracy of 0.973. Applying the RFC10 developed using the SAS-ST 10 bands (400 nm to 709 nm) to the OLCI spectra resulted in a classification accuracy of 0.794. This lower accuracy resulted from including the short wavelength bands (400 nm to 443 nm) in the RFC10 model. A matchup analysis between Sentinel-3A OLCI satellite spectra and SAS-ST *in situ* data revealed the underestimations of *Rrs* acquired by OLCI, particularly in the 400-443 nm range for the decaying bloom group. Consequently, an adapted random forest classifier (RFC7) was developed based on SAS-ST *Rrs* and *nRrs* at seven wavelengths from 490 nm to 709 nm, excluding data from 400 nm to 443 nm. RFC7 increased the overall prediction accuracy for coccolithophore bloom detection in OLCI-measured spectra from 0.794 (RFC10) to 0.891, while increasing the Kappa coefficient from 0.14 to 0.66. These findings demonstrate the successful integration of *in situ* and satellite reflectance data to develop robust machine learning models for monitoring coccolithophore bloom dynamics in the Salish Sea.

4.2 Contributions of the research

This study presents the first detailed evaluation of the autonomous SAS-ST radiometer since its launch in 2015. Utilization of SAS-ST has realized a reduction of costs and labour associated with ocean-based fieldwork. The reflectance dataset provided by SAS-ST improves the understanding of the Salish Sea area, particularly given the scarcity of available matchups prior to its successful operation. Additionally, the SAS-ST installation and data processing methodology proposed in this study are adaptable to other regions worldwide lacking in-situ reflectance data, leveraging ship-of-opportunity platforms, thereby advancing the capacity to supplement a network of fixed platforms hosting above-water sensors like AERONET-OC and WATERHYPERNET.

A central contribution of this thesis is the demonstration of how SAS-ST *in situ* reflectance spectra were crucial for identifying and categorizing coccolithophore blooms into different developmental stages (no bloom, growing and decaying bloom). This *in situ* dataset not only supports the development of a random forest machine learning model for detecting bloom stages but also provides the ground-truth data needed to validate and refine satellite-based algorithms. Furthermore, the application of these models to Sentinel-3A OLCI data revealed the potential for using multispectral satellite reflectance measurements for tracking coccolithophore blooms in the Salish Sea. In addition, the hyperspectral data from SAS-ST have already proven valuable for distinguishing bloom stages, and PACE's hyperspectral capability will further improve the detection and monitoring of coccolithophore blooms, contributing to better global ocean biogeochemistry assessments.

4.3 Limitations and Future Research

Despite our adherence to stringent criteria for data acquisition and processing in our protocols for R_{rs}^{0+} measurements with the SAS-ST, as well as efforts to maximize its potential for application in coccolithophore monitoring, certain limitations persist within this work.

The first limitation arose from the unavailability of a true ship-specific superstructure correction factor for the QoOB. Although we provided a relatively reliable estimation of its value based on the black pixel assumption in the infrared bands for our cleanest water, the lack of direct field measurement hampers validation. In future work, we could consider covering a fixed tower with a white sheet akin to the size of the ferry wall of QoOB. This setup would allow us to measure how the presence of a white reflective surface, similar to the ferry wall, modifies the surrounding radiance field. Alternatively, we could conduct mathematical simulations to achieve a similar quantification.

The second limitation pertains to the assessment of the final R_{rs}^{0+} and the accurate quantification of particular uncertainties associated with its measurement and data processing. These uncertainties arise due to changeable measurement environmental conditions, corrections for sky and sun glint, as well as corrections for ship-induced perturbations and BRDF. The typical procedure involves comparing above water R_{rs}^{0+} against in-situ measurements of subsurface R_{rs}^{0-} or Hydrolight simulation based on concurrent measurements obtained from diverse instruments at the same geographical location. However, our measurement setup precludes such direct comparisons. Instead, we evaluated our R_{rs}^{0+} dataset against a global water dataset proposed by W16, which lacks regional specificity. This limitation complicates the precise quantification of uncertainties in R_{rs}^{0+} measurements. Future efforts should concentrate on refining the uncertainty budget by considering environmental conditions during data acquisition and various steps in data processing. This approach will enhance the robustness of vicarious calibration and atmospheric correction validation provided by SAS-ST for satellite observations.

Finally, despite the utilization of literature discussing the absorption and *Rrs* characteristics of coccolithophores in the analysis, there remains a deficiency in the inclusion of water samples to evaluate the effectiveness of categorizing various stages of coccolithophore blooms.

Incorporating water samples into the evaluation process would enable the application of light and scanning electron microscopy, along with flow cytometry, to count and identify coccolithophore species and development stages, in conjunction with the acidification method to quantify PIC. This approach would facilitate the acquisition of *in situ* measurements pertaining to coccolithophore cells and detached coccolith concentrations, thereby enabling a more comprehensive understanding of the evolutionary phase of each water sample. In future investigations focusing on coccolithophores and other phytoplankton blooms, the collection of such data should be prioritized.

References

Ahmad, Z., Franz, B.A., McClain, C.R., Kwiatkowska, E.J., Werdell, J., Shettle, E.P., Holben, B.N., 2010. New aerosol models for the retrieval of aerosol optical thickness and normalized water-leaving radiances from the SeaWiFS and MODIS sensors over coastal regions and open oceans. Appl Opt. 49, 5545–5560. https://doi.org/10.1364/AO.49.005545

Alikas, K., Ansko, I., Vabson, V., Ansper, A., Kangro, K., Uudeberg, K., Ligi, M., 2020. Consistency of radiometric satellite data over lakes and coastalwaters with local field measurements. Remote Sens.12, 616. https://doi.org/10.3390/rs12040616

Allen, S E, Wolfe, M.A., 2013. Hindcast of the timing of the spring phytoplankton bloom in the strait of Georgia, 1968-2010. Prog Oceanogr. 115, 6–13. https://doi.org/10.1016/j.pocean.2013.05.026

Antoine, D., Guevel, P., Desté, J.F., Bécu, G., Louis, F., Scott, A.J., Bardey, P., 2008. The "BOUSSOLE" Buoy - A new transparent-to-swell taut mooring dedicated to marine optics: Design, tests, and performance at sea. J Atmos Ocean Technol. 25, 968–989. https://doi.org/10.1175/2007JTECHO563.1

Bailey, S.W., Werdell, P.J., 2006. A multi-sensor approach for the on-orbit validation of ocean color satellite data products. Remote Sens Environ. 102, 12–23. https://doi.org/10.1016/j.rse.2006.01.015

Bach, L.T., Riebesell, U., Gutowska, M.A., Federwisch, L., Schulz, K.G., 2015. A unifying concept of coccolithophore sensitivity to changing carbonate chemistry embedded in an ecological framework. Prog Oceanogr. 135, 125–138. https://doi.org/10.1016/J.POCEAN.2015.04.012

Balch, W.M., 2018. The Ecology, Biogeochemistry, and Optical Properties of Coccolithophores. Annual review of marine science. 10(1), 71-98. https://doi.org/10.1146/annurev-marine-121916

Balch, W.M., Drapeau, D.T., Bowler, B.C., Lyczskowski, E., Booth, E.S., Alley, D., 2011. The contribution of coccolithophores to the optical and inorganic carbon budgets during the Southern Ocean Gas Exchange Experiment: New evidence in support of the Great Calcite Belt hypothesis. J Geophys Res Oceans. 116, 1–14. https://doi.org/10.1029/2011JC006941

Balch, W.M., Gordon, H.R., Bowler, B.C., Drapeau, D.T., Booth, E.S., 2005. Calcium carbonate measurements in the surface global ocean based on Moderate-Resolution Imaging Spectroradiometer data. J Geophys Res Oceans. 110. https://doi.org/https://doi.org/10.1029/2004JC002560

Balch, W.M., Kilpatrick, K.A., Holligan, P., Harbour, D., Fernandez, E., 1996. The 1991 coccolithophore bloom in the central North Atlantic. 2. Relating optics to coccolith concentration. Limnol Oceanogr. 41, 1684–1696. https://doi.org/https://doi.org/10.4319/lo.1996.41.8.1684

Balch, W.M., Mitchell, C., 2023. Remote sensing algorithms for particulate inorganic carbon (PIC) and the global cycle of PIC. Earth Sci Rev. 239, 104363. https://doi.org/10.1016/j.earscirev.2023.104363

Barnes, B.B., Cannizzaro, J.P., English, D.C., Hu, C., 2019. Validation of VIIRS and MODIS reflectance data in coastal and oceanic waters: An assessment of methods. Remote Sens Environ. 220, 110–123. https://doi.org/10.1016/j.rse.2018.10.034

Brando, Vittorio E, Lovell, J.L., King, E.A., Boadle, D., Scott, R., Schroeder, T., 2016. The potential of autonomous ship-borne hyperspectral radiometers for the validation of ocean color radiometry data. Remote Sens. 8, 150. https://doi.org/10.3390/rs8020150

Breiman, L., 2001. Random Forests. Mach Learn. 45, 5–32. https://doi.org/10.1023/A:1010933404324

Brewin, R.J.W., Sun, X., Aurin, D.A., Viljoen, J.J., Walsh, C., Sathyendranath, S., 2024. Superyachts could support satellite ocean colour validation. Frontiers in Remote Sensing. 5, 1336494. https://doi.org/10.3389/frsen.2024.1336494

Brown, C.W., Yoder, J.A., 1994. Coccolithophorid blooms in the global ocean. J Geophys Res. 99, 7467–7482. https://doi.org/10.1029/93JC02156

Carswell, T., Costa, M., Young, E., Komick, N., Gower, J., Sweeting, R., 2017. Evaluation of MODIS-aqua atmospheric correction and chlorophyll products of western North American coastal waters based on 13 years of data. Remote Sens. 9, 1–24. https://doi.org/10.3390/rs9101063

Cazzaniga, I., Zibordi, G., Mélin, F., 2021. Spectral variations of the remote sensing reflectance during coccolithophore blooms in the Western Black Sea. Remote Sens Environ. 264, 112607. https://doi.org/10.1016/j.rse.2021.112607

Chandler, P.C., King, S.A., Boldt, J., editors, 2017. State of the Physical, Biological and Selected Fishery Resources of Pacific Canadian Marine Ecosystems in 2016. Canadian Technical Report of Fisheries and Aquatic Sciences 3225.

Clark, D.K., Yarbrough, M.A., Feinholz, M., Flora, S., Broenkow, W., Kim, Y.S., Johnson, B.C., Brown, S.W., Yuen, M., Mueller, J.L., 2003. MOBY, a radiometric buoy for performance monitoring and vicarious calibration of satellite ocean color sensors: measurement and data analysis protocols. Ocean Optics Protocols for Satellite Ocean Color Sensor Validation. Volume 6: Special Topics in Ocean Optics Protocols and Appendices.

Collins, A., Allen, S.E., Pawlowicz, R., 2009. The role of wind in determining the timing of the spring bloom in the Strait of Georgia. Canadian Journal of Fisheries and Aquatic Sciences. 66, 1597–1616. https://doi.org/10.1139/F09-071

Concha, J.A., Bracaglia, M., Brando, V.E., 2021. Assessing the influence of different validation protocols on Ocean Colour match-up analyses. Remote Sens Environ. 259, 112415. https://doi.org/10.1016/j.rse.2021.112415

Congalton, R.G., 1991. A review of assessing the accuracy of classifications of remotely sensed data. Remote Sens Environ. 37, 35–46. https://doi.org/https://doi.org/10.1016/0034-4257(91)90048-B

Cui, T., Zhang, J., Groom, S., Sun, L., Smyth, T., Sathyendranath, S., 2010. Validation of MERIS ocean-color products in the Bohai Sea: A case study for turbid coastal waters. Remote Sens Environ. 114, 2326–2336. https://doi.org/10.1016/j.rse.2010.05.009

Cutler, D.R., Edwards, T.C., Beard, K.H., Cutler, A., Hess, K.T., Gibson, J., Lawler, J.J., 2007. Random forests for classification in ecology. Ecology. 88, 2783–2792. https://doi.org/10.1890/07-0539.1

Dogliotti, A.I., Ruddick, K.G., Nechad, B., Doxaran, D., Knaeps, E., 2015. A single algorithm to retrieve turbidity from remotely-sensed data in all coastal and estuarine waters. Remote Sens Environ. 156, 157–168. https://doi.org/10.1016/J.RSE.2014.09.020

Donlon, C., Berruti, B., Buongiorno, A., Ferreira, M.H., Féménias, P., Frerick, J., Goryl, P., Klein, U., Laur, H., Mavrocordatos, C., Nieke, J., Rebhan, H., Seitz, B., Stroede, J., Sciarra, R., 2012. The Global Monitoring for Environment and Security (GMES) Sentinel-3 mission. Remote Sens Environ. 120, 37–57. https://doi.org/10.1016/j.rse.2011.07.024

Eismann, M.T., 2012. Hyperspectral remote sensing. SPIE Press, Bellingham, Washington.

El-Habashi, A., Ahmed, S., 2019. Analyses of satellite ocean color retrievals show advantage of neural network approaches and algorithms that avoid deep blue bands. J Appl Remote Sens. 13, 1. https://doi.org/10.1117/1.jrs.13.024509

Environment and Climate Change Canada, 2021a. https://climate.weather.gc.ca/climate_data/hourly_data_e.html?hlyRange=1994-02-01%7C2019-01-29&dlyRange=1992-05-01%7C2019-01-29&mlyRange=1992-05-01%7C2006-07-01&StationID=29411&Prov=BC&urlExtension=_e.html&searchType=stnName&optLimit=yearRange&StartYear=1840&EndYear=2019&selRowPerPage=25&Line=1&searchMeth

od=contains&txtStationName=entrance+island&timeframe=1&Year=2016&Month=7&Day=5# [Accessed November 2021].

Environment and Climate Change Canada, 2021b. https://climate.weather.gc.ca/climate_data/hourly_data_e.html?hlyRange=1994-02-01%7C2020-02-26&dlyRange=1991-07-01%7C2020-02-26&mlyRange=1991-01-01%7C1999-07-01&StationID=6831&Prov=BC&urlExtension=_e.html&searchType=stnName&optLimit=yearRange&StartYear=1840&EndYear=2020&selRowPerPage=25&Line=8&searchMethod=contains&txtStationName=sand&timeframe=1&Year=2019&Month=8&Day=28# [Accessed November 2021].

Esenkulova, S., Suchy, K.D., Pawlowicz, R., Costa, M., Pearsall, I.A., 2021. Harmful Algae and Oceanographic Conditions in the Strait of Georgia, Canada Based on Citizen Science Monitoring. Front Mar Sci. 8, 725092. https://doi.org/10.3389/fmars.2021.725092

European Space Agency, 2021. https://sentinel.esa.int/web/sentinel/technical-guides/sentinel-3-olci/olci-instrument/spectral-response-function-data> [Accessed November 2021]

Fan, Y., Li, W., Chen, N., Ahn, J.H., Park, Y.J., Kratzer, S., Schroeder, T., Ishizaka, J., Chang, R., Stamnes, K., 2021. OC-SMART: A machine learning based data analysis platform for satellite ocean color sensors. Remote Sens Environ. 253, 112236. https://doi.org/10.1016/j.rse.2020.112236

Gao, H.X., 2005. Applied mutivariable statistic. Peking University Publication House, Beijing, China.

Garaba, S.P., Voß, D., Wollschläger, J., Zielinski, O., 2015. Modern approaches to shipborne ocean color remote sensing. Appl Opt. 54, 3602. https://doi.org/10.1364/ao.54.003602

Garaba, S.P., Zielinski, O., 2013. Methods in reducing surface reflected glint for shipborne above-water remote sensing. Journal of the European Optical Society. 8, 13058. https://doi.org/10.2971/jeos.2013.13058

Garcia, C.A.E., Garcia, V.M.T., Dogliotti, A.I., Ferreira, A., Romero, S.I., Mannino, A., Souza, M.S., Mata, M.M., 2011. Environmental conditions and bio-optical signature of a coccolithophorid bloom in the Patagonian shelf. J Geophys Res Oceans. 116, C3. https://doi.org/10.1029/2010JC006595

Gege, P., 2014. WASI-2D: A software tool for regionally optimized analysis of imaging spectrometer data from deep and shallow waters. Computers and Geosciences. 62, 208–215. https://doi:10.1016/j.cageo.2013.07.022.

Giannini, F., Hunt, B.P.V., Jacoby, D., Costa, M., 2021. Performance of OLCI Sentinel-3A satellite in the Northeast Pacific coastal waters. Remote Sens Environ. 256, 112317. https://doi.org/10.1016/j.rse.2021.112317

Gordon, H.R., Boynton, G.C., Balch, W.M., Groom, S.B., Harbour, D.S., Smyth, T.J., 2001. Retrieval of coccolithophore calcite concentration from sea WiFS imagery. Geophys Res Let.t 28, 1587–1590. https://doi.org/10.1029/2000GL012025

Gray, P.C., Boss, E., Prochaska, J.X., Kerner, H., Demeaux, C.B., Lehahn, Y., 2024. The Promise and Pitfalls of Machine Learning in Ocean Remote Sensing. Oceanography. 37, 52–63. https://www.jstor.org/stable/27333923.

Groetsch, P.M.M., Gege, P., Simis, S.G.H., Eleveld, M.A., Peters, S.W.M., 2017. Validation of a spectral correction procedure for sun and sky reflections in above-water reflectance measurements. Opt Express. 25, A742. https://doi.org/10.1364/oe.25.00a742

Groom, S.B., Holligan, P.M., 1987. Remote sensing of coccolithophore blooms. Advances in Space Research. 7, 73–78. https://doi.org/10.1016/0273-1177(87)90166-9

Groom, S.B., Sathyendranath, S., Ban, Y., Bernard, S., Brewin, B., Brotas, V., Brockmann, C., Chauhan, P., Choi, J.K., Chuprin, A., Ciavatta, S., Cipollini, P., Donlon, C., Franz, B.A., He, X., Hirata, T., Jackson, T., Kampel, M., Krasemann, H., Lavender, S.J., Pardo-Martinez, S., Melin, F., Platt, T., Santoleri, R., Skakala, J., Schaeffer, B., Smith, M., Steinmetz, F., Valente, A., Wang, M., 2019. Satellite ocean colour: Current status and future perspective. Front Mar Sci. 6, 485. https://doi.org/10.3389/fmars.2019.00485

Guanter, L., Kaufmann, H., Segl, K., Foerster, S., Rogass, C., Chabrillat, S., Kuester, T., Hollstein, A., Rossner, G., Chlebek, C., Straif, C., Fischer, S., Schrader, S., Storch, T., Heiden, U., Mueller, A., Bachmann, M., Mühle, H., Müller, R., Habermeyer, M., Ohndorf, A., Hill, J., Buddenbaum, H., Hostert, P., der Linden, S., Leitão, P.J., Rabe, A., Doerffer, R., Krasemann, H., Xi, H., Mauser, W., Hank, T., Locherer, M., Rast, M., Staenz, K., Sang, B., 2015. The EnMAP Spaceborne Imaging Spectroscopy Mission for Earth Observation. Remote Sens. 7, 8830–8857. https://doi.org/10.3390/rs70708830

Haigh, R., Ianson, D., Holt, C.A., Neate, H.E., Edwards, A.M., 2015. Effects of ocean acidification on temperate coastal marine ecosystems and fisheries in the northeast pacific. PLoS One. 10, 1–46. https://doi.org/10.1371/journal.pone.0117533

Halverson, M., Pawlowicz, R., 2011. Entrainment and flushing time in the Fraser River estuary and plume from a steady salt balance analysis. J Geophys Res Oceans. 116, C8. https://doi.org/10.1029/2010JC006793

Halverson, M.J., Pawlowicz, R., 2008. Estuarine forcing of a river plume by river flow and tides. J Geophys Res Oceans. 113, C9. https://doi.org/10.1029/2008JC004844

Hilborn, A., Costa, M., 2018. Applications of DINEOF to satellite-derived chlorophyll-a from a productive coastal region. Remote Sens. 10, 11–13. https://doi.org/10.3390/rs10091449

Hlaing, S., Harmel, T., Gilerson, A., Foster, R., Weidemann, A., Arnone, R., 2013. Evaluation of the VIIRS ocean color monitoring performance in coastal regions. Remote Sensing of Environment. 139, 398–414. https://doi.org/10.1016/j.rse.2013.08.013.

Holligan, P.M., Balch, W.M., 1991. From the ocean to cells: coccolithophore optics and biogeochemistry, in: Particle Analysis in Oceanography. Springer, pp. 301–324.

Holligan, P.M., Fernández, E., Aiken, J., Balch, W.M., Boyd, P., Burkill, P.H., Finch, M., Groom, S.B., Malin, G., Muller, K., Purdie, D.A., Robinson, C., Trees, C.C., Turner, S.M., van der Wal, P., 1993. A biogeochemical study of the coccolithophore, Emiliania huxleyi, in the North Atlantic. Global Biogeochem Cycles. 7, 879–900. https://doi.org/10.1029/93GB01731

Hooker, S.B., Bernhard, G., Morrow, J.H., Booth, C.R., Comer, T., Lind, R.N., Quang, V., 2012. Optical Sensors for Planetary Radiant Energy (OSPREy): Calibration and Validation of Current and Next-Generation NASA Missions. NASA Tech. Memo. 2011-215872. Greenbelt, Maryland: NASA Goddard Space Flight Center.

Hooker, S.B., Morel, A., 2003. Platform and Environmental Effects on Above-Water Determinations of Water-Leaving Radiances. J Atmos Ocean Technol. 20, 187–205. https://doi.org/10.1175/1520-0426(2003)020<0187:PAEEOA>2.0.CO;2

Hovland, E.K., Hancke, K., Alver, M.O., Drinkwater, K., Høkedal, J., Johnsen, G., Moline, M., Sakshaug, E., 2014. Optical impact of an Emiliania huxleyi bloom in the frontal region of the Barents Sea. Journal of Marine Systems. 130, 228–240. https://doi.org/10.1016/j.jmarsys.2012.07.002

Hu, C., Feng, L., Guan, Q., 2021. A Machine Learning Approach to Estimate Surface Chlorophyll a Concentrations in Global Oceans from Satellite Measurements. IEEE Transactions on Geoscience and Remote Sensing. 59, 4590–4607. https://doi.org/10.1109/TGRS.2020.3016473

Ianson, D., Alllen, S., Gower Jim, Covert Paul, Varela Diana, 2018. Rogue coccolithophore bloom in the Strait of Georgia in 2016: investigating cause and biogeochemical consequences . COMS, June 10-14 2018, Halifax.

Iglesias-Rodríguez, M.D., Brown, C.W., Doney, S.C., Kleypas, J., Kolber, D., Kolber, Z., Hayes, P.K., Falkowski, P.G., 2002. Representing key phytoplankton functional groups in ocean carbon cycle models: Coccolithophorids. Global Biogeochem Cycles. 16, 47-1-47–20. https://doi.org/https://doi.org/10.1029/2001GB001454

Iida, T., Saitoh, S.I., Miyamura, T., Toratani, M., Fukushima, H., Shiga, N., 2002. Temporal and spatial variability of coccolithophore blooms in the eastern Bering Sea, 1998-2001. Prog Oceanogr. 55, 165–175. https://doi.org/https://doi.org/10.1016/S0079-6611(02)00076-9

Ioannou, I., Gilerson, A., Gross, B., Moshary, F., Ahmed, S., 2013. Deriving ocean color products using neural networks. Remote Sens Environ. 134, 78–91. https://doi.org/10.1016/j.rse.2013.02.015

IOCCG, 2014. Phytoplankton functional types from space. Sathyendranath S (ed), Reports of the International Ocean Colour Coordinating Group, No. 15, IOCCG, Dartmouth, Canada.

Jackson, T., Sathyendranath, S., and Mélin, F., 2017. An improved optical classification scheme for the Ocean Colour Essential Climate Variable and its applications. Remote Sensing of Environment. 203, 152–161. https://doi.org/10.1016/j.rse.2017.03.036.

Johannessen, S.C., Macdonald, R.W., Paton, D.W., 2003. A sediment and organic carbon budget for the greater Strait of Georgia. Estuar Coast Shelf Sci. 56, 845–860. https://doi.org/10.1016/S0272-7714(02)00303-7

Kolluru, S., Tiwari, S.P., 2022. Modeling ocean surface chlorophyll-a concentration from ocean color remote sensing reflectance in global waters using machine learning. Science of the Total Environment. 844, 157191. https://doi.org/10.1016/j.scitotenv.2022.157191

Komick, N.M., Costa, M.P.F., Gower, J., 2009. Bio-optical algorithm evaluation for MODIS for western Canada coastal waters: An exploratory approach using *in situ* reflectance. Remote Sens Environ. 113, 794–804. https://doi.org/10.1016/j.rse.2008.12.005

Krumhardt, K.M., Lovenduski, N.S., Iglesias-Rodriguez, M.D., Kleypas, J.A., 2017. Coccolithophore growth and calcification in a changing ocean. Prog Oceanogr. 159, 276-295. https://doi.org/10.1016/j.pocean.2017.10.007

Kruse, F.A., Lefkoff, A.B., Boardman, J.W., Heidebrecht, K.B., Shapiro, A.T., Barloon, P.J., Goetz, A.F.H., 1993. The spectral image processing system (SIPS)-interactive visualization and analysis of imaging spectrometer data. Remote Sens Environ. 44, 145–163. https://doi.org/10.1016/0034-4257(93)90013-N

Le, C., Li, Y., Zha, Y., Sun, D., Huang, C., Zhang, H., 2011. Remote estimation of chlorophyll a in optically complex waters based on optical classification. Remote Sens Environ. 115, 725–737. https://doi.org/10.1016/j.rse.2010.10.014

Lee, Z., Ahn, Y.-H., Mobley, C., Arnone, R., 2010. Removal of surface-reflected light for the measurement of remote-sensing reflectance from an above-surface platform. Opt Express. 18, 26313. https://doi.org/10.1364/oe.18.026313

Lee, Z., Carder, K.L., Arnone, R.A., 2002. Deriving inherent optical properties from water color: a multiband quasi-analytical algorithm for optically deep waters. Appl Opt. 41, 5755. https://doi.org/10.1364/ao.41.005755

Lee, Z.P., Du, K., Voss, K.J., Zibordi, G., Lubac, B., Arnone, R., Weidemann, A., 2011. An inherent-optical-property-centered approach to correct the angular effects in water-leaving radiance. Appl Opt. 50, 3155–3167. https://doi.org/10.1364/AO.50.003155

Li, M., Gargett, A., Denman, K., 2000. What determines seasonal and interannual variability of phytoplankton and zooplankton in strongly estuarine systems? Application to the semi-enclosed estuary of Strait of Georgia and Juan de Fuca Strait. Estuar Coast Shelf Sci. 50, 467–488. https://doi.org/10.1006/ecss.2000.0593

Loizzo, R., Guarini, R., Longo, F., Scopa, T., Formaro, R., Facchinetti, C., Varacalli, G., 2018. Prisma: The Italian Hyperspectral Mission, in: IGARSS 2018 - 2018 IEEE International Geoscience and Remote Sensing Symposium. pp. 175–178. https://doi.org/10.1109/IGARSS.2018.8518512

Loos, E.A., Costa, M., 2010. Inherent optical properties and optical mass classification of the waters of the Strait of Georgia, British Columbia, Canada. Prog Oceanogr. 87, 144–156. https://doi.org/10.1016/j.pocean.2010.09.004

Mannino, A., Novak, M.G., Hooker, S.B., Hyde, K., Aurin, D., 2014. Algorithm development and validation of CDOM properties for estuarine and continental shelf waters along the northeastern U.S. coast. Remote Sens Environ. 152, 576–602. https://doi.org/10.1016/J.RSE.2014.06.027

Marchese, C., Hunt, B.P.V., Giannini, F., Ehrler, M., Costa, M., 2022. Bioregionalization of the coastal and open oceans of British Columbia and Southeast Alaska based on Sentinel-3A satellite-derived phytoplankton seasonality. Front Mar Sci. 9, 968470. https://doi.org/10.3389/fmars.2022.968470

Masson, D., 2006. Seasonal water mass analysis for the Straits of Juan de Fuca and Georgia. Atmosphere – Ocean. 44, 1–15. https://doi.org/10.3137/ao.440101

Masson, D., 2002. Deep water renewal in the strait of Georgia. Estuar Coast Shelf Sci. 54, 115–126. https://doi.org/10.1006/ecss.2001.0833

Masson, D., Peña, A., 2009. Chlorophyll distribution in a temperate estuary: The Strait of Georgia and Juan de Fuca Strait. Estuar Coast Shelf Sci. 82, 19–28. https://doi.org/10.1016/j.ecss.2008.12.022

Mélin, F., 2022. Validation of ocean color remote sensing reflectance data: Analysis of results at European coastal sites. Remote Sens Environ. 280, 113153. https://doi.org/10.1016/j.rse.2022.113153

Mélin, F., Vantrepotte, V., Clerici, M., D'Alimonte, D., Zibordi, G., Berthon, J.F., Canuti, E., 2011. Multi-sensor satellite time series of optical properties and chlorophyll-a concentration in the Adriatic Sea. Prog Oceanogr. 91, 229–244. https://doi.org/10.1016/J.POCEAN.2010.12.001

Mitchell, C., Hu, C., Bowler, B., Drapeau, D., Balch, W.M., 2017. Estimating Particulate Inorganic Carbon Concentrations of the Global Ocean From Ocean Color Measurements Using a Reflectance Difference Approach. J Geophys Res Oceans. 122, 8707–8720. https://doi.org/10.1002/2017JC013146

Mobley, C.D., 1999. Estimation of the remote-sensing reflectance from above-surface measurements. Appl Opt. 38, 7442–7455. https://doi.org/10.1364/AO.38.007442

Moore, T. S., Campbell, J. W., and Dowell, M. D., 2009. A class-based approach to characterizing and mapping the uncertainty of the MODIS ocean chlorophyll product. Remote Sensing of Environment. 113, 2424–2430 https://doi.org/10.1016/j.rse.2009.07.016.

Moore, Timothy S, Dowell, M.D., Franz, B.A., 2012. Detection of coccolithophore blooms in ocean color satellite imagery: A generalized approach for use with multiple sensors. Remote Sens Environ. 117, 249–263. https://doi.org/10.1016/j.rse.2011.10.001

Moore, T. S., Dowell, M. D., Bradt, S., and Ruiz Verdu, A., 2014. An optical water type framework for selecting and blending retrievals from bio-optical algorithms in lakes and coastal waters. Remote Sensing of Environment 143, 97–111. https://doi.org/10.1016/j.rse.2013.11.021.

Morel, A., Bricaud, A., 1981. Theoretical results concerning light absorption in a discrete medium, and application to specific absorption of phytoplankton. Deep Sea Research Part A, Oceanographic Research Papers. https://doi.org/10.1016/0198-0149(81)90039-X

Morel, A., Gentili, B., 1996. Diffuse reflectance of oceanic waters III Implication of bidirectionality for the remote-sensing problem. Appl Opt. 35, 4850. https://doi.org/10.1364/ao.35.004850

Morel, A., Antoine, D., and Gentili, B., 2002. Bidirectional reflectance of oceanic waters: accounting for Raman emission and varying particle scattering phase function. Applied Optics. 41, 6289. https://doi.org/10.1364/ao.41.006289.

Mograne, M.A., Jamet, C., Loisel, H., Vantrepotte, V., Mériaux, X., Cauvin, A., 2019. Evaluation of Five Atmospheric Correction Algorithms over French Optically-Complex Waters for the Sentinel-3A OLCI Ocean Color Sensor. Remote Sens. 11, 668. https://doi.org/10.3390/rs11060668

Müller, D., Krasemann, H., Brewin, R. J. W., Brockmann, C., Deschamps, P. Y., Doerffer, R., 2015. The Ocean Colour Climate Change Initiative: I. A methodology for assessing atmospheric correction processors based on in-situ measurements. Remote Sensing of Environment. 162, 242–256. https://doi.org/10.1016/j.rse.2013.11.026.

Nasiha, H.J., Wang, Z., Giannini, F., Costa, M., 2022. Spatial Variability of *In situ* Above-Water Reflectance in Coastal Dynamic Waters: Implications for Satellite Match-Up Analysis. Frontiers in Remote Sensing. 3, 876748. https://doi.org/10.3389/frsen.2022.876748

NASA., 2016. The Strait of Georgia turns milky green due to an "unprecedented" explosion of coccolithophores. Earth Observatory. Retrieved from https://earthobservatory.nasa.gov/images/88687/canadian-waters-teem-with-phytoplankton

Neeley, A.R., Freeman, S.A., Harris, L.A., 2015. Multi-method approach to quantify uncertainties in the measurements of light absorption by particles. Opt Express. 23, 31043. https://doi.org/10.1364/oe.23.031043

Nemcek, N., Hennekes, M., Sastri, A., Perry, R.I., 2023. Seasonal and spatial dynamics of the phytoplankton community in the Salish Sea, 2015–2019. Prog Oceanogr. 217, 103108. https://doi.org/10.1016/j.pocean.2023.103108

Neukermans, G., Fournier, G., 2018. Optical modeling of spectral backscattering and remote sensing reflectance from Emiliania huxleyi Blooms. Front Mar Sci. 5, 1–20. https://doi.org/10.3389/fmars.2018.00146

Neukermans, G., Oziel, L., Babin, M., 2018. Increased intrusion of warming Atlantic water leads to rapid expansion of temperate phytoplankton in the Arctic. Glob Chang Biol. 24, 2545–2553. https://doi.org/10.1111/gcb.14075

Ottaviani, M., Foster, R., Gilerson, A., Ibrahim, A., Carrizo, C., El-Habashi, A., Cairns, B., Chowdhary, J., Hostetler, C., Hair, J., Burton, S., Hu, Y., Twardowski, M., Stockley, N., Gray, D., Slade, W., Cetinic, I., 2018. Airborne and shipborne polarimetric measurements over open ocean and coastal waters: Intercomparisons and implications for spaceborne observations. Remote Sens Environ. 206, 375–390. https://doi.org/10.1016/j.rse.2017.12.015

Park, Y.J., Ruddick, K., 2005. Model of remote-sensing reflectance including bidirectional effects for case 1 and case 2 waters. Appl Opt. 44, 1236–1249. https://doi.org/10.1364/AO.44.001236

Pawlowicz, R., di Costanzo, R., Halverson, M., Devred, E., Johannessen, S., 2017. Advection, Surface Area, and Sediment Load of the Fraser River Plume Under Variable Wind and

River Forcing. Atmosphere – Ocean. 55, 293–313. https://doi.org/10.1080/07055900.2017.1389689

Pawlowicz, R., Hannah, C., Rosenberger, A., 2019. Lagrangian observations of estuarine residence times, dispersion, and trapping in the Salish Sea. Estuar Coast Shelf Sci. 225, 106246. https://doi.org/10.1016/j.ecss.2019.106246

Phillips, S.R., Costa, M., 2017. Spatial-temporal bio-optical classification of dynamic semi-estuarine waters in western North America. Estuar Coast Shelf Sci. 199, 35–48. https://doi.org/10.1016/j.ecss.2017.09.029

Pospelova, V., Esenkulova, S., Johannessen, S.C., O'Brien, M.C., Macdonald, R.W., 2010. Organic-walled dinoflagellate cyst production, composition and flux from 1996 to 1998 in the central Strait of Georgia (BC, Canada): A sediment trap study. Mar Micropaleontol. 75, 17–37. https://doi.org/10.1016/j.marmicro.2010.02.003

Pramlall, S., Jackson, J.M., Marchese, C., Suchy, K.D., Hunt, B.P.V., Costa, M., 2024. Mapping phenoregions and phytoplankton seasonality in Northeast Pacific marine coastal ecosystems via a satellite-based approach. Prog Oceanogr. 228, 103336. https://doi.org/10.1016/j.pocean.2024.103336

Riebesell, U., Fabry, V.J., Hansson, L., Gattuso, J.-P., 2011. Guide to best practices for ocean acidification research and data reporting. Office for Official Publications of the European Communities.

Rosenfield, G. H., and Fitzpatrick-Lins, K., 1984. ANALYSIS OF A CLASSIFICATION ERROR MATRIX USING CATEGORICAL DATA TECHNIQUES. Sioux Falls, ND, US. IEEE.

Ruddick, K.G., Cauwer, V. De, Park, Y., Moore, G., 2006. Seaborne measurements of near infrared water-leaving reflentance: The similarity spectrum for turbid waters. Limnology. 51, 1167–1179.

Ruddick, K.G., Voss, K., Boss, E., Castagna, A., Frouin, R., Gilerson, A., Hieronymi, M., Carol Johnson, B., Kuusk, J., Lee, Z., Ondrusek, M., Vabson, V., Vendt, R., 2019. A review of protocols for fiducial reference measurements of water-leaving radiance for validation of satellite remote-sensing data over water. Remote Sens. 11, 2198. https://doi.org/10.3390/rs11192198

Sathyendranath, S., Brewin, R.J.W., Ciavatta, S., Jackson, T., Kulk, G., Jönsson, B., Vicente, V.M., Platt, T., 2023. Ocean Biology Studied from Space. Surv Geophys. 44(5), 1287-1308. https://doi.org/10.1007/s10712-023-09805-9

Sathyendranath, S., Brewin, R.J.W., Jackson, T., Mélin, F., Platt, T., 2017. Ocean-colour products for climate-change studies: What are their ideal characteristics? Remote Sens Environ. 203, 125–138. https://doi.org/10.1016/j.rse.2017.04.017

Satlantic, 2016. SAS Solar Tracker Operation Manual.

Satlantic, 2011. Satlantic Instrument File Standard, Ver. 6.1.

Seegers, B.N., Stumpf, R.P., Schaeffer, B.A., Loftin, K.A., Werdell, P.J., 2018. Performance metrics for the assessment of satellite data products: an ocean color case study. Opt Express. 26, 7404. https://doi.org/10.1364/oe.26.007404

Shalev-Shwartz, S., Ben-David, S., 2014. Understanding machine learning: From theory to algorithms. Cambridge university press.

Shutler, J.D., Grant, M.G., Miller, P.I., Rushton, E., Anderson, K., 2010. Coccolithophore bloom detection in the north east Atlantic using SeaWiFS: Algorithm description, application and sensitivity analysis. Remote Sens Environ. 114, 1008–1016. https://doi.org/10.1016/j.rse.2009.12.024

Simis, S.G.H., Olsson, J., 2013. Unattended processing of shipborne hyperspectral reflectance measurements. Remote Sens Environ. 135, 202–212. https://doi.org/10.1016/j.rse.2013.04.001

Simpson, E., Ianson, D., Kohfeld, K.E., 2022. Using End-Member Models to Estimate Seasonal Carbonate Chemistry and Acidification Sensitivity in Temperate Estuaries. Geophys Res Lett. 49(2), e2021GL095579. https://doi.org/10.1029/2021GL095579

Smyth, T.J., Moore, G.F., Groom, S.B., Land, P.E., Tyrrell, T., 2002. Optical modeling and measurements of a coccolithophore bloom. Appl Opt. 41, 7679–7688. https://doi.org/10.1364/AO.41.007679

Steinmetz, F., Ramon, D., Deschamps, P.Y., 2016. ATBD v1 - Polymer Atmospheric Correction Algorithm ref: D2.3 Date: 23/12/2016 Issue: 2.1. PML, United Kingdom.

Suchy, K.D., le Baron, N., Hilborn, A., Perry, R.I., Costa, M., 2019. Influence of environmental drivers on spatio-temporal dynamics of satellite-derived chlorophyll a in the Strait of Georgia. Prog Oceanogr. 176, 102134. https://doi.org/10.1016/j.pocean.2019.102134

Talone, M., Zibordi, G., 2019. Spectral assessment of deployment platform perturbations in above-water radiometry. Opt Express. 27, A878. https://doi.org/10.1364/oe.27.00a878

Talone, M., Zibordi, G., Lee, Z., 2018. Correction for the non-nadir viewing geometry of AERONET-OC above water radiometry data: an estimate of uncertainties. Opt Express. 26, A541. https://doi.org/10.1364/oe.26.00a541

Tilstone, G., Dall'Olmo, G., Hieronymi, M., Ruddick, K., Beck, M., Ligi, M., Costa, M., D'Alimonte, D., Vellucci, V., Vansteenwegen, D., Bracher, A., Wiegmann, S., Kuusk, J., Vabson, V., Ansko, I., Vendt, R., Donlon, C., Casal, T., 2020. Field intercomparison of radiometer measurements for ocean colour validation. Remote Sens. 12(10), 1587. https://doi.org/10.3390/rs12101587

Travers-Smith, H., Giannini, F., Sastri, A.R., Costa, M., 2021. Validation of Non-photochemical Quenching Corrections for Chlorophyll-a Measurements Aboard Ships of Opportunity. Front Mar Sci. 8, 1–15. https://doi.org/10.3389/fmars.2021.686750

Tyralis, H., Papacharalampous, G., Langousis, A., 2019. A brief review of random forests for water scientists and practitioners and their recent history in water resources. Water. 11(5), 910. https://doi.org/10.3390/w11050910

Tyrrell, T., Holligan, P.M., Mobley, C.D., 1999. Optical impacts of oceanic coccolithophore blooms. J Geophys Res Oceans. 104, 3223–3241. https://doi.org/https://doi.org/10.1029/1998JC900052

Tyrrell, T., Merico, A., 2004. Emiliania huxleyi: bloom observations and the conditions that induce them, in: Coccolithophores: From Molecular Processes to Global Impact. Springer, pp. 75–97.

Vabson, V., Kuusk, J., Ansko, I., Vendt, R., Alikas, K., Ruddick, K., Ansper, A., Bresciani, M., Burmester, H., Costa, M., D'Alimonte, D., Dall'Olmo, G., Damiri, B., Dinter, T., Giardino, C., Kangro, K., Ligi, M., Paavel, B., Tilstone, G., van Dommelen, R., Wiegmann, S., Bracher, A., Donlon, C., Casal, T., 2019. Field intercomparison of radiometers used for satellite validation in the 400-900 nm range. Remote Sens. 11(9), 1101. https://doi.org/10.3390/rs11091129

Valente, A., Sathyendranath, S., Brotas, V., Groom, S., Grant, M., Jackson, T., Chuprin, A., Taberner, M., Airs, R., Antoine, D., Arnone, R., Balch, W.M., Barker, K., Barlow, R., Bélanger, S., Berthon, J.F., Beşiktepe, Ş., Borsheim, Y., Bracher, A., Brando, V., Brewin, R.J.W., Canuti, E., Chavez, F.P., Cianca, A., Claustre, H., Clementson, L., Crout, R., Ferreira, A., Freeman, S., Frouin, R., García-Soto, C., Gibb, S.W., Goericke, R., Gould, R., Guillocheau, N., Hooker, S.B., Hu, C., Kahru, M., Kampel, M., Klein, H., Kratzer, S., Kudela, R., Ledesma, J., Lohrenz, S., Loisel, H., Mannino, A., Martinez-Vicente, V., Matrai, P., Mckee, D., Mitchell, B.G., Moisan, T., Montes, E., Muller-Karger, F., Neeley, A., Novak, M., O'dowd, L., Ondrusek, M., Platt, T., Poulton, A.J., Repecaud, M., Röttgers, R., Schroeder, T., Smyth, T., Smythe-Wright, D., Sosik, H.M., Thomas, C., Thomas, R., Tilstone, G., Tracana, A., Twardowski, M., Vellucci, V., Voss, K., Werdell, J., Wernand, M., Wojtasiewicz, B., Wright, S., Zibordi, G., 2022. A compilation of global bio-optical *in situ* data for ocean colour satellite applications – version three. Earth Syst Sci Data. 14, 5737–5770. https://doi.org/10.5194/essd-14-5737-2022

Valente, A., Sathyendranath, S., Brotas, V., Groom, S., Grant, M., Taberner, M., Antoine, D., Arnone, R., Balch, W.M., Barker, K., Barlow, R., Bélanger, S., Berthon, J.F., Beşiktepe, S., Borsheim, Y., Bracher, A., Brando, V., Canuti, E., Chavez, F., Cianca, A., Claustre, H., Clementson, L., Crout, R., Frouin, R., García-Soto, C., Gibb, S.W., Gould, R., Hooker, S.B., Kahru, M., Kampel, M., Klein, H., Kratzer, S., Kudela, R., Ledesma, J., Loisel, H., Matrai, P., Mckee, D., Mitchell, B.G., Moisan, T., Muller-Karger, F., O'Dowd, L., Ondrusek, M., Platt, T., Poulton, A.J., Repecaud, M., Schroeder, T., Smyth, T., Smythe-Wright, D., Sosik, H.M., Twardowski, M., Vellucci, V., Voss, K., Werdell, J., Wernand, M., Wright, S., Zibordi, G., 2019. A compilation of global bio-optical *in situ* data for ocean-colour satellite applications - Version two, Earth System Science Data. 11(3), 1037-1068. https://doi.org/10.5194/essd-11-1037-2019

Vandenberg, N., Costa, M., Coady, Y., Agbaje, T., 2017. PySciDON: A python scientific framework for development of ocean network applications. 2017 IEEE Pacific Rim Conference on Communications, Computers and Signal Processing, PACRIM, Victoria, BC, Canada, 21-23 Aug. 2017. https://doi.org/10.1109/PACRIM.2017.8121926

Vanhellemont, Q., Ruddick, K., 2021. Atmospheric correction of Sentinel-3/OLCI data for mapping of suspended particulate matter and chlorophyll-a concentration in Belgian turbid coastal waters. Remote Sens Environ. 256, 112284. https://doi.org/10.1016/j.rse.2021.112284

Vansteenwegen, D., Ruddick, K., Cattrijsse, A., Vanhellemont, Q., Beck, M., 2019. The pan-and-tilt hyperspectral radiometer system (PANTHYR) for autonomous satellite validation measurements-Prototype design and testing. Remote Sens. 11(11), 1360. https://doi.org/10.3390/rs11111360

Vishnu, P.S., Xi, H., Belluz, J.D.B., Hussain, M.S., Bracher, A., Costa, M., 2022. Seasonal dynamics of major phytoplankton functional types in the coastal waters of the west coast of Canada derived from OLCI Sentinel 3A. Front Mar Sci. 9, 1018510. https://doi.org/10.3389/fmars.2022.1018510

Wang, Z., Costa, M., 2022. Autonomous Shipborne *In situ* Reflectance Data in Optically Complex Coastal Waters: A Case Study of the Salish Sea, Canada. Frontiers in Remote Sensing. 3, 867570. https://doi.org/10.3389/frsen.2022.867570

Wang, M., Shi, W., 2005. Estimation of ocean contribution at the MODIS near-infrared wavelengths along the east coast of the U.S.: Two case studies. Geophys Res Lett 32, 1–5. https://doi.org/10.1029/2005GL022917

Wei, J., Lee, Z., Shang, S., 2016. A system to measure the data quality of spectral remote-sensing reflectance of aquatic environments. J Geophys Res Oceans. 121, 8189–8207. https://doi.org/https://doi.org/10.1002/2016JC012126

Wei, J., Yu, X., Lee, Z., Wang, M., Jiang, L., 2020. Improving low-quality satellite remote sensing reflectance at blue bands over coastal and inland waters. Remote Sens Environ. 250, 112029. https://doi.org/10.1016/j.rse.2020.112029

Werdell, P.J., Behrenfeld, M.J., Bontempi, P.S., Boss, E., Cairns, B., Davis, G.T., Franz, B.A., Gliese, U.B., Gorman, E.T., Hasekamp, O., Knobelspiesse, K.D., Mannino, A., Martins, J.V., McClain, C.R., Meister, G., Remer, L.A., 2019. The Plankton, Aerosol, Cloud, Ocean Ecosystem Mission: Status, Science, Advances. Bull Am Meteorol Soc. 100, 1775–1794. https://doi.org/https://doi.org/10.1175/BAMS-D-18-0056.1

Werdell, P.J., McKinna, L.I.W., Boss, E., Ackleson, S.G., Craig, S.E., Gregg, W.W., Lee, Z., Maritorena, S., Roesler, C.S., Rousseaux, C.S., Stramski, D., Sullivan, J.M., Twardowski, M.S., Tzortziou, M., Zhang, X., 2018. An overview of approaches and challenges for retrieving marine inherent optical properties from ocean color remote sensing. Prog Oceanogr. 160, 186–212. https://doi.org/10.1016/j.pocean.2018.01.001

Wernand, M. R. (2002). Guidelines for (Ship-Borne) Auto-Monitoring of Coastal and Ocean Colour. Oceanographic Society. Proceedings of Ocean Optics XVI, Santa-Fe, NM, USA, November 18-22, 2002.

Winter, A., Henderiks, J., Beaufort, L., Rickaby, R.E.M., Brown, C.W., 2014. Poleward expansion of the coccolithophore Emiliania huxleyi. J Plankton Res. 36(2), 316-325. https://doi.org/10.1093/plankt/fbt110

Young, J., Geisen, M., Cros, L., Kleijne, A., Sprengel, C., Probert, I., Østergaard, J., 2003. A guide to extant coccolithophore taxonomy, Journal of Nannoplankton Research Special Issue. 1(1), 1-132.

Yunker, M.B., Macdonald, R.W., 2003. Alkane and PAH depositional history, sources and fluxes in sediments from the Fraser River Basin and Strait of Georgia, Canada. Org Geochem. 34, 1429–1454. https://doi.org/10.1016/S0146-6380(03)00136-0

Zibordi, G., 2016. Experimental evaluation of theoretical sea surface reflectance factors relevant to above-water radiometry. Opt Express. 24, A446. https://doi.org/10.1364/oe.24.00a446

Zibordi, G., Berthon, J.F., Mélin, F., D'Alimonte, D., Kaitala, S., 2009a. Validation of satellite ocean color primary products at optically complex coastal sites: Northern Adriatic Sea, Northern Baltic Proper and Gulf of Finland. Remote Sens Environ. 113, 2574–2591. https://doi.org/10.1016/j.rse.2009.07.013

Zibordi, G., Holben, B., Slutsker, I., Giles, D., D'alimonte, D., Mélin, F., Berthon, J.F., Vandemark, D., Feng, H., Schuster, G., Fabbri, B.E., Kaitala, S., Seppälä, J., 2009b. AERONET-OC: A network for the validation of ocean color primary products. J Atmos Ocean Technol. 26, 1634–1651. https://doi.org/10.1175/2009JTECHO654.1

Zibordi, G., Melin, F., Berthon, J.F., 2018. A regional assessment of OLCI data products. IEEE Geoscience and Remote Sensing Letters. 15, 1490–1494. https://doi.org/10.1109/LGRS.2018.2849329

Zibordi, Giuseppe, Mélin, F., Berthon, J.-F., Talone, Marco., 2015a. *In situ* autonomous optical radiometry measurements for satellite ocean color validation in the Western Black Sea. Ocean Science. 11, 275–286. https://doi.org/10.5194/os-11-275-2015

Zibordi, Giuseppe, Mélin, F., Voss, K.J., Johnson, B.C., Franz, B.A., Kwiatkowska, E., Huot, J.P., Wang, M., Antoine, D., 2015b. System vicarious calibration for ocean color climate change applications: Requirements for *in situ* data. Remote Sens Environ. 159, 361–369. https://doi.org/10.1016/j.rse.2014.12.015

Zibordi, G, Strömbeck, N., Mélin, F., Berthon, J.F., 2006. Tower-based radiometric observations at a coastal site in the Baltic Proper. Estuar Coast Shelf Sci 69, 649–654. https://doi.org/10.1016/j.ecss.2006.05.022

Appendix

Appendix A:

1. Deployment setup of SAS-ST.
    - Home orientation: -90° (the angle of home position with respect to the ship heading, negative indicates counterclockwise rotation);
    - Backward limit: -90 ° (counterclockwise rotation range with respect to the home position);
    - Forward limit: 10 ° (clockwise rotation range with respect to the home position);
    - High Sun elevation: 90 ° (data acquisition happens only if the sun elevation is below this angle);
    - Low Sun elevation: 30 ° (data acquisition occurs only if the sun elevation is above this angle);
    - View angle: 120 ° (the drive unit will point the sensors at this azimuth angle from the Sun); and
    - View accuracy: 5 ° (the motor will adjust the sensors' pointing direction if it differs by more than the view accuracy from the specified view angle; in this case, the sensors were pointing at 120±5° azimuth angle from the Sun).

2. The summary plot of R_{rs} and accompanying E_s, L_i, L_t for the 16 sampled days.

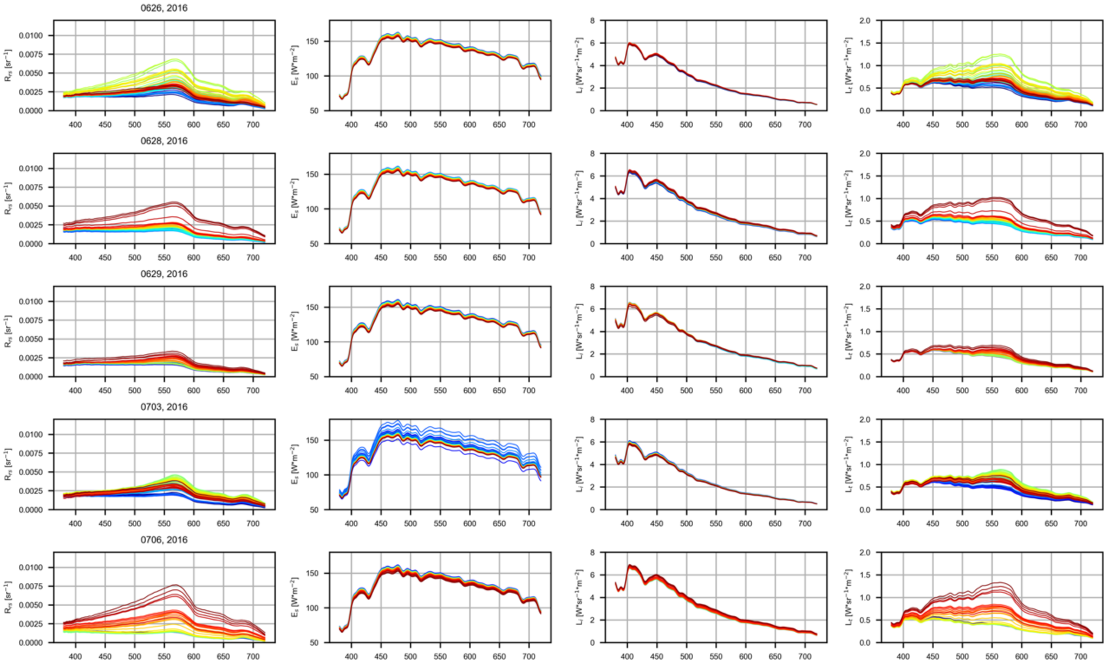

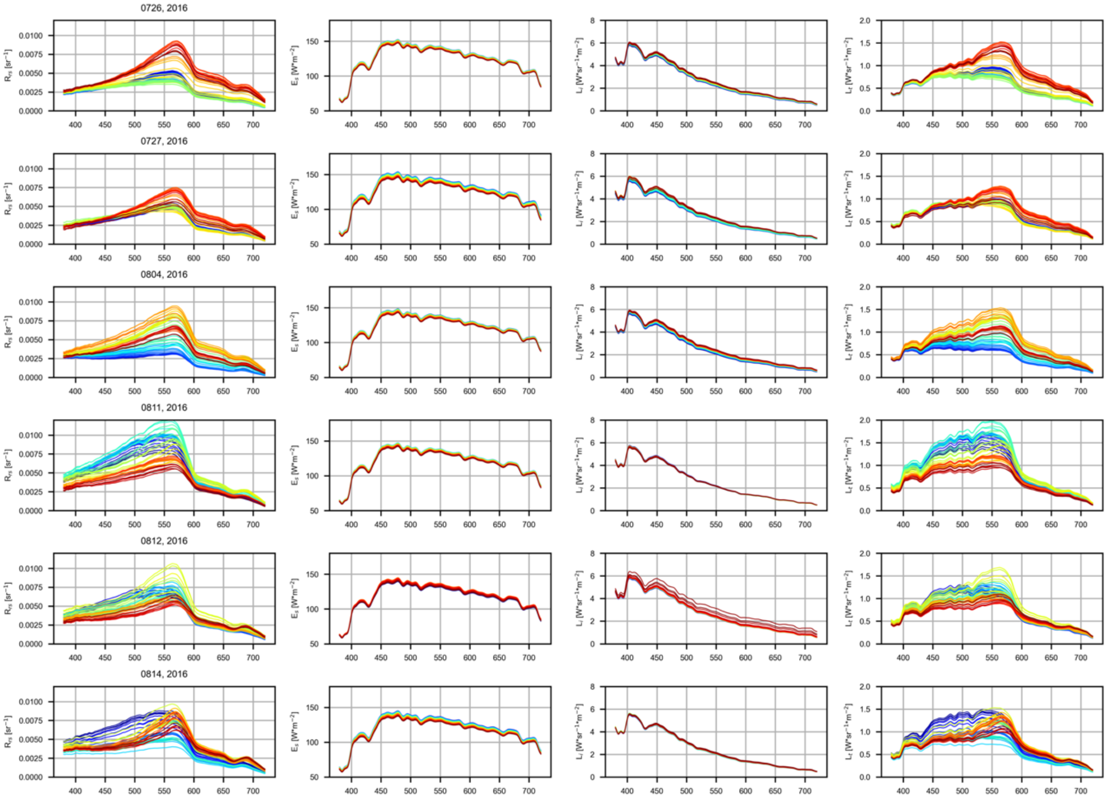

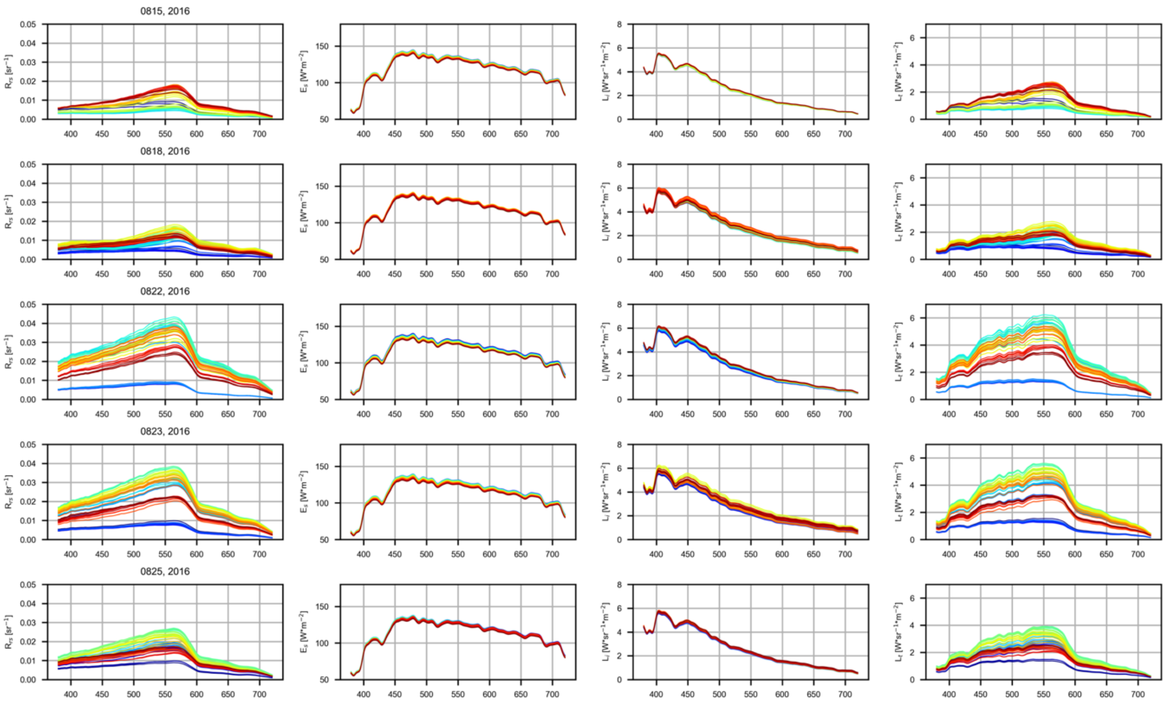

Appendix B: Python code for machine learning algorithm

```
import pandas as pd
import numpy as np
from glob import glob
import os
import matplotlib.pyplot as plt
import matplotlib as mpl
mpl.rcParams["font.family"] = 'Arial'
mpl.rcParams["font.size"] = 12
mpl.rcParams["font.weight"] = 'bold'

from sklearn.neighbors import KNeighborsClassifier
import seaborn as sns
```

```
if __name__ == "__main__":
    global dateAll
    global path
    global pathin
    global pathout


    path='/Users/wangziwei/Google Drive/202206/'
    pathin=path+'1 SAS_FB/5_SAS_coccolith_flag_manual/'
    pathout=path+'1 SAS_FB/5_SAS_coccolith_flag_manual/3_SAS_manual_coccolith_flag_analysis/'

sas=pd.read_excel(pathin+'all_15_days_SAS_Rrs_nRrs_OLCIwl_name_organized.xlsx',index_col=0)
    data=sas.drop(['date','pins'],axis=1)


#%% Randon forest


# train test split
from sklearn.ensemble import RandomForestClassifier


from sklearn.model_selection import train_test_split


x,y = data.loc[:,data.columns != 'bloom_flag'], data.loc[:,'bloom_flag']


x_train,x_test,y_train,y_test = train_test_split(x,y,test_size = 0.3,random_state = 1)


#%% hyperparameter tuning


def print_results(results):
```

```
   #print('BEST score: {},BEST PARAMS:
{}'.format(round(results.best_score_,3),results.best_params_))
   print('BEST score: {},STD: {},BEST PARAMS:
{}'.format(results.cv_results_['mean_test_score'],results.cv_results_['std_test_score'],results.best
_params_,))


import joblib
import pandas as pd
from sklearn.ensemble import RandomForestClassifier
from sklearn.model_selection import GridSearchCV
from sklearn.metrics import classification_report, confusion_matrix
import warnings
warnings.filterwarnings('ignore', category=FutureWarning)
warnings.filterwarnings('ignore', category=DeprecationWarning)

tr_features = x_train
tr_labels = y_train

rf = RandomForestClassifier()
parameters = {
   'n_estimators': [5, 50, 100,150, 200,250,300],#,350,400,450,500,513,550],
    'max_depth': [2, 4, 8, 12, 16, 20]#,24,28,32, None]
 }



cv = GridSearchCV(rf, parameters, cv=5)
cv.fit(tr_features, tr_labels.values.ravel())

print_results(cv)
```

```
#%%

best_model = cv.best_estimator_
best_model.fit(tr_features, tr_labels.values.ravel())

from sklearn.metrics import accuracy_score

y_pred = best_model.predict(x_test)
accuracy = accuracy_score(y_test, y_pred)

print("Test accuracy:", accuracy)

#%%
# save model
joblib.dump(best_model, pathin+'RF_model_v2.3.pkl')
```